ABSTRACT

Title of Dissertation: Development of a laminar-turbulent transition model and blended time-marching schemes for rotorcraft CFD application

Bumseok Lee
Doctor of Philosophy, 2021

Dissertation Directed by: Professor James D. Baeder
Department of Aerospace Engineering

This work focuses on improving rotorcraft Computational Fluid Dynamic (CFD) simulations through the incorporation of an appropriate Galilean invariant transition model suitable for rotating flows and a blended implicit time-marching scheme to reduce unphysical early tip-vortex breakdown.

A correlation-based Galilean invariant transition model is coupled to the Spalart–Allmaras (S–A) turbulence model. The transition model is derived from Menter's 1-eq γ transition model and reformulated to incorporate with the S–A turbulence model. A constant freestream turbulence is applied for local correlations to account for wind tunnel test conditions in CFD simulations. Convergence of the model is improved for implicit time methods by applying the positivity in the implicit operators. The model is extended with two crossflow transition models, one proposed by Langtry et al. and the other one by Menter and Smirnov. The extended model has capability to predict the natural transition, bypass transition, separation-induced transition, and crossflow transition. Calibrations of the transition model are per-

formed based on results of flat plate cases, and a new set of the model constants are proposed. The model is validated against various 2-D airfoils and 3-D cases. Accuracy and robustness of the transition model is demonstrated with comparisons with experimental data. For a 3-D hovering rotor case, the transition model shows similar trends with other CFD, for integrated quantities, but without nonphysical behaviors in transition locations.

The wake breakdown of a hovering rotor in CFD simulations is investigated with a focus on the effect of time marching. Several factors are tested such as 1) time step sizes, 2) temporal accuracy of time-marching schemes (BDF2 and BDF1), and 3) adding temporal damping to the BDF2 scheme. For this purpose, a blended formulation of the BDF2 and BDF1 schemes is derived with a temporal damping variable. Numerical studies are performed for NASA Langleys PSP hovering rotor, and results are compared such as wake structures, integrated rotor performance, and FFT analysis of the thrust coefficient. The results show that adding a small amount of temporal damping to the BDF2 scheme makes the integrated rotor performance settled down and reduces unphysical secondary vortex braid instability in wake structure. It is shown that the blended BDF scheme with a temporal damping can be used as an engineering solution of the wake structure breakdown in CFD rotor simulations without significant loss of temporal accuracy.

Development of a laminar-turbulent transition model and blended time-marching schemes for rotorcraft CFD application

by

Bumseok Lee

Dissertation submitted to the Faculty of the Graduate School of the
University of Maryland, College Park in partial fulfillment
of the requirements for the degree of
Doctor of Philosophy
2021

Advisory Committee:
Dr. James D. Baeder, Chair/Advisor
Dr. Inderjit Chopra
Dr. Anubhav Datta
Dr. Jacob Bedrossian
Dr. Johan Larsson, Dean's Representative

Table of Contents

List of Tables

List of Figures

List of Abbreviations

C_d	Drag coefficient
C_f	Skin friction coefficient
C_l	Lift coefficient
C_t	Thrust coefficient
C_p	Pressure coefficient
C_q	Torque coefficient
FM	Figure of Merit defined as $\frac{C_t^{3/2}/\sqrt{2}}{C_q}$
Tu	Freestream turbulence intensity defined as $Tu = 100\sqrt{\frac{(u'^2+v'^2+w'^2)/3}{U}}$
Re	Reynolds number
Re_v	Vorticity Reynolds number
$Re_{\theta t}$	Momentum thickness Reynolds number
α	Angle of attack
β	Angle of side slip
γ	intermittency

Chapter 1: Introduction

1.1 Motivation

1.1.1 Galilean invariant transition model

Prediction of laminar-turbulent transition is important in the design of a new wing, fuselage, rotor blade, or wind turbine blade. Laminar-turbulent transition affects viscous drag, flow separation, and heat transfer, and ignoring the effect of transition often results in inaccurate predictions of the drag and flow development. For fixed wing aircraft, maintaining laminar flow on wings or a fuselage is considered one of the key requirements for next generation aircraft. Laminar flow on wings and fuselage reduces total vehicle drag, and thus decrease fuel burning and gas emission. For rotorcraft, laminar-turbulent transition affects fuselage drag and rotor performance. In a recent experimental study by Overmeyer and Martin [10], it was observed that the rotor with the natural transition has 7.1 and 4.9 counts higher Figure of Merits (a hovering efficiency) at low and high thrusts, respectively, than the rotor with the fixed transition on the both upper and lower surfaces of the blade. One count of the Figure of Merit difference is approximately equivalent to 170 lbs of payload for an UH-60 class helicopter at standard sea-level conditions [11].

7.1 and 4.9 count differences are approximately 1207 lbs and 833 lbs, respectively, and these are non-negligible amounts in a helicopter design. In NASA's CFD Vision 2030 Study: A Path to Revolutionary Computational Aerosciences [12], the capability for prediction of turbulent flow with laminar turbulent transition and flow separation is considered "the single, most critical area" among five pacing items in CFD simulations by 2030. The importance of the accurate prediction of the laminar turbulent transition cannot be overstated.

To predict laminar-turbulent transition in general purpose CFD simulations, an additional transition model is required. Direct Numerical Simulation (DNS) or Large Eddy Simulation (LES) can predict laminar turbulent transition directly without any modeling, but they are prohibitively expensive for engineering applications. In the Reynolds Averaged Naiver–Stoke (RNAS) simulations, turbulence models, such as the S–A [13] or $k-\omega$ SST [14] model, were developed based on the assumption of fully turbulent flow, so they require additional corrections to predict laminar-turbulent transition. Several transition models have been developed for this purpose based on the stability theory methods (e^N methods) or partial-differential equation (PDE) methods. Among them, one of the most successful models is Langtry–Menters γ-$Re_{\theta t}$ model [15]. The model is suitable for modern CFD methodologies such as parallelization (due to only needing local quantities) and is compatible with both structured and unstructured meshes. For this reason, the model has become the most widely used transition model in industrial CFD simulations since its publication in 2009.

However, one of the limitations of Langtry–Menters model is a lack of Galilean

invariance. Galilean invariance implies an independence on the frame of reference and is a well known requirement of turbulence modeling [16]. However, Langtry–Menter's model is not Galilean invariant because the model uses 1) flow quantities along the streamwise direction and 2) the local velocity vector for the local correlations. The lack of Galilean invariance does not matter for a stationary object but can cause issues for general multiple moving objects such as for a helicopter rotor system. Several numerical studies already have shown irregular behaviors of the transition model for rotor simulations, such as nonphysical trends of transition locations or unphysically high turbulent intensity [5,17–20]. Therefore, to avoid these issues, a transition model with Galilean invariance is required for general applications. The first objective of the present work is to develop an appropriate Galilean invariant transition model for the S–A turbulence model.

1.1.2 Wake breakdown of a hovering rotor

In rotorcraft CFD simulations, wake structure breakdown is a phenomenon where the vortical structures of a rotor are destroyed by the secondary vortex braid instability (also called vortical worms, vortex soup). Figure 1.1 shows wake breakdown from a 3-bladed TRAM rotor simulation by Chaderjian [21]. The instability appears in both hover and forward flight simulations, but its effect on the wake structure is more dominant in hover cases because in forward flight, the non-zero freestream velocity convects the wake downstream away from the rotor system and helps stabilize the wake. Figure 1.2 shows a development of the wake breakdown

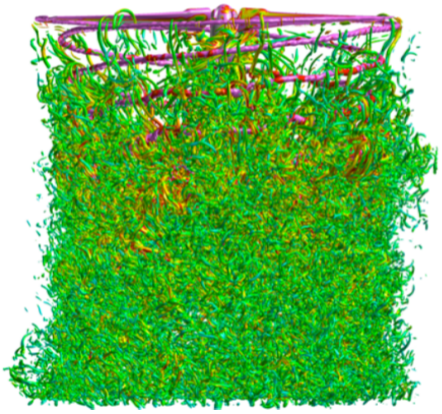

Figure 1.1: Wake breakdown of a TRAM rotor by the secondary vortex braid instability.

for a hovering S-76 rotor. The mechanism responsible for wake breakdown in CFD simulations has not been fully understood yet, but, in general, its process is as follows:

1. Secondary vortex braid instability appears in the middle or far wake region after rotor revolution 5∼8.
2. The secondary vortex braids propagate to the entire flowfield.
3. Helical vortex structures are destabilized by the secondary vortex instability.
4. The tip vortices are destroyed in the middle or far wake.

The wake breakdown has been observed since a high-order numerical scheme and/or adaptive mesh refinement (AMR) were applied in rotor CFD simulations. It was not observed in hover simulations in 1990s, but it is frequently observed in recent hover simulations such as UH-60 rotor simulations by Hariharan et al. [22], TRAM rotor by Chaderjian [21], S-76 rotor by Jain [23].

In order to identify factors causing wake breakdown, several numerical studies have been performed. Abras et al. [24–26] tested different conditions such as 1) the

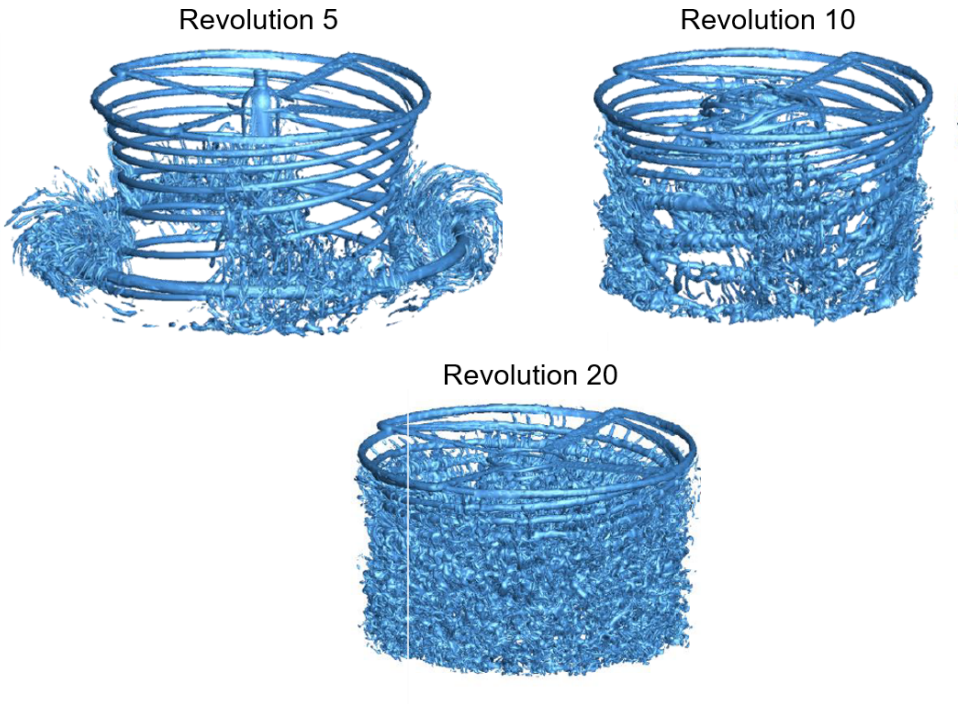

Figure 1.2: Development of wake breakdown of S-76 rotor. Image reproduced from Abras et al. (2019)

number of blades, 2) the turbulence model, and 3) type of off-body grid for an S-76 hovering rotor; and showed less wake breakdown with a large torus mesh rotating together with the blade. The current author also looked at the effect of temporal accuracy on wake breakdown for an S-76 hovering rotor [17]. In the work, a reduced temporal accuracy from 2nd order to 1st order suppress generation of secondary vortices and better preserve tip vortices with minimum effects on integrated rotor performances and blade loadings. However, it is known that eventually rotor wakes will breakdown, just not in the vicinity of the rotor. Since critical factors causing the wake breakdown are still not clear, there are no engineering solutions of the wake breakdown yet. The second goal of the present study is further investigation of the wake breakdown with a focus on time-marching schemes in CFD simulations and to propose an engineering solution for more physical wake structures.

1.2 Background

This chapter reviews 1) basic ideas of laminar-turbulent transition, 2) Galilean invariance, and 3) transition prediction methods. The first part of the chapter discusses four modes of laminar-turbulent transition that will be mentioned through the present dissertation. Then, Galilean invariance is described with various flow quantities. Finally, PDE-based transition models are discussed.

1.2.1 Physics of laminar-turbulent transition

Laminar-turbulent transition (or transition) is the process by which the laminar flow becomes turbulent. In 1883, Osborne Reynolds first reported the phenomena using a critical non-dimensional parameter, Reynolds number, from pipe flow experiments [27]. The transition process begins with perturbations in the boundary layers by disturbances such as freestream acoustic waves, surface roughness, and interaction with turbulent flows, which are referred as the receptivity. Based on the disturbances, the transition undergoes different paths and can be described as different modes. This section reviews four types of transition; natural transition, bypass transition, crossflow transition, and separation-induced transition.

1.2.1.1 Natural transition

Natural transition is one of the most common types in aerodynamic flows. It occurs for conditions with low freestream turbulence level. The turbulence level can be represented with the turbulence intensity (Tu), which is a ratio of the root mean

square of the turbulent fluctuation velocity to the mean velocity. Natural transition occurs when the turbulence intensity is less than 1%. The transition is triggered by infinitesimal disturbances, and two dimensional Tollmien-Schlichting waves start to grow. Figure 1.3 shows the development of natural transition. Flow changes from two dimensional Tollmien-Schlichting waves to three dimensional vortex breakdown to turbulent spots to fully turbulent flow. The natural transition is well predicted by linear stability theory.

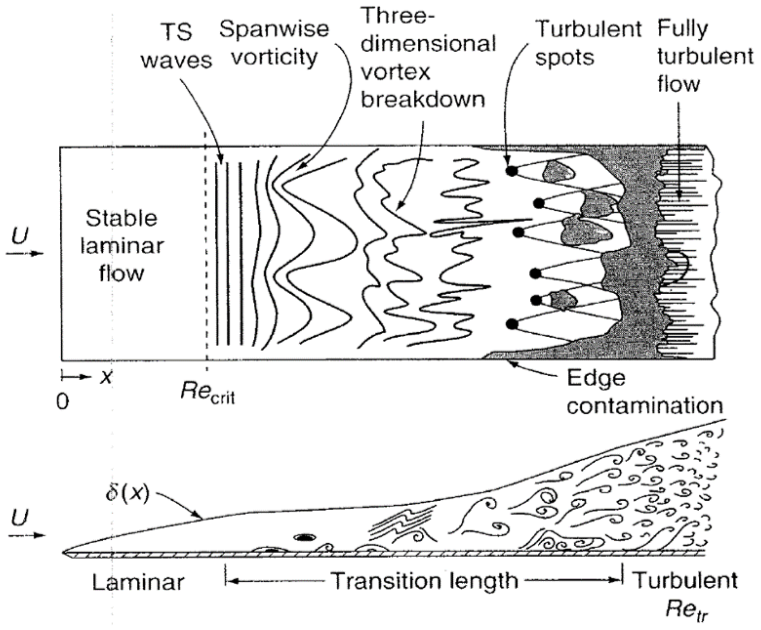

Figure 1.3: Schematic of natural transition process. Image reproduced from White (2006) [1].

1.2.1.2 Bypass transition

For high freestream turbulence intensity ($Tu > 1.0\%$) or rough surfaces, the first or second/third stages of the natural transition are bypassed, and the vortex breakdown or turbulent spots are directly formed. This type of transition is known as

bypass transition. The bypass transition is often observed in turbomachinery flows due to high disturbances in the downwash of blades or large surface roughness. It is generally believed that Tollmien-Schlichting waves are not observed in the bypass transition if the turbulent intensity is larger than 1% [28].

1.2.1.3 Crossflow transition

On a swept wing, the laminar boundary layer has three-dimensional velocity profiles: tangential and crossflow velocity profiles. Figure 1.4 shows velocity profiles of the three-dimenional boundary layer on a swept wing. The instability in the tangential direction is similar to two-dimensional Tollmien-Schlichting waves. On the other hand, when a sweep angle is large, instability in the crossflow becomes dominant and can also cause transition. The phenomenon is referred to as crossflow

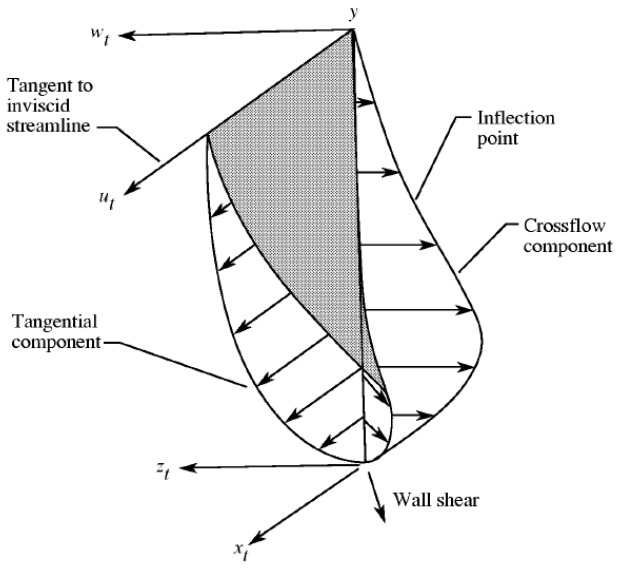

Figure 1.4: Boundary layer velocity profiles on a three-dimensional sweep. Image reproduced from Dagenhart and Saric (1999) [2]

transition. The crossflow transition occurs earlier than the transition by Tollmien-

Schlichting waves (natural transition), if it occurs.

1.2.1.4 Separation-induced transition

When a laminar boundary layer separates under strong adverse pressure gradient, it forms a separation bubble and reattaches due to increased mixing in the downstream turbulent shear layers. This process is called the separation-induced transition. The separation-induced transition is often observed near the leading edge of an airfoil on the upper surface. Figure 1.5 shows the separation-induced

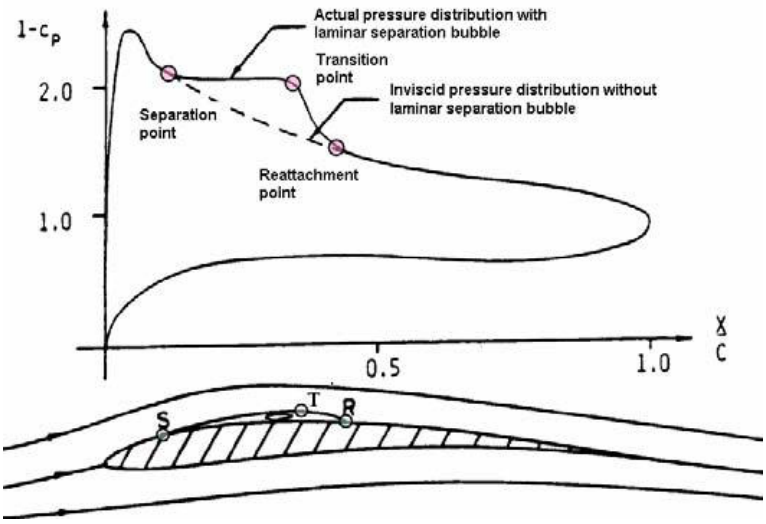

Figure 1.5: Pressure distribution across the separation bubble. Image reproduced from Russell (1979) [3].

transition on an airfoil and corresponding surface pressure distribution. The pressure distribution remains flat (constant) at the forward portion of the bubble and then rapidly drops after the transition. The length of the bubble is a function of Reynolds number and/or angle of attack. Sudden changes of bubble length from "short" to "long" is called "bursting" and can result in significant loss of lift or increase in drag.

1.2.2 Galilean invariance in CFD simulations

A flow quantity that remains the same under Galilean transformation is referred to as Galilean invariant. Galilean transformation is a transformation between two inertial frames of reference with a constant relative velocity. Figure 1.6 shows a schematic of two coordinate systems with a constant relative velocity, v. Under the

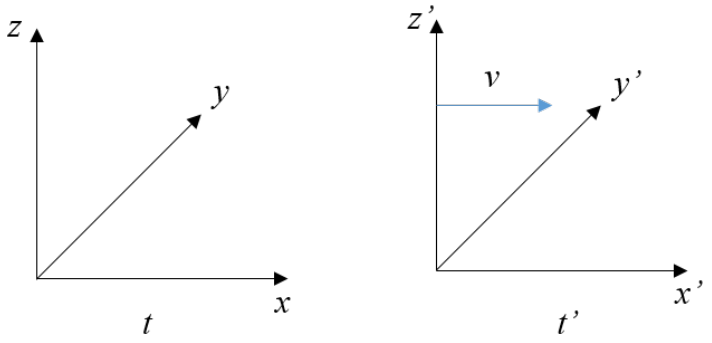

Figure 1.6: Schematic of two coordinate systems for Galilean transformation.

Galilean transformation, relations between two coordinate systems, (x, y, z, t) and (x', y', z', t'), can be written as

$$\begin{aligned} x' &= x - vt \\ y' &= y \\ z' &= z \\ t' &= t \end{aligned} \tag{1.1}$$

where v is a relative velocity (constant). From the above relations, it can be shown that the flow velocity vector is not Galilean invariant because the relative velocity

is subtracted (or added) from the original velocity as

$$u' = u - v \tag{1.2}$$

where u and u' are the velocity components in the x and x' directions, respectively, and v is a constant. Similarly, streamlines, which are parallel to the velocity vector, are not Galilean invariant for the same reason. On the other hand, scalar quantities such as density and pressure are Galilean invariant. Also, the velocity gradient is Galilean invariant, and it can be shown that

$$\frac{\partial u'}{\partial x'} = \frac{\partial}{\partial x'}(u - v) = \frac{\partial}{\partial x'}u = \frac{\partial u}{\partial x}\frac{\partial x}{\partial x'} + \frac{\partial u}{\partial t}\frac{\partial t}{\partial x'} = \frac{\partial u}{\partial x} \tag{1.3}$$

Therefore, quantities related to the velocity gradients such as the rate of strain (S_{ij}), the magnitude of vorticity (Ω_{ij}), vorticity vector (ω_{ij}) are also Galilean invariant. Although the helicity ($u \cdot \omega$) includes the vorticity vector, it is not Galilean invariant due to the velocity vector. A partial derivative of the velocity vector ($\frac{\partial u}{\partial t}$) is not Galilean invariant, whereas the total derivative of the velocity vector ($\frac{Du}{Dt}$) is Galilean invariant. Finally, the Navier-Stokes equations are Galilean invariant [16]. Table 1.2.2 lists Galilean invariant/non-Galilean invariant flow quantities and variables.

Galilean invariance is one of the necessary requirements in turbulence modeling. Because the Navier-Stokes equations are Galilean invariant, the model equations should follow the property of the governing equations. In other words, the

Galilean invariant	non-Galilean invariant
density, pressure, velocity gradient, vorticity, strain, Du/Dt	velocity, streamline, helicity, $\partial u/\partial t$

Table 1.1: Galilean invariant and non-Galilean invariant quantities in the fluid dynamics.

model equations should give the same solutions regardless of the frame of reference in the inertial system. Turbulence models, such as the S–A [29] or $k-\omega$ SST [30] model, were developed such that they satisfy Galilean invariance.

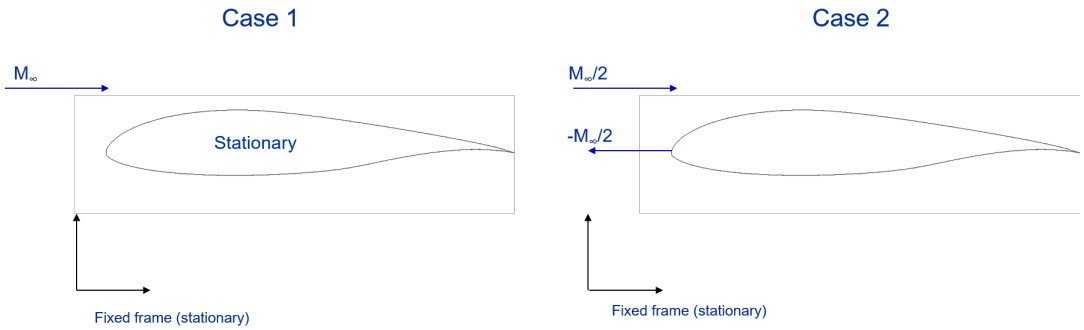

Figure 1.7: Two inertial systems with and without the grid motion.

Figure 1.7 shows a notional case in two different inertial systems to show Galilean invariance in CFD simulations. Case 1 has a stationary airfoil with freestream Mach number of 0.2. On the other hand, Case 2 has freestream Mach number of 0.1, but the airfoil is moving with Mach number of 0.1. CFD simulations for the two cases should give the same solutions because the relative velocity to the airfoil wall is the same. Figure 1.8 compares predicted lift and drag coefficients for the two cases from fully turbulent CFD simulations using the S-A turbulence model. The figure shows that Case 1 and Case 2 have the same time histories of lift and drag

coefficients, respectively.

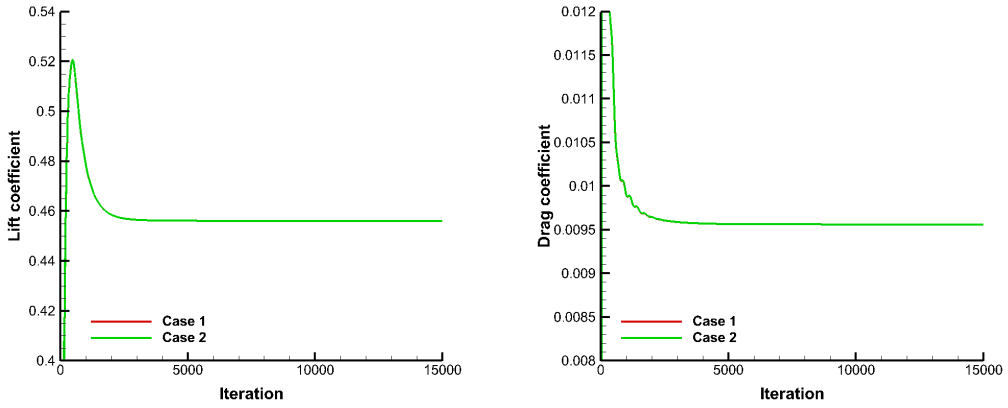

(a) Lift coefficient.

(b) Drag coefficient.

Figure 1.8: Comparison of lift and drag coefficients for the two cases: fully turbulent simulations.

Figure 1.9 compares solutions of Case 1 and Case 2: ρ, ρu, and $\tilde{\nu}$ (the solution from the S-A turbulence model). Because density is Galilean invariant, the two contours from Case 1 and 2 are exactly the same. On the other hand, ρu is not Galilean invariant, so the results from the two cases show different contours. Note that the Navier-Stoke equations are Galilean invariant, but their solutions can be non-Galilean invariant. For $\tilde{\nu}$, the solution of the S-A turbulence model, the results from the two cases have the same contours because the turbulence model is Galilean invariant. In other words, the S-A turbulence model does not use any non-Galilean invariant variables, so it gives the same solutions for the two cases whether the airfoil is moving or not.

The same cases are simulated using two transition models: 1) Medida-Baeder 2-eq transition model (non-Galilean invariant) and 2) a new 1-eq Galilean invariant transition model from the current study. Details of the each transition model is

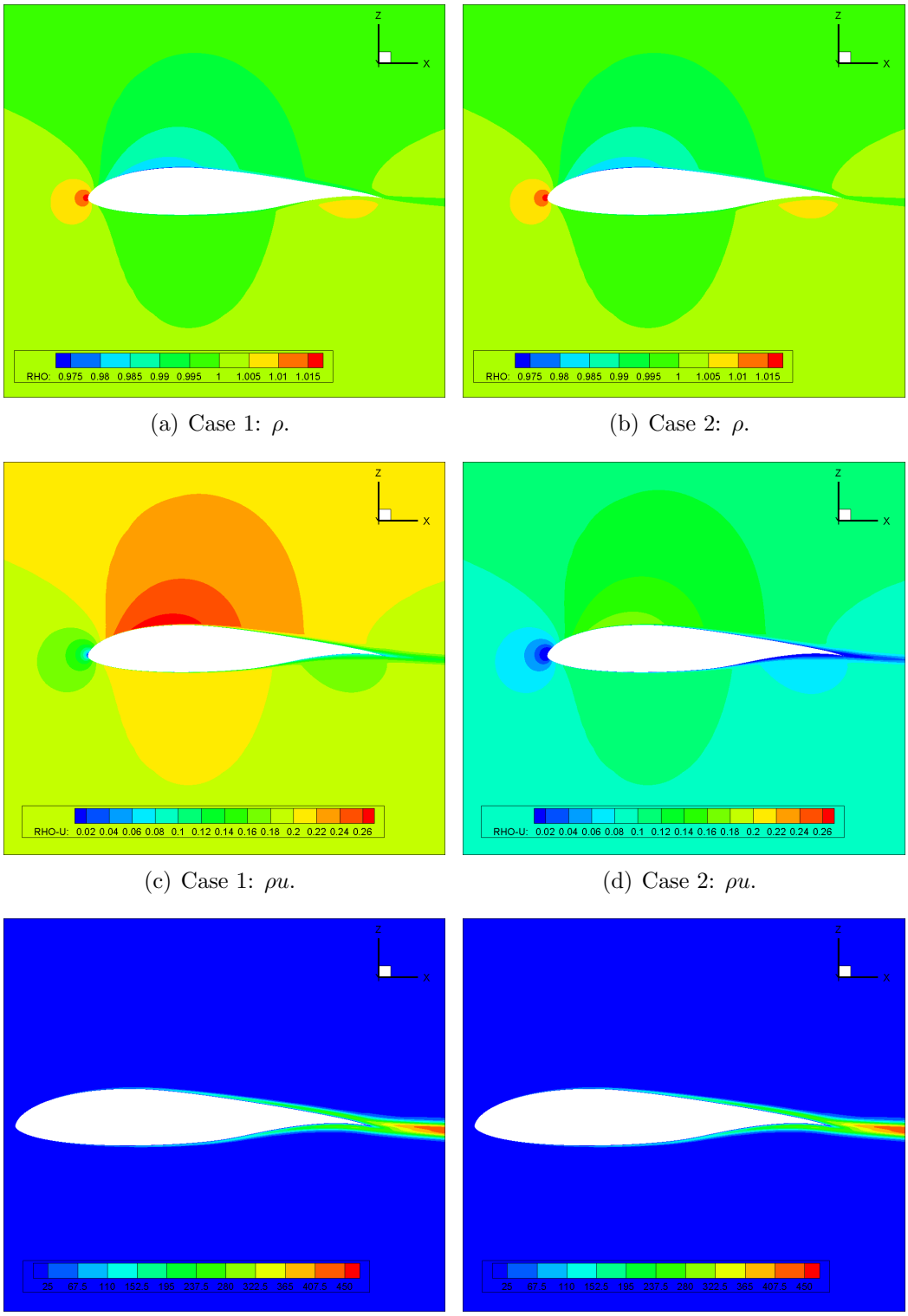

(a) Case 1: ρ.

(b) Case 2: ρ.

(c) Case 1: ρu.

(d) Case 2: ρu.

(e) Case 1: $\tilde{\nu}$.

(f) Case 2: $\tilde{\nu}$.

Figure 1.9: Comparison of contours between the case 1 and case 2: fully turbulent simulations using the S-A turbulence model.

given in a later section of this dissertation. Figure 1.10 compares time histories of lift and drag coefficients resulting from the two transition models. It is seen that the non-Galilean invariant 2-eq transition model results in different time histories of lift and drag coefficients for Case 1 and 2, whereas the new Galilean invariant 1-eq transition model gives the same lift and drag coefficients for the two cases.

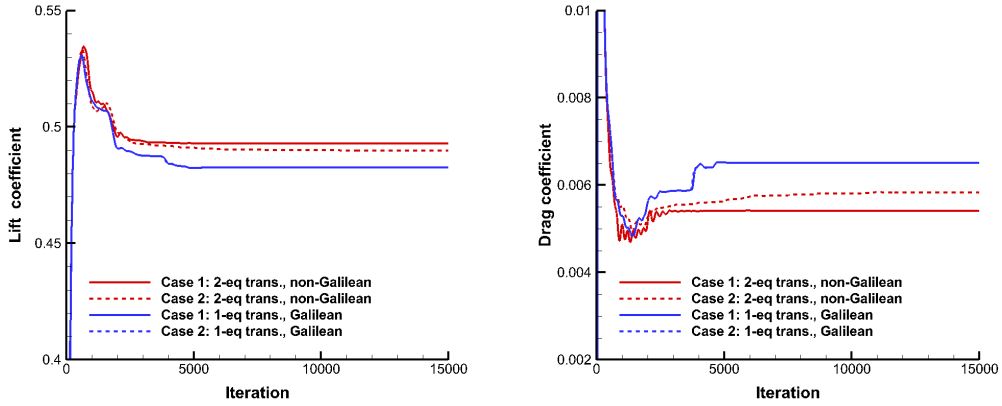

(a) Lift coefficient. (b) Drag coefficient.

Figure 1.10: Comparison of lift and drag coefficients for the two cases: transition simulations.

Figure 1.11 compares solutions from the 2-eq transition model, intermittency (γ) and the transition momentum thickness Reynolds number ($Re_{\theta t}$). For the intermittency contours, a ratio of x-axis to y-axis is adjusted to see differences on the surface more clearly. Because the transition model is not Galilean invariant, results from the two cases show different contours of γ and $Re_{\theta t}$. Transition locations of Case 1 and Case 2 are also different on both the upper and lower surfaces of the airfoil, resulting in the different lift and drag coefficients in Fig. 1.10. On the other hand, Figure 1.12 shows intermittency contours from the 1-eq transition model. Because the model is Galilean invariant, results from Cases 1 and 2 give the same intermittency contours like $\tilde{\nu}$ shown in Figure 1.9.

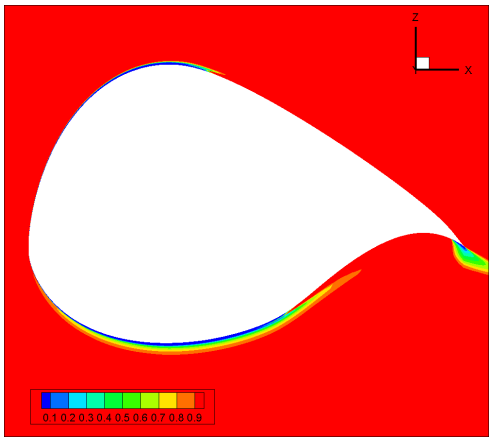

(a) Case 1: γ.

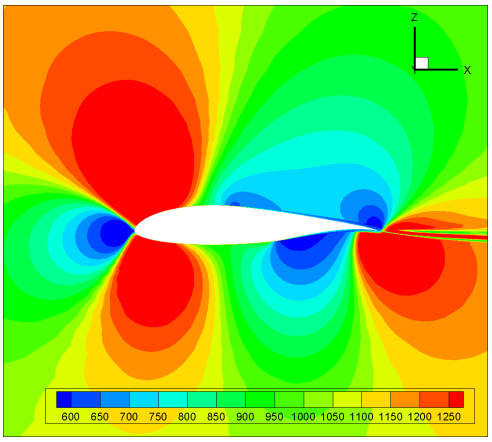

(b) Case 1: $Re_{\theta t}$.

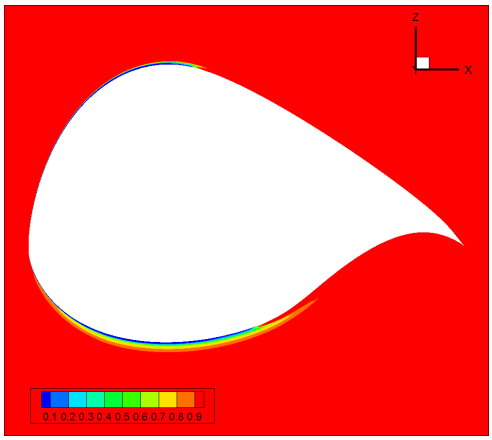

(c) Case 2: γ.

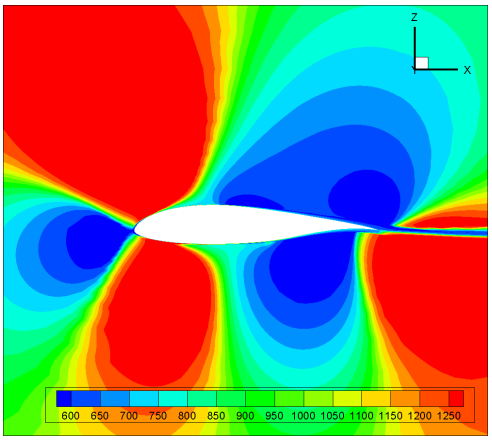

(d) Case 2: $Re_{\theta t}$.

Figure 1.11: Comparison of solutions from the 2-eq transition model.

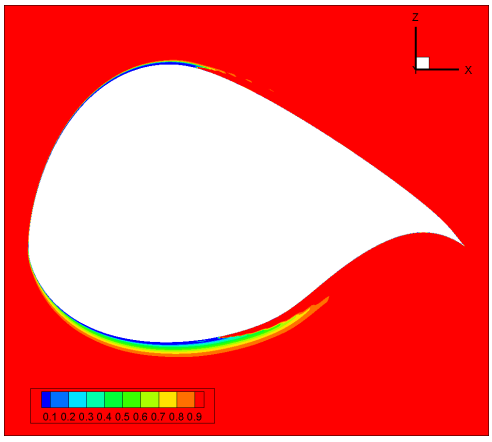

(a) Case 1: γ.

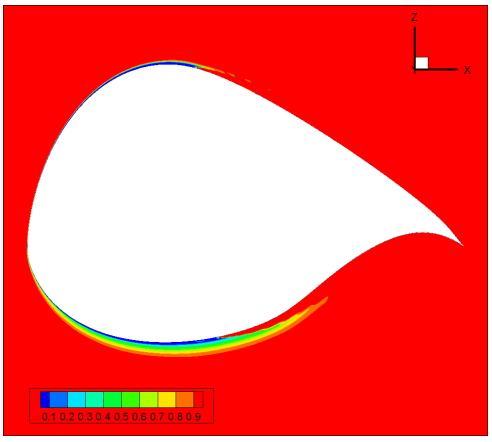

(b) Case 2: γ.

Figure 1.12: Comparison of solutions from the 1-eq transition model.

As mentioned earlier, the 2-eq transition model is not Galilean invariant, and it depends on the frame of reference. However, for an inertial motion, the velocity vector can be corrected such that the local velocity is relative to the moving wall. This is simple work because the relative velocity between two inertial systems is just a constant. If the corrections of the velocity vector are made for Case 2, then the transition model gives the same solutions for Case 1 and 2, shown in Figures 1.13 and 1.14.

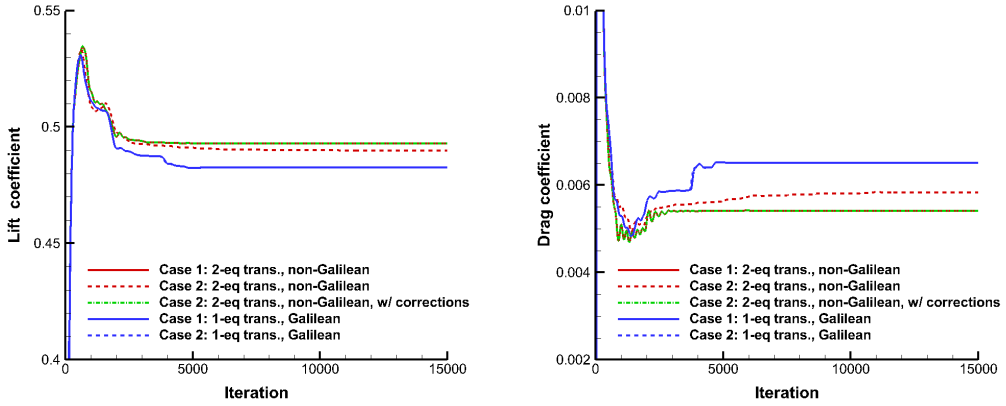

(a) Lift coefficient. (b) Drag coefficient.

Figure 1.13: Comparison of lift and drag coefficients for the two cases: transition simulations.

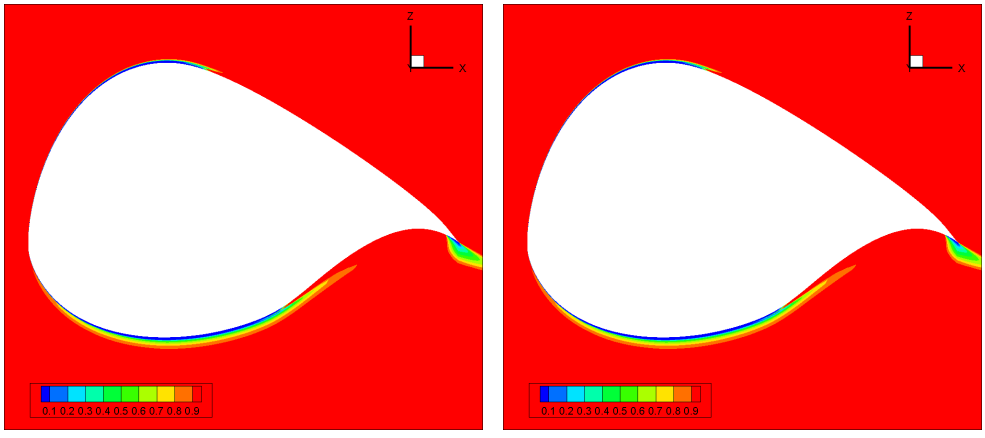

(a) Case 1: γ. (b) Case 2 with correction: γ.

Figure 1.14: Comparison of solutions from the 2-eq transition model for the case 1 and case 2.

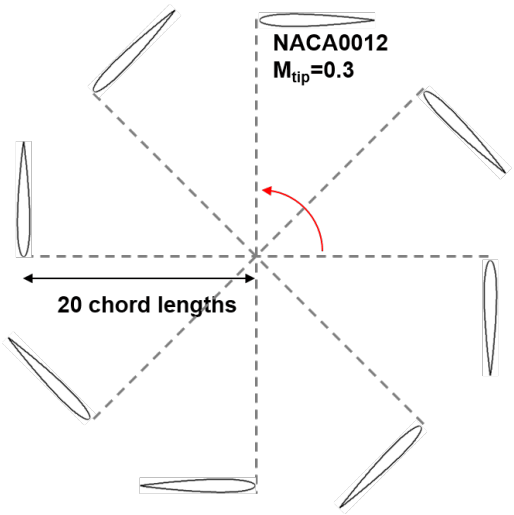

Figure 1.15: 2-D rotating NACA0012 airfoil.

A problem with non-Galilean invariant models is a non-inertial motion. As a second notional case, a 2-D rotating NACA0012 airfoil is shown in Figure 1.15. The NACA0012 airfoil is located at 20 chord lengths from the center of rotation, and the tip Mach number is 0.3. The effective pitch angle of the airfoil is zero and does not change. Although the airfoil is symmetric, it has an effective camber because rotational velocities are different at different locations on the airfoil. Figure 1.16 compares the normal and axial forces of the rotating airfoil resulting from the two transition models. As it was discussed in the previous cases, the correction should be made for the non-Galilean invariant 2-eq transition model to account for the motion of the airfoil. However, the corrections for non-inertial motion are not simple anymore unlike the correction for an inertial motion with a constant relative velocity. In Figure 1.16, the corrections are made such that the local velocity vector is with respect to the moving wall. However, other CFD work [18–20,31] show such velocity corrections give some nonphysical behaviors of the transition model for 3-D hovering rotor such as requiring a much higher input freestream turbulence intensity. Consid-

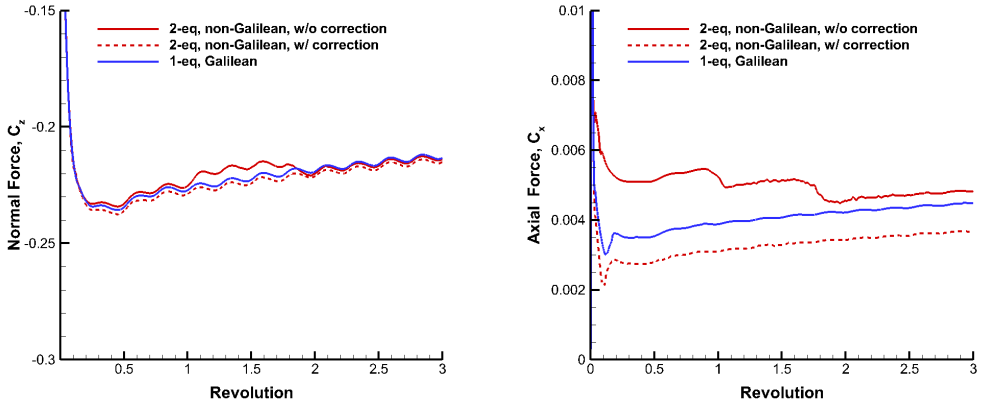

(a) Lift coefficient.

(b) Drag coefficient.

Figure 1.16: Comparison of the normal and axial forces of rotating NACA0012 airfoil: transition simulations.

ering the momentum equations of the Navier-Stokes equations from inertial frame to the rotational frame with the addition of Coriolis and centrifugal force terms, not just changes to the velocity for the flux terms, there may be some missing terms in the corrections. However, it is not clear how the corrections should be made for non-inertial motions such as due to rotating or pitching. This explains why non-Galilean invariant models should be avoided for simulations of moving objects. In summary, non-Galilean invariant turbulent and/or transition model is not desirable because 1) it depends on the frame of reference, and 2) the correction should be made for moving objects, but 3) the corrections for general non-inertial motions are not clear. On the other hand, a Galilean invariant model does not depend on the frame of reference and thus does not require such corrections. Finally, a Galilean invariant model follows the characteristics of the governing equations.

1.2.3 Transition prediction method

This section discusses prediction methods of the transition. Transition can be predicted using 1) e^n method based on linear stability theory, 2) local correlation methods, 3) PDE-based methods, or 4) Direct Numerical Simulations (DNS) / Large Eddy Simulations (LES). Among them, this section mainly focuses on PDE-based methods. The other two prediction methods, 1) e^n method based on linear stability theory and 2) local correlation methods, are discussed in Appendix A. DNS or LES also gives precious insights to understand physics of the transition, but they are too costly to use in general engineering applications. For this reason, DNS or LES is not reviewed in this dissertation.

The PDE-based methods consist of one or two partial differential transport equations. They should be solved using a numerical algorithm, and an output from the model is coupled to a baseline turbulence model to control the turbulent eddy viscosity generation. Table 1.2.3 shows the most widely used PDE-based transition models, which will be mentioned in this dissertation repeatedly. Each model is discussed in the following chapters.

Transition model	Turbulence model	Galilean invariant	Year
Langtry-Menter [15] 2-eq $\gamma - Re_{\theta t}$	k-ω-SST	No	2009
Medida-Baeder [32] 2-eq $\gamma - Re_{\theta t}$	SA	No	2014
Menter et al. [33] 1-eq γ	k-ω-SST	Yes	2015
Coder [34, 35] 2-eq AFT	SA	Yes	2019

Table 1.2: List of the PDE-based transition models.

1.2.3.1 Langtry-Menter's 2-eq $\gamma - Re_{\theta t}$ model

Langtry-Menter's 2-eq $\gamma - Re_{\theta t}$ model [15] is one of the most successful model in RANS-based transition modelling. The model is based on local correlations and doesn't require non-local operations. The model consists of two transport equations, one for intermittency (γ) and one for transition onset momentum-thickness Reynolds number ($Re_{\theta t}$). The output intermittency turns on/off the source terms of the turbulent kinetic energy of the SST turbulence model [14], and the transition onset momentum-thickness Reynolds number couples the empirical correlation to the transition onset criteria.

A key idea of the model is using the vorticity Reynolds number (Re_v) like Van Driest and Blumer Correlation [36] instead of the momentum thickness Reynolds number ($Re_{\theta t}$) to avoid non-local operations based on the following relations:

$$Re_{\theta t} = \frac{\max(Re_v)}{2.193} \tag{1.4}$$

Transition onset occurs when the scaled vorticity Reynolds number exceeds the critical value of the momentum thickness Reynolds number ($Re_{\theta c}$) as

$$F_{onset} = \frac{Re_{\theta t}}{Re_{\theta c}} \approx \frac{Re_v}{2.193 Re_{\theta c}} \tag{1.5}$$

The model has a capability to predict natural transition, bypass transition, and separation-induced transition, and it has been extended with crossflow transition

models proposed by Langtry et al. [37], Muller and Herbst [38], and Grabe et al. [39]. Similarly, the model has been coupled with roughness-induced transition models suggested by Dassler et al. [40] and Langel et al. [41]. The transition model was originally developed for $k-\omega$ SST turbulence model; but Medida and Baeder [32] coupled it to the S-A turbulence model with modifications, which will be discussed in the following section.

One of the limitations of the model is a lack of Galilean invariance. The model is not Galilean invariant because the transport equation for the transition onset momentum-thickness Reynolds number requires flow quantities along the streamwise direction as well as the local velocity vector.

1.2.3.2 Medida-Baeder 2-eq $\gamma - Re_{\theta t}$ model

Medida–Baeder model [32] was derived from Langtry–Menter's model [15]. The model is incorporated with the S–A turbulence model and was reformulated to remove the dependence on the k and ω of the SST turbulence model. There are four primary differences between Langtry–Menter's model and Medida–Baeder model. Firstly, Medida–Baeder model employs modified transport equation for intermittency with a new transition onset function (G_{onset}) to improve recovery of intermittency in the turbulent boundary layers. Because the function requires operations along the boundary layer, however, the model is not fully local. Secondly, in Medida–Baeder model, a constant freestream turbulence intensity is used in the computational domain because the local turbulence intensity is not available with

the S–A turbulence model. Thirdly, the separation-induced transition modification of Langtry–Menter's model is omitted. Finally, for Medida-Baeder model, the output intermittency is applied to the production term of the S–A turbulence model. Because Medida-Baeder model employs the same transport equation for the momentum thickness Reynolds number ($Re_{\theta t}$), it is not Galilean invariant either.

1.2.3.3 Menter's 1-eq γ model

The motivation of Menter's 1-eq γ transition model [33] is to improve limitations of Langtry–Menter's $\gamma - Re_{\theta t}$ model: 1) the lack of Galilean invariance, and 2) complexity in the $Re_{\theta t}$ transport equation. The new transition model has only one transport equation for intermittency, and the second transport equation in Langtry-Menter's model is simplified with algebraic relations. The model also uses the relation between the vorticity Reynolds number and the critical momentum thickness Reynolds number for the transition onset criteria as

$$F_{onset1} = \frac{Re_v}{2.2Re_{\theta c}} \tag{1.6}$$

like Langtry-Menter's model. The intermittency transport equation is newly formulated based on the new local correlations.

The model achives Galilean invariance by replacing quantities along the streamwise direction with the wall normal direction as

$$\frac{dU}{dx} = -\frac{dV}{dy} \tag{1.7}$$

where U and x are the streamwise velocity and coordinate, respectively, and similarly, V and y are the wall-normal velocity and coordinate, respectively. In addition, the magnitude of the local velocity (U) for the turbulence intensity is replaced with the specific rate of dissipation (ω) and the wall distance (d_w) as

$$U \approx \omega d_w \tag{1.8}$$

Nichols [42] first made efforts to integrate Menter's 1-eq γ transition model with the S–A turbulence model and showed promising results. However, in the work, the initial condition of the SA turbulence model ($\tilde{\nu}$) is used as an input of the transition model instead of the freestream turbulence intensity from experiments. Therefore, it cannot account for the experimental flow condition (physical value), but the numerical value of the turbulence model should be adjusted to match the experimental data.

1.2.3.4 Coder's Amplification Factor Transport (AFT) 2-eq transition model

Coder's Amplification Factor Transport (AFT) model [34, 35] is based on the linear stability theory. A key idea of the model is using the simplified linear stability theory by employing the approximate envelope method proposed by Drela and Giles [43] instead of full application of linear stability theory or computational expensive database look-up. The original version of the model [34] solves one transport equation for the envelope amplification factor ($\tilde{n}$), but the latest version [35]

consists of two transport equations, one for the envelope amplification factor ($\tilde{n}$) and one for modified intermittency. The envelope amplification factor is calculated from the boundary layer shape factor with the pressure gradient and then used for the transition onset criteria. The modified intermittency is coupled to the f_{t2} term of the SA turbulence model and triggers the transition onset. The original version of the model was not Galilean invariant, but the latest version is Galilean invariant by applying Menter's approach shown in Eq. 1.7 for calculations of the pressure gradient parameter. Similarly, the modified intermittency equation is also derived from Menter's 1-eq transition model [33]. For example, in the AFT model, transition onset criteria shown in Eq. 1.6 is replaced with stability theory as

$$F_{onset1} = \frac{\tilde{n}}{N_{crit}} \tag{1.9}$$

where $\tilde{n}$ is the envelope amplification factor and N_{crit} is the critical amplification factor from Mack [44].

1.3 Literature Review

This section reviews research work about two main topics of the present dissertation: 1) application of a transition model for helicopter rotor simulations and 2) rotor wake structure breakdown. In the first section, transition predictions of a hovering rotor using a transition model are reviewed. Several issues and limitations of the work are also identified. In the second section, numerical and experimental investigations of rotor wake breakdown are presented. Because there is very lim-

ited experimental work, the section mainly focuses on numerical studies from CFD simulations.

1.3.1 Prediction of transition on a hovering rotor

This section reviews papers presented as part of the AIAA Hover Prediction Workshop since 2015 with regard to transition modelling of a rotor blade. Numerical simulations of a rotor have been performed using either stability based models or PDE based transition models by several research groups. Before the experimental study of PSP rotor by Overmeyer and Martin [10] was published in 2017, however, most work included limited transition prediction validation from a lack of available experimental data.

Jain [23] investigated the effect from including a transition model for S-76 rotor using CREATE-AV Helios (NASA's OVERFLOW as a near-body flow solver) [45] with Langtry–Menter's transition model [15]. However, in the work, the transition model over-predicts Figure of Merit and gives less accurate prediction than the fully turbulent simulations. Lee et al. [4] compared fully turbulent and transition simulations of S-76 rotor using OVERTURNS flow solver with the Medida-Baeder transition model [32]. In the results, Figure of Merit was only reasonably predicted with very high freestream turbulence intensity around 2.0%. In addition, the lower surface of the blade shows suspicious earlier transitions near the swept tip of the blade regardless of thrust levels, which is shown in Figure 1.17. Garcia et al. [46] performed hover simulations of XV-15 proprotor using HMB flow solver with Menter's

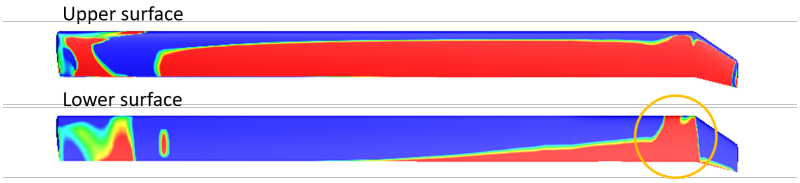

Figure 1.17: Intermittency contour on the S-76 rotor blade: Red-turbulent, Blue-laminar flow. Image reproduced from Lee et al. (2017) [4].

γ transition model [47]. In the work, the transition model improves comparisons of the skin friction coefficient with the experiment but doesn't affect the integrated rotor performance. Similarly, Sheng [48] made comparisons of the integrated of rotor performances of XV-15 proprotor between transition simulations using UN^{2}CLE flow solver and fully turbulent simulations using CREATE-AV Helios [45]. However, in the integrated rotor performance, no meaningful differences are observed between the fully turbulent and transition results. It is considered that laminar flows on S-76 rotor or XV-15 rotor are very limited, so these cases are not proper to validate the transition modeling.

Recently, the limitations are relieved by the experimental study for NASA Langley's PSP rotor by Overmeyer and Martin [10]. In the experiment, hover performances were investigated as a function of various transition conditions, and transition locations were measured on the blade surfaces using the infrared thermography techniques. With the release of the experimental data, numerical simulations of PSP hovering rotor have been conducted using various transition models as shown in Table 1.3.1.

Jain [5] performed transition simulations using CREATE-AV Helios (NASA's OVERFLOW as a near-body flow solver) with Langtry–Menter's transition model.

Authors	Flow Solver	Turublence model	Transition model	Tu
Jain [5]	Helios (OVERFLOW)	SST	Langtry-Menter 2-eq	0.08%
Vieira et al. [49]	STAR-CCM$^+$	SA-RC	Coder's AFT 1-eq	0.07% (N_{crit}=9)
Coder et al. [35, 50]	OVERFLOW	SA-neg-RC	Coder's AFT 2-eq	0.07% (N_{crit}=9)
Zhao et al. [51, 52]	UN^{2}CLE	SST SA	Langtry-Menter 2-eq	Unkown
Lee et al. [18]	OVERTURNS	SA-R	Medida-Baeder 2-eq	0.75%
Fitzgibbon et al. [53]	HMB	SST	Menter's 1-eq	Unknown
Kwon et al. [19, 20]	In-house Unstructured	SST	Langtry-Menter 2-eq	1.0%

Table 1.3: Transition simulations of NASA Langley's PSP hovering rotor.

The work compared predicted rotor performances and transition locations on the blade surfaces with the experimental data. Overall, the transition model captures the first-order effect of transition on the rotor performances well. However, predicted transition locations on the upper surface of the blade shows peculiar behaviors regardless of collective pitch angles as shown in Fig. 1.18. Vieira et al. [49]

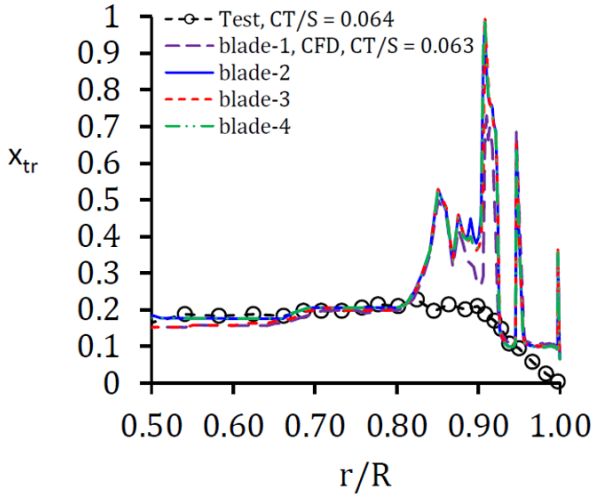

Figure 1.18: Comparison of transition locations on the upper surface of the blade. Image reproduced from Jain (2017) [5]

conducted the isolated rotor simulations using STAR-CCM$^+$ with Coder's AFT transition model (old version). For transition simulations, $N_{crit} = 9$ is specified as transition criteria. Although the transition model gives promising results in the rotor performance and transition locations, a slope of Figure of Merit from the transition simulations changes irregularly as the thrust level increases. Later, Parwani and Coder [50] and Carnes and Coder [35] performed similar simulations including the fuselage using OVERFLOW flow solver with the latest version of AFT transition model. Lee et al. [18] investigated the effect of a transition model with and without a crossflow transition correction using OVERTURNS flow solver with the Medida-Baeder transition model. In the work, non-Galilean invariant variables were modified with the local velocity vector relative to the blade wall to account for the grid motion. Overall, transition simulations give good comparisons of the integrated rotor performance with the experiment, but transition simulations require quite high freestream turbulence intensity, 0.75%. It was not published, but transition simulations were also performed without the modifications of non-Galilean invariant variables. In such case, a lower freestream turbulence intensity, 0.075% gives better comparisons with the experimental data. However, the results show unphysical earlier transition on the lower surface of the blade near the swept tip, which was similarly observed in S-76 rotor simulations. In the work by Kwon et al. [19, 20], a high freestream turbulence intensity value (1.0%) was used with Langtry-Menter's transition model. It is considered that they also performed simulations with the modifications of transition model to account for the motion of the blade. Similar numerical studies are performed by Zhao et al. [51, 52] using UN^{2}CLE flow solver

with Langtry-Metner's model, and Fitzgibbon et al. [53] using HMB flow solver with Menter's 1-eq transition model, but they do not include information of the turbulence intensity in the papers. It is not a PSP rotor simulation, but Kaufmann et al. [31] reported that Langtry-Menter's model gives too delayed transition on a rotor blade when turbulence intensity is lower than 1% in simulations accounting for the rotating frame of reference. On the contrary, the semi-empirical method predicts transition locations reasonably with turbulence intensity around 0.08%. It is not clarified how the rotating frame of reference was accounted for, but a high turbulence intensity value around 1% is required in the paper to match the experimental data.

Several numerical work are reviewed here, but they have similar issues, which can be summarized as follows:

1) A correct range of free stream turbulence intensity is not clear for a rotor simulation. The freetream turbulence intensity is one of the most important parameter in transition simulations. For fixed wing aircraft, a typical range of freestream turbulence intensity is from 0.07% ($N_{crit} = 9$) to 0.161% ($N_{crit} = 7$). However, for rotorcraft, it has not been measured in an experiment, and its correct range is still unknown. In the CFD simulations mentioned above, the freestream turbulence intensity varies from 0.07% to 1%, the maximum values is more than ten times larger than the minimum value.

2) Non-Galilean invariant transition models such as Langtry-Menter or Medida-Baeder model depend on the frame of reference. For simulations in the inertial frame of reference, the transition models give reasonable prediction of the rotor perfor-

mances with freestream turbulence intensity less than 0.1%. However, in such cases, the transition models show unphysical behaviors in transition locations regardless of thrust levels as shown in Jain [5] and Lee [17]. On the other hand, in transition simulations accounting for the grid motion or rotational frame of reference, high freestream turbulence intensity around 1% is required to match experimental data. It is not clear whether such high freestream turbulence intensity is reasonable or not for rotor simulations.

3) For transition simulations with the SST turbulence model, detailed information of implementation of the turbulence model are not clarified. For the SST turbulence model, there are nonphysical decay mechanisms of turbulence quantities, so the sustaining terms or decay limiters are proposed to prohibit that [54]. Employing the terms change the behavior of transition models. In addition, there are many variants of the SST turbulence model with different source terms such as SST [14], SST-V [30], and SST-KL [55]. All these variations affects transition predictions, but this information is not included in many papers.

1.3.2 Wake breakdown of a hovering rotor

This section reviews numerical and experimental work of wake breakdown of a hovering rotor. In numerical simulations, wake breakdown by the secondary vortex braids (also called "vortical worms" or "vortex soup") is observed in simulations with the adaptive mesh refinement (AMR) and/or high-order numerical schemes. Figure 1.19 shows development of the wake break down of UH-60A rotor by Hari-

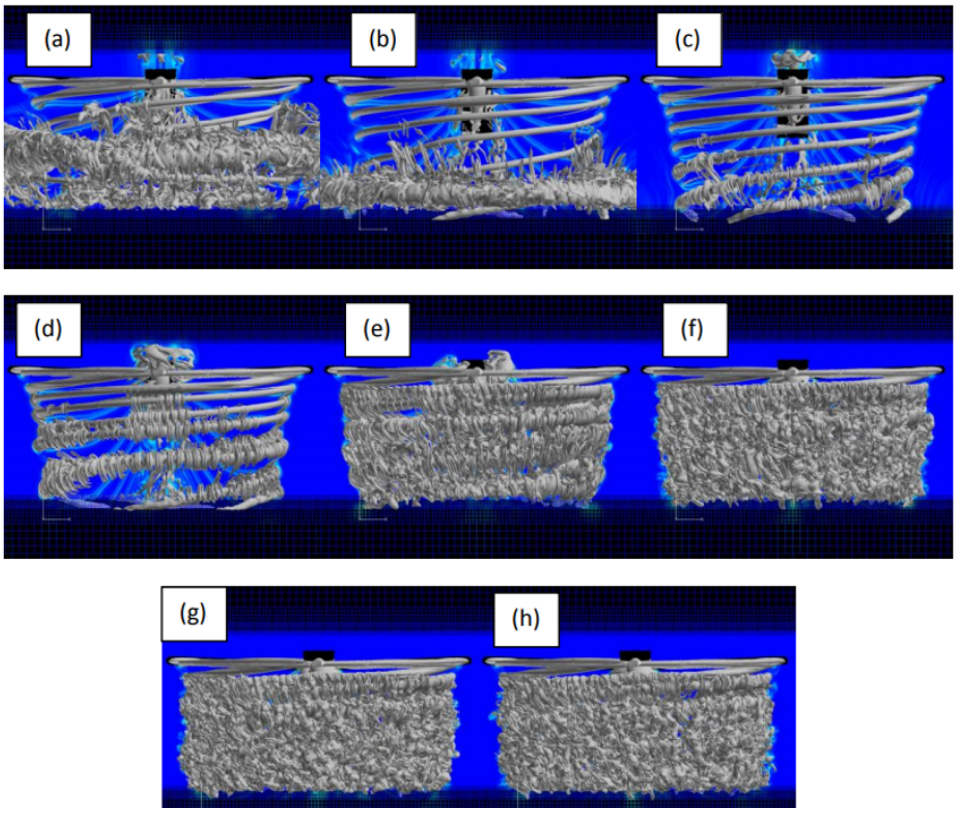

Figure 1.19: Development of wake breakdown by secondary vortex structures: UH-60A hover simulations at time steps 30, 40, 50, 60, 70, 80, 90, 100 thousand steps. Image reproduced from Hariharan et at. [6].

haran et al. [6] using CREATE-AV Helios. NSU3D was used for a near-body solver and the fifth-order accurate invicid flow solver (SAMRC) was applied for off-body simulations. The adaptive mesh refinement was performed, and the simulation was conducted using the rotational source terms. In the figure, after the starting vortex leaves the refinement region (Figs. (a) and (b)), the "secondary vortex braids" appear although the wake structures are still stable (Fig. (c)). Then, the secondary vortex braids propagate to the entire flow field and make the wake structures unstable (Fig. (d) and Fig. (e)). Finally, vortical structures are destroyed by the instabilities (Fig. (f)). Chaderjian and Buning [21] conducted hover simulations of the 3-bladed Tilt Rotor Aeroacoustics Model (TRAM) using OVERFLOW with 5th

order spatial scheme and the SA-DES model. In the work, two levels of the AMR are performed with the finest cell size of 2.5% of the tip chord length. Figure. 1.20(a) shows small "vortical worms" dominate the entire wake structures except the very near wake region. Jain [56] performed a hovering rotor simulations for 4-blade S-

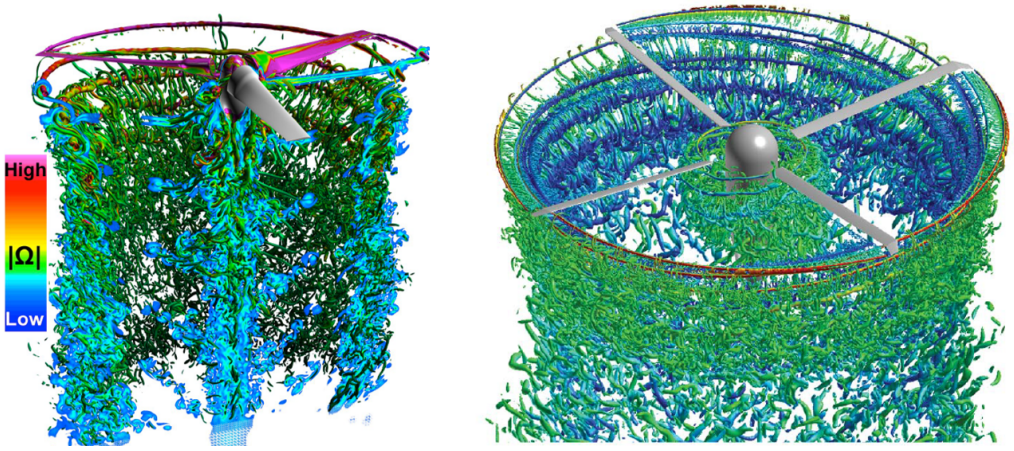

(a) The TRAM rotor. Image reporduced from Chaderjian and Buning [21].

(b) S-76 rotor. Image reproduced from Jain [56].

Figure 1.20: Wake breakdown of high-resolution hover simulations.

76 rotor using OVERFLOW with the fifth order central scheme, SA-DES model, and the AMR with the finest cell size of 2.5% of the reference chord length. Figure 1.20(b) shows the tip vortical structures become unstable within one revolution by vortical "wormlike" structures. In addition to the previous work, other CFD work also shows similar phenomena for S-76 rotor [4, 57], and PSP rotor [5, 18, 50] using the AMR and/or high-order numerical schemes.

On the other hand, there have been very limited experimental work that identifies the secondary vortex. Wolf et al. [7] recently performed experiments on a subscale rotor in ground effect and investigated wake structures using the time-resolved

particle tracking method. Figure 1.21 show a part of the measured wake structures from the experiment. In the figure, the secondary vortex braids are observed between the tip vortices. However, the extent of the vortex braids in the experiment is still much less than that of CFD simulations. More experimental studies are required, but the wake breakdown in CFD simulations, only stable vortical structure in the very near wake, is considered physically incorrect.

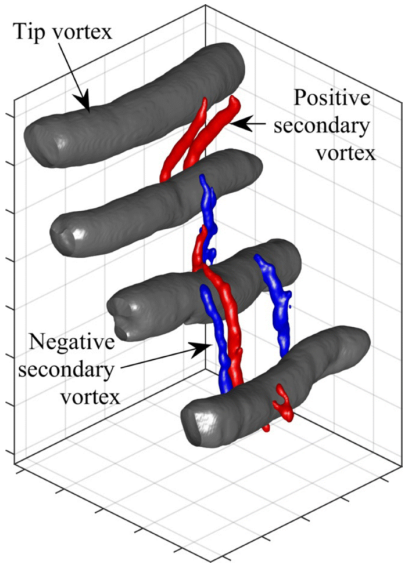

Figure 1.21: Experiment measurement of the secondary vortex structures on a subscale rotor. Image reproduced from Wolf et al. [7].

There have been several numerical studies to identify factors causing the wake breakdown in CFD simulations. Significant efforts are made by Abras, Hariharan, and Narducci [24–26]. In their work, several factors are investigated for S-76 blade such as 1) the number of blades, 2) flow solver, 3) turbulence model, and 4) off-body grid. Among them, the type of off-body grids is one of the key factors affecting the wake structures, and a rotating torus mesh with the blades reduces non-physical wake breakdown the most. The authors considered that a potential "culprits" is the

data transfer between the overset boundaries, and the numerical issue exacerbates the wake breakdown with some types of off-body meshes.

The current author also looked at the effect of the temporal accuracy on the wake breakdown [17]. In the work, the BDF2 and BDF1 schemes were investigated, and a reduced temporal accuracy from 2nd-order to 1st-order gives less unphysical secondary vortex braids with minor changes in the rotor performances. However, the BDF1 scheme removed entire secondary vortex braids, and it may not be physical either considering the experimental work by Wolf et al. [7]. In addition, the previous work only considered the BDF2 and BDF1 schemes and did not investigate other time-maching factors such as time step sizes or temporal damping of the BDF scheme. To better understand wake breakdown and suggest an engineering solutions, further analyses are required with various time-marching factors.

1.4 Objectives

The present study has two primary research objectives: 1) Development of a Galilean invariant transition model for the S-A turbulence model, and 2) Further investigation of the effect of time marching on wake breakdown of a hovering rotor.

For the first objective, the S–A turbulence model is chosen as a baseline turbulence model instead of the SST turbulence model. The S-A turbulence model has been widely validated for external flows and has a capability for hybrid RANS/LES simulations. In addition, the S-A turbulence model has less variants of the source terms and doesn't require sustaining terms or decay limiters unlike the SST turbu-

lence model.

For the transition model, it should be Galilean invariant to avoid the dependence on the frame of reference. Moreover, for an input of transition simulations, the model should use a physical value from experiments instead of a numerical value such as the initial condition of the S–A turbulence model ($\tilde{\nu}$). The transition model also should meet the following requirements:

- Able to predict various transition mechanisms such as natural transition, separation-induced transition, bypass transition, and crossflow transition.
- Fully local and compatible with both structured/unstructured meshes.
- Give good convergence for implicit time-marching methods.
- Robust results for various meshes and/or Reynolds numbers.

Finally, for rotor simulations, the transition model should predict rotor performance reasonably within a typical range of the freestream turbulence intensity without non-physical behaviors. Although there are no experimental evidence yet, the current author believes that a correct range of the freestream turbulence intensity in rotor simulations is not around 1.0% that can cause bypass transition but instead closer to 0.1%, which is a range of natural transition more comparable to that for a fixed wing aircraft.

The second objective of the present study is to investigate the effect of time marching on wake breakdown with various factors such as time step sizes, the BDF2 and BDF1 schemes, and temporal damping of the BDF scheme. To control the

temporal damping of the BDF scheme, a new formulation of the BDF scheme needs to be derived with a damping variable. In addition, the formulation should be coupled to dual-time stepping for unsteady simulations. The final goal of the present analysis is to propose an engineering solution to reduce unphysical wake breakdown of a hovering rotor without significant loss of the temporal accuracy.

1.5 Scope and Organization of Thesis

Chapter 1 discusses the motivation, background, literature review, and research objective of the present work. The remainder of the dissertation is as follows:

- Chapter 2 presents numerical methodology of the present study. The work is performed using a compressible, structured, finite volume, hybrid RANS/LES flow solver, OVERTURNS. The section gives details about the flow solver including the governing equations and numerical algorithms. Also, a blended BDF scheme coupled to dual-time stepping is derived.

- Chapter 3 derives formulations of the SA-γ transition model. First of all, Menter's 1-eq γ transition model is presented. Secondly, integration with the S–A turbulence model is discussed with improvements in the convergence of the transition model. Finally, the extension of the transition model with crossflow transition models are shown.

- Chapter 4 provides validation cases of the SA-γ transition model for various two-dimensional and three-dimensional cases including flow overs flat plate,

airfoils, and a hovering rotor. The chapter shows the accuracy and robustness of the transition model for various flow conditions and meshes.

- Chapter 5 discusses the effect of the time-marching on wake breakdown of a hovering rotor. Various factors such as time step sizes, time-marching schemes, and temporal damping of the time-marching schemes are investigated. The chapter shows that adding a small amount of temporal damping to the BDF2 scheme can be used as an engineering solution for reducing unphysical wake breakdown of a hovering rotor.

- Finally, in Chapter 6, conclusions and an overall summary of the present study is presented with recommendations for future work.

Chapter 2: Computational Methodology

The following chapter discusses numerical methods of the present work. The work is performed using Overset Transonic Unsteady Rotor Navier–Stokes (OVERTURNS) [58] flow solver. OVERTURNS is compressible, structured, finite volume, hybrid RANS/LES flow solver and has been developed at the University of Maryland over decades. In the first section of the chapter, the governing equations and their modifications are discussed. Then, in the second part, numerical algorithms employed in OVERTURNS flow solver are presented.

2.1 Governing equations

2.1.1 Navier–Stokes Equations

To describe the behavior of flow, the three-dimensional, unsteady, compressible Navier–Stokes equations are employed as the governing equations, consisting of conservation of mass, momentum, and energy. In the Cartesian coordinate system, Navier–Stokes equations in the strong conservation form are expressed as

$$\frac{\partial Q}{\partial t} + \frac{\partial F_i}{\partial x} + \frac{\partial G_i}{\partial y} + \frac{\partial H_i}{\partial z} = \frac{\partial F_v}{\partial x} + \frac{\partial G_v}{\partial y} + \frac{\partial H_v}{\partial z} + S \tag{2.1}$$

where Q is the vector of conserved variables, F_i, G_i and H_i are the inviscid flux vectors, F_v, G_v and H_v are the viscous flux vectors, and S is the vector of sources from body forces or effects of a frame of reference.

The vector of conserved variables, Q, is given

$$Q = \begin{Bmatrix} \rho \\ \rho u \\ \rho v \\ \rho w \\ e \end{Bmatrix} \tag{2.2}$$

where ρ is the density, u, v, w are velocity components in the Cartesian coordinate, and e is the total energy per unit volume.

The inviscid flux vectors, F_i, G_i, H_i, are given by

$$F_i = \begin{Bmatrix} \rho u \\ \rho u^2 + p \\ \rho uv \\ \rho uw \\ u(e+p) \end{Bmatrix}, \quad G_i = \begin{Bmatrix} \rho v \\ \rho vu \\ \rho v^2 + p \\ \rho vw \\ v(e+p) \end{Bmatrix}, \quad H_i = \begin{Bmatrix} \rho w \\ \rho wu \\ \rho wv \\ \rho w^2 + p \\ w(e+p) \end{Bmatrix} \tag{2.3}$$

where p is the pressure from the equation of state for a perfect gas as

$$p = (\gamma - 1)\left\{ e - \frac{1}{2}(u^2 + v^2 + w^2) \right\} \tag{2.4}$$

with the ratio of specific heat (γ) of 1.4 for air.

The viscous flux vectors, F_v, G_v, H_v, are given by

$$F_v = \begin{Bmatrix} 0 \\ \tau_{xx} \\ \tau_{yx} \\ \tau_{zx} \\ u\tau_{xx} + v\tau_{yx} + w\tau_{zx} - q_x \end{Bmatrix} \tag{2.5}$$

$$G_v = \begin{Bmatrix} 0 \\ \tau_{xy} \\ \tau_{yy} \\ \tau_{zy} \\ u\tau_{xy} + v\tau_{yy} + w\tau_{zy} - q_y \end{Bmatrix} \tag{2.6}$$

$$H_v = \begin{Bmatrix} 0 \\ \tau_{xz} \\ \tau_{yz} \\ \tau_{zz} \\ u\tau_{xz} + v\tau_{yz} + w\tau_{zz} - q_z \end{Bmatrix} \tag{2.7}$$

where q_x, q_y, and q_z are thermal conduction terms expressed as as a function of temperature, T, and coefficient of thermal conductivity, k, as follows:

$$q_i = -k\frac{\partial T}{\partial x_i} \quad (i = x, y, z) \tag{2.8}$$

The viscous stress, τ_{ij}, is formulated based on Stokes' hypothesis as

$$\tau_{ij} = \mu \left[\left(\frac{\partial u_i}{\partial x_j} + \frac{\partial u_j}{\partial x_i} \right) - \frac{2}{3} \frac{\partial u_k}{\partial x_k} \delta_{ij} \right] \tag{2.9}$$

where μ is molecular viscosity calculated using Sutherlands law and δ_{ij} is the Kronecker delta.

Most simulations in this dissertation do not include body forces. However, for three-dimensional hovering rotor simulations, the source vector, S, is applied to employ advantages of the rotating frame of reference. The rotating frame of reference and source vector are described in the following section.

2.1.2 Simulation in the rotating frame of reference

For a general unsteady simulation with moving bodies, the governing equations are solved in the inertial frame of reference. In such case, an overset connectivity between meshes should be searched at every time-step with re-calculations of the metric terms. On the other hand, for a hovering rotor, the governing equation can be solved in the rotating frame of reference. In this case, computational costs can be saved, since the calculations of the overset connectivity and metric terms are only required at the beginning of a simulation. A simulation in the rotating frame of reference requires 1) modifications of the governing equations (i.e., momentum equations) and 2) source terms accounting for the Coriolis and centrifugal forces. The modified momentum equations from Eq. 2.3 are

$$F_i = \begin{Bmatrix} \rho(u-u_g) \\ \rho(u-u_g)u+p \\ \rho(u-u_g)v \\ \rho(u-u_g)w \\ (u-u_g)(e+p) \end{Bmatrix}, \quad G_i = \begin{Bmatrix} \rho(v-v_g) \\ \rho(v-v_g)u \\ \rho(v-v_g)v+p \\ \rho(v-v_g)w \\ (v-v_g)(e+p) \end{Bmatrix}, \quad H_i = \begin{Bmatrix} \rho(w-w_g) \\ \rho(w-w_g)u \\ \rho(w-w_g)v \\ \rho(w-w_g)w+p \\ (w-w_g)(e+p) \end{Bmatrix} \tag{2.10}$$

where $U_g = (u_g, v_g, w_g) = \Omega \times r$ is the vector of grid velocities and $\Omega = (\Omega_x, \Omega_y, \Omega_z)$ is the vector of angular velocities. For a hovering rotor rotating about z-axis, angular velocities are $\Omega = (0, 0, \Omega_z)$, and thus, grid velocities are $U_g = (-y\Omega_z, x\Omega_z, 0)$. Also, the rotational source terms accounting for the Coriolis and centrifugal forces, S, are given as

$$S = \begin{Bmatrix} 0 \\ \rho v \Omega_z \\ -\rho u \Omega_z \\ 0 \\ 0 \end{Bmatrix} \tag{2.11}$$

2.1.3 Non-dimensionalization of the Navier–Stokes Equations

The governing equations are non-dimensionalized for the similarity. The non-dimensionaliation of variables is performed using the reference variables as:

$$t^* = \frac{ta_\infty}{c}, \quad x^* = \frac{x}{c}, \quad y^* = \frac{y}{c}, \quad z^* = \frac{z}{c} \tag{2.12}$$

$$\mu^* = \frac{\mu}{\mu_\infty}, \quad u^* = \frac{u}{a_\infty}, \quad v^* = \frac{v}{a_\infty}, \quad w^* = \frac{w}{a_\infty} \tag{2.13}$$

$$\rho^* = \frac{\rho}{\rho_\infty}, \quad T^* = \frac{T}{T_\infty}, \quad p^* = \frac{p}{\rho_\infty a_\infty}, \quad e^* = \frac{e}{\rho_\infty a_\infty} \tag{2.14}$$

where the superscript $*$ represents a non-dimensionalized variables, the subscript ∞ represents free-stream conditions, c is the chord of the airfoil, and a is the speed of sound. The above variables are substituted into the Navier-Stoke equations, and then it results in the identical equations except the viscous stress and thermal conduction terms:

$$\tau_{ij} = \frac{\mu M_\infty}{a_\infty}\left[\left(\frac{\partial u_i}{\partial x_j} + \frac{\partial u_j}{\partial x_i}\right) - \frac{2}{3}\frac{\partial u_k}{\partial x_k}\delta_{ij}\right] \tag{2.15}$$

$$q_i = -\frac{\mu M_\infty}{Re_\infty Pr(\gamma - 1)}\frac{\partial T}{\partial x_i} \tag{2.16}$$

where M_∞, Re_∞, Pr are Mach number, Reynolds number, and Prandtl number, respectively, defined as

$$M_\infty = \frac{V_\infty}{a_\infty}, \quad Re_\infty = \frac{\rho_\infty V_\infty c}{\mu_\infty}, \quad Pr = \frac{\mu_\infty c_p}{k} \tag{2.17}$$

where V_∞ is a magnitude of the freestream velocity and c_p is the specific heat at constant pressure. At the standard air conditions, the Prandtl number is assumed $Pr = 0.72$. The superscript $*$ is intentionally dropped in Eqs. 2.15 and 2.16 for simplicity.

2.1.4 Reynolds-Averaged Navier–Stokes

Direct simulation of the time-dependent Navier–Stokes equations, called Direct Numerical Simulation (DNS), or Large Eddy Simulations (LES) is prohibitively expensive for practical engineering problems at high Reynolds numbers. As an alternative to DNS or LES, the current work employs the Reynolds-Averaged Navier–Stokes (RANS) approach, resolving statistically steady turbulence without transient features. In the RANS approach, flow variables are decomposed into the mean and fluctuation parts, called Reynolds decomposition, as:

$$f = \overline{f} + f' \tag{2.18}$$

where $\overline{f}$ is the mean part and f' is the fluctuation part. The mean part, $\overline{f}$, is defined as

$$\overline{f} = \lim_{\Delta t \to \infty} \frac{1}{\Delta t} \int_t^{t+\Delta t} f(t) dt \tag{2.19}$$

Also, by the definition, time-averaging of the fluctuation part is

$$\overline{f}' = \lim_{\Delta t \to \infty} \frac{1}{\Delta t} \int_t^{t+\Delta t} f(t)' dt = 0 \tag{2.20}$$

Substitution of the decomposed flow variables into the Navier-Stokes equations and time-averaging of the equations give Reynolds-Averaged Navier–Stokes (RNAS) equations. Many fluctuation terms cancel out because of the time-averaging, and the resultant equations are identical to the Navier-Stokes equations except the time-averaging variables in the equations and additional terms in the momentum and energy equations. The additional term in the momentum equation is known as the Reynolds-stress tensor and calculated based on Boussinesq's eddy viscosity hypothesis using a turbulence model as

$$(\overline{\tau_{ij}})_{turb} = -\rho\overline{u_i' u_j'} \approx 2\mu_t \left(\overline{S_{ij}} - \frac{1}{3}\frac{\partial \overline{u_k}}{\partial x_k}\delta_{ij}\right) - \frac{2}{3}\overline{\rho} k \delta_{ij} \tag{2.21}$$

where $\overline{S_{ij}}$ is the strain rate tensor, and k is the turbulent kinetic energy, and μ_t is the turbulent eddy viscosity. To calculate the turbulent eddy viscosity, μ_t, the Spalart-Allmaras one-equation turbulence model [13] is applied in the present work. Details of the turbulence model is given in Chapter 2.1.5. The additional term in the energy equations is ignored, since there is no heat transfer.

2.1.5 Turbulence model

The present work calculates the turbulent eddy viscosity using the Spalart-Allmaras (SA) one-equation turbulence model [13]. The model consists of a transport equation for a working variable, $\tilde{\nu}$, as

$$\frac{D\tilde{\nu}}{Dt} = c_{b1}\tilde{S}\tilde{\nu} - c_{w1} f_w \left(\frac{\tilde{\nu}}{d}\right)^2 + \frac{1}{\sigma}\left[\nabla \cdot ((\nu + \tilde{\nu})\nabla\tilde{\nu}) + c_{b2}(\nabla\tilde{\nu})^2\right] \tag{2.22}$$

where d is the distance from the nearest wall and ν is the molecular viscosity. The original SA model has a trip term, f_{t2}, but it is often unused in many implementations. This version of the SA turbulence model is called SA-noft2, and the present work also employs the SA-noft2 version. Other variables of the model are given as

$$\tilde{S} = \Omega + \frac{\tilde{\nu}}{k^2 d^2} f_{v2}, \quad f_{v2} = 1 - \frac{\chi}{1 + \chi f_{v1}}, \quad \chi = \frac{\tilde{\nu}}{\nu}, \quad f_{v1} = \frac{\chi^3}{\chi^3 + c_{v1}^3} \tag{2.23}$$

$$f_w = g \left[\frac{1 + c_{w3}^6}{g^6 + c_{w3}^6} \right]^{1/6}, \quad g = r + c_{w2}(r^6 - r), \quad r = min \left[\frac{\tilde{\nu}}{\tilde{S} k^2 d^2}, 10 \right] \tag{2.24}$$

The model constants are

$$c_{b1} = 0.1355, \quad \sigma = 2/3, \quad c_{b2} = 0.622, \quad \kappa = 0.41 \tag{2.25}$$

$$c_{w2} = 0.3, \quad c_{w3} = 2, \quad c_{v1} = 7.1, \quad c_{w1} = \frac{c_{b1}}{\kappa^2} + \frac{1 + c_{b2}}{\sigma} \tag{2.26}$$

After the transport equation for $\tilde{\nu}$ is solved, the turbulent eddy viscosity is calculated as

$$\mu_t = \rho \tilde{\nu} f_{v1} \tag{2.27}$$

2.1.5.1 Rotation correction of the SA model

The production term of the SA turbulence model is proportional to the magnitude of the vorticity. However, this causes excessive generation of the turbulent eddy viscosity in pure rotation regions, such as vortex cores, that should not generate turbulence. To remedy this, the rotation correction of the SA turbulence model [59]

is employed to reduce the turbulent eddy viscosity generation in regions where the vorticity exceeds the strain rate. In the correction, the magnitude of vorticity Ω in Eq. 2.23 is replaced with

$$\Omega + C_{rot} min(0, S - \Omega), \quad C_{rot} = 2.0, \quad S = \sqrt{2 S_{ij} S_{ij}}, \quad S_{ij} = \frac{1}{2}\left(\frac{\partial u_i}{\partial x_j} + \frac{\partial u_j}{\partial x_i}\right) \tag{2.28}$$

2.1.6 Curvilinear Coordinate Transformation

The governing equations in a non-uniform spaced Cartesian coordinate system (physical domain) is transformed onto an equispaced curvilinear coordinate system (computational domain) as shown in Fig. 2.1. The transformation is performed using the chain-rule of derivative as:

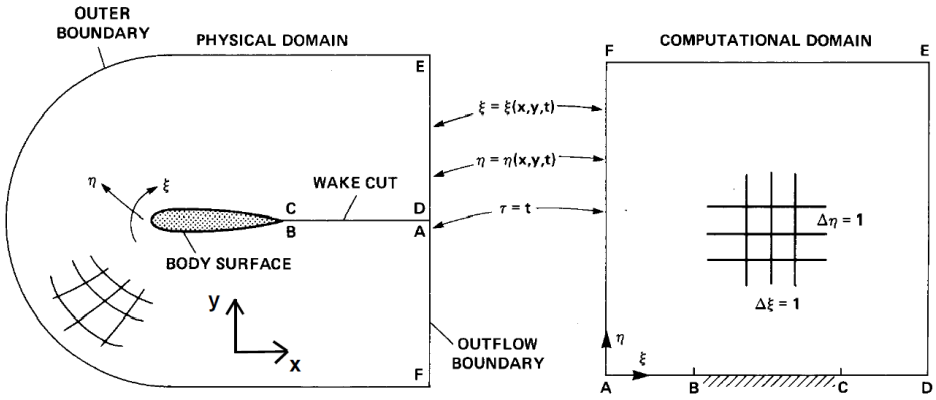

Figure 2.1: Curvilinear coordinate transformation of physical domain onto computational domain. Image reproduced from [8].

$$\frac{\partial \hat{Q}}{\partial t} + \frac{\partial \hat{F}}{\partial \xi} + \frac{\partial \hat{G}}{\partial \eta} + \frac{\partial \hat{H}}{\partial \zeta} = \hat{S} \tag{2.29}$$

where

$$\hat{Q} = \frac{1}{J}Q \tag{2.30}$$

$$\hat{F} = \frac{1}{J}[\xi_t Q + \xi_x(F_i - F_v) + \xi_y(G_i - G_v) + \xi_z(H_i - H_v)] \tag{2.31}$$

$$\hat{G} = \frac{1}{J}[\eta_t Q + \eta_x(F_i - F_v) + \eta_y(G_i - G_v) + \eta_z(H_i - H_v)] \tag{2.32}$$

$$\hat{H} = \frac{1}{J}[\zeta_t Q + \zeta_x(F_i - F_v) + \zeta_y(G_i - G_v) + \zeta_z(H_i - H_v)] \tag{2.33}$$

$$\hat{S} = \frac{1}{J}S \tag{2.34}$$

and $J = det\left(\frac{\partial(\xi,\eta,\zeta)}{\partial(x,y,z)}\right)$ is the Jacobian of the coordinate transformation.

2.2 Numerical Algorithm

This section present numerical algorithms employed in OVERTURNS for solving the governing equations

2.2.1 Finite Volume

The curvilinear form of the governing equations are spatially discretized using the node-based finite volume method. In the method, a fictitious volume, called control volume, is created around grid points by joining the interfaces passing the midpoints of two grid points as shown in Fig. 2.2 (2-D control volume for a simplicity). Inviscid and viscous fluxes are calculated at the faces of the control volume. The governing equations are discretized based on the node-based finite volume method

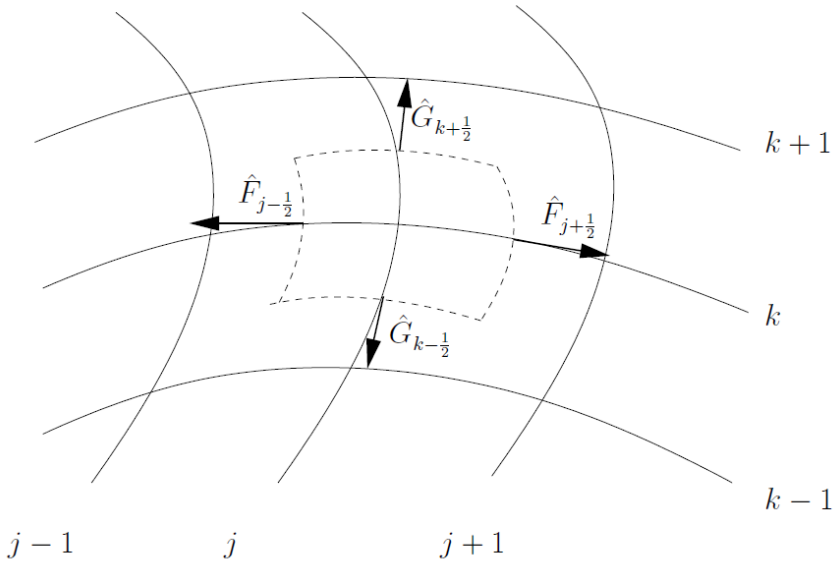

Figure 2.2: Schematic of the control volume. Image reproduced from [9].

as

$$\frac{\partial \hat{Q}}{\partial t} = -\frac{\hat{F}_{j+\frac{1}{2}} - \hat{F}_{j-\frac{1}{2}}}{\Delta\xi} - \frac{\hat{G}_{k+\frac{1}{2}} - \hat{G}_{k-\frac{1}{2}}}{\Delta\eta} - \frac{\hat{H}_{l+\frac{1}{2}} - \hat{H}_{l-\frac{1}{2}}}{\Delta\zeta} + \hat{S}_{j,k,l} \tag{2.35}$$

where (j, k, l) are the indices in the (ξ, η, ζ) directions, respectively, and $(j \pm \frac{1}{2}, k \pm \frac{1}{2}, l \pm \frac{1}{2})$ are interfaces of the control volume.

2.2.2 Inviscid Flux

In OVERTURNS, inviscid fluxes are calculated in two steps: (1) reconstruction of the primitive variables at cell interfaces, and (2) evaluation of inviscid fluxes from the left and right states using a flux difference scheme. Figure 2.3 shows a schematic of the left and right states at a cell interface for a simple one-dimensional case. The left and right states at the cell interface are calculated using the third-order Monotone Upstream-Centered Scheme for Conservation Laws (MUSCL3) [60] or the fifth-order Weighted Essentially Non-Oscillatory (WENO5) [61]. Then, the

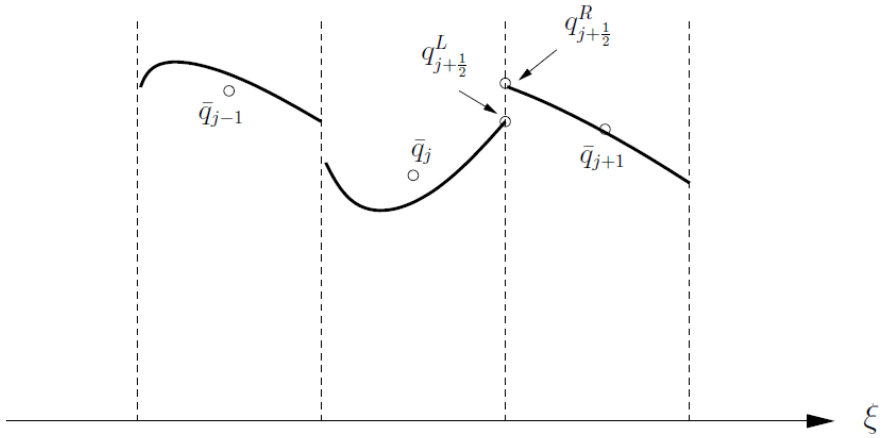

Figure 2.3: Schematic of one dimensional piecewise reconstruction. Image reproduced from [9].

left and right states can be considered as a local Riemann problem, and inviscid fluxes are computed using Roe's flux difference splitting (FDS) scheme [62] at the each interface as

$$F(q^L, q^R) = \frac{F(q^L) + F(q^R)}{2} - |\hat{A}(q^L, q^R)|\frac{q^R - q^L}{2} \tag{2.36}$$

where q^L, q^R are the left and right states, and $\hat{A}$ is the Roe-averaged Jacobian matrix. Harten's entropy correction [63] is employed to modify the eigenvalues of the Jacobian matrix to avoid nonphysical behaviors of the Roe scheme. As stated earlier, reconstruction of the primitive variables is perform using either MUSCL3 or WENO5 scheme. Each scheme is further discussed in the following sections.

2.2.2.1 MUSCL3 scheme

The third-order Monotone Upstream-Centered Scheme for Conservation Laws (MUSCL3) [60] is given as

$$q^L_{i+1/2} = \bar{q}_i + \phi_i \left[\frac{1}{3}(\bar{q}_{i+1} - \bar{q}_i) + \frac{1}{6}(\bar{q}_i - \bar{q}_{i-1}) \right] \tag{2.37}$$

$$q^R_{i-1/2} = \bar{q}_i - \phi_i \left[\frac{1}{3}(\bar{q}_{i+1} - \bar{q}_i) + \frac{1}{6}(\bar{q}_i - \bar{q}_{i-1}) \right] \tag{2.38}$$

where $q^L_{i+1/2}$ and $q^R_{i-1/2}$ are reconstructed variables, $q^-_{i+1}, \bar{q}_i, q^-_{i-1}$ are the cell-averaged values, and ϕ is Koren's differentiable limiter [64] defined as:

$$\phi_i = \frac{3\Delta\bar{q}_i\nabla\bar{q}_i + \epsilon}{2(\Delta\bar{q}_i - \nabla\bar{q}_i)^2 + 3\Delta\bar{q}_i\nabla\bar{q}_i + \epsilon} \tag{2.39}$$

where ϵ is a small number ($= 10^{-6}$) to prevent division by zero, and Δ and ∇ are forward and backward difference operators, respectively, defined as $\Delta\bar{q}_i = (\bar{q}_{i+1} - \bar{q}_i)$ and $\nabla\bar{q}_i = (\bar{q}_i - \bar{q}_{i-1})$. The MUSCL3 has third-order of accuracy in smooth regions, whereas it reduces the order of accuracy to the first order at high gradient regions such as shock discontinuities.

2.2.2.2 WENO5 scheme

The fifth-order Weighted Essentially Non-Oscillatory (WENO5) [61] is defined as

$$q^L_{i+\frac{1}{2}} = \sum_{r=0}^{2} w_r \hat{f}^L_r \tag{2.40}$$

where w_r are the weights defined as

$$w_r = \frac{\alpha_r}{\sum_{s=0}^{2} \alpha_s}, \quad \alpha_r = \frac{d_r}{(\beta_r + \epsilon)^p} \tag{2.41}$$

The ideal weights, d_r are given as

$$d_0 = \frac{1}{10}, \quad d_1 = \frac{3}{5}, \quad d_2 = \frac{3}{10} \tag{2.42}$$

The smoothness indicators β_k are defined as

$$\begin{aligned}
\beta_0 &= \frac{13}{12}(\bar{q}_{i-2} - 2\bar{q}_{i-1} + \bar{q}_i)^2 + \frac{1}{4}(\bar{q}_{i-2} - 4\bar{q}_{i-1} + 3\bar{q}_i)^2 \\
\beta_1 &= \frac{13}{12}(\bar{q}_{i-1} - 2\bar{q}_i + \bar{q}_{i+1})^2 + \frac{1}{4}(\bar{q}_{i-1} - \bar{q}_{i+1})^2 \\
\beta_2 &= \frac{13}{12}(\bar{q}_i - 2\bar{q}_{i+1} + \bar{q}_{i+2})^2 + \frac{1}{4}(3\bar{q}_i - 4\bar{q}_{i+1} + \bar{q}_{i+2})^2
\end{aligned} \tag{2.43}$$

The three stencil lists are

$$\begin{aligned}
\hat{f}_0^L &= \frac{1}{6}(2\hat{q}_{i-2} - 7\hat{q}_{i-1} + 11\hat{q}_i) \\
\hat{f}_1^L &= \frac{1}{6}(-\hat{q}_{i-1} + 5\hat{q}_i + 2\hat{q}_{i+1}) \\
\hat{f}_2^L &= \frac{1}{6}(2\hat{q}_i + 5\hat{q}_{i+1} - \hat{q}_{i+2})
\end{aligned} \tag{2.44}$$

The WENO5 scheme has the fifth-order of accuracy at smooth regions, whereas it becomes third-order at discontinuities and/or high gradient regions. The WENO5 scheme with the weights shown above is often called WENO5-JS. Henrick et al. [65] and Borges et al. [66] propose different weights, and their versions of the WENO5 scheme are called WENO5-M and WENO5-Z, respectively. They are also available

in OVERTURNS flow solver.

2.2.3 Viscous Flux

Inviscid fluxed were computed using the upwinding Roe scheme that accounts for directions of wave propagation. On the other hand, viscous fluxes are calculated using the central differencing. Viscous fluxes shown Eqs. 2.5-2.7 are expressed as derivative terms in the following form:

$$\frac{\partial}{\partial \xi}\left(\alpha \frac{\partial \beta}{\partial \eta}\right) \tag{2.45}$$

They are calculated using the second order central differing as:

$$\frac{1}{2}\left(\left[\alpha_{j+\frac{1}{2},k}\frac{\beta_{j+\frac{1}{2},k+1}-\beta_{j+\frac{1}{2},k}}{\Delta\eta}\right]-\left[\alpha_{j-\frac{1}{2},k}\frac{\beta_{j-\frac{1}{2},k}-\beta_{j-\frac{1}{2},k-1}}{\Delta\eta}\right]\right) \tag{2.46}$$

where $\delta_{j+\frac{1}{2},k}=\frac{\delta_{j,k}+\delta_{j+1,k}}{2}$ and $\delta=(\alpha,\beta)$

2.2.4 Time Integration

After the calculations of the inviscid and viscous fluxes, the time integration is performed for the vector of the conservative variables, Q. The time integration can be performed using either an explicit or implicit method. An explicit method doesn't require expensive matrix inversions. However, it has the stability restriction on time step size and thus not suitable for stiff problems such as viscous flow or boundary layer simulations. In the current work, an implicit time marching method, the first

order or second order Backward Difference Formula (BDF) is employed. Both BDF1 and BDF2 are unconditionally stable (A-stable). The governing equations with the BDF1 or BDF2 are written as

$$\frac{\partial \hat{Q}^{n+1}}{\partial t} = -\frac{\hat{F}^{n+1}_{j+\frac{1}{2}} - \hat{F}^{n+1}_{j-\frac{1}{2}}}{\Delta\xi} - \frac{\hat{G}^{n+1}_{k+\frac{1}{2}} - \hat{G}^{n+1}_{k-\frac{1}{2}}}{\Delta\eta} - \frac{\hat{H}^{n+1}_{l+\frac{1}{2}} - \hat{H}^{n+1}_{l-\frac{1}{2}}}{\Delta\zeta} + \hat{S}^{n+1}_{j,k,l} \tag{2.47}$$

where the left hand side with BDF1 is

$$\frac{\partial \hat{Q}^{n+1}}{\partial t} = \frac{\hat{Q}^{n+1} - \hat{Q}^{n}}{\Delta t} \tag{2.48}$$

or the left hand side with BDF2 is

$$\frac{\partial \hat{Q}^{n+1}}{\partial t} = \frac{3\hat{Q}^{n+1} - 4\hat{Q}^{n} + \hat{Q}^{n-1}}{2\Delta t} \tag{2.49}$$

The right hand side of the equation can be linearized in time using Taylor series as

$$\begin{aligned} \hat{F}^{n+1} &= \hat{F}^{n} + \hat{A}\Delta\hat{Q} + O(\Delta t^2) \\ \hat{G}^{n+1} &= \hat{G}^{n} + \hat{B}\Delta\hat{Q} + O(\Delta t^2) \\ \hat{H}^{n+1} &= \hat{H}^{n} + \hat{A}\Delta\hat{Q} + O(\Delta t^2) \end{aligned} \tag{2.50}$$

where $\Delta\hat{Q} = \hat{Q}^{n+1} - \hat{Q}^{n}$ is the difference between the solutions at the new and old time steps, and A, B, C are flux Jacobians given as $\hat{A} = \frac{\partial \hat{F}}{\partial \hat{Q}}, \hat{B} = \frac{\partial \hat{G}}{\partial \hat{Q}}, \hat{C} = \frac{\partial \hat{H}}{\partial \hat{Q}}$. With these relations, the linearized form of the Eq. 2.47 can be written in the delta form

for BDF1 as:

$$\left[I + \Delta t(\partial_\xi \hat{A}^n + \partial_\eta \hat{B}^n + \partial_\zeta \hat{C}^n)\right] \Delta\hat{Q}^n = -\Delta t \left[\partial_\xi \hat{F}^n + \partial_\eta \hat{G}^n + \partial_\zeta \hat{H}^n - \hat{S}^n\right] \quad (2.51)$$

and similarly, for BDF2 as:

$$\begin{aligned} \left[I + \frac{2\Delta t}{3}(\partial_\xi \hat{A}^n + \partial_\eta \hat{B}^n + \partial_\zeta \hat{C}^n)\right] \Delta\hat{Q}^n = \\ -\frac{2\Delta t}{3}\left[\partial_\xi \hat{F}^n + \partial_\eta \hat{G}^n + \partial_\zeta \hat{H}^n - \hat{S}^n - \frac{\hat{Q}^n - \hat{Q}^{n-1}}{2\Delta t}\right] \end{aligned} \quad (2.52)$$

Finding $\Delta\hat{Q}^n$ requires the matrix inversion of the left hand side. However, the direct inversion of the left hand side of Eq. 2.51 or Eq. 2.52 is computationally too expensive. Therefore, further approximations are made to the left hand side using an approximate factorization method. The OVERTURNS flow solver employs either Lower-Upper Symmetric Gauss-Seidel (LUSGS) method [67] or Diagonalized Alternating Direction Implicit (DADI) [68] method for this purpose.

2.2.5 LUSGS

The LUSGS method factorizes the left hand side of the linearized governing equations into three groups: a lower diagonal (L), a main diagonal (D), and an

upper diagonal (U). Then, it approximates the left hand side as:

$$\begin{aligned}
[L+D+U]\Delta\hat{Q}^n &= D[D^{-1}L+I+D^{-1}U]\Delta\hat{Q}^n \\
&\approx D[I+D^{-1}L][I+D^{-1}U]\Delta\hat{Q}^n \\
&= [D+L]D^{-1}[D+U]\hat{Q}^n \\
&= -\Delta t[RHS]^n
\end{aligned} \tag{2.53}$$

where

$$\begin{aligned}
L &= \Delta t(-\hat{A}^+_{j-1,k,l} - \hat{B}^+_{j,k-1,l} - \hat{C}^+_{j,k,l-1}) \\
D &= I + \Delta t(\hat{A}^+_{j,k,l} - \hat{A}^-_{j,k,l} + \hat{B}^+_{j,k,l} - \hat{B}^-_{j,k,l} + \hat{C}^+_{j,k,l} - \hat{C}^-_{j,k,l}) \\
U &= \Delta t(\hat{A}^-_{j+1,k,l} + \hat{B}^-_{j,k+1,l} + \hat{C}^-_{j,k,l+1})
\end{aligned} \tag{2.54}$$

This can be solved using the forward and backward sweeps as:

$$\begin{aligned}
[D+L]\Delta\tilde{Q} &= -\Delta t[RHS]^n \\
[D+U]\Delta\hat{Q} &= D\Delta\tilde{Q}
\end{aligned} \tag{2.55}$$

Additional simplifications are made by using the spectral radius approximation of the flux Jacobians. For example, in the ξ direction, it is given as

$$\hat{A}^+ = \frac{1}{2}(\hat{A}+\sigma_\xi), \quad \hat{A}^- = \frac{1}{2}(\hat{A}-\sigma_\xi). \tag{2.56}$$

where σ_ξ is contributions from the both inviscid and viscous fluxes as

$$\sigma_\xi = |U_\xi| + c + \frac{2\mu(\xi_x^2 + \xi_y^2 + \xi_z^2)}{\rho} \tag{2.57}$$

where, U_ξ is the contravariant velocity in the ξ direction. By applying the approximation, the matrix inversion reduces to a scalar inversion.

2.2.6 DADI

The second method for the approximate factorization is DADI. In the DADI, the left hand side is approximated as

$$\begin{aligned} &\left[I + \Delta t(\partial_\xi \hat{A}^n + \partial_\eta \hat{B}^n + \partial_\zeta \hat{C}^n)\right] \Delta \hat{Q}^n \\ &\approx [I + \Delta t \partial_\xi \hat{A}][I + \Delta t \partial_\eta \hat{B}][I + \Delta t \partial_\zeta \hat{C}]\hat{Q}^n \end{aligned} \tag{2.58}$$

The inviscid flux Jacobians can be factored into eigenvectors and eigenvalues as

$$\lambda_\xi = T_\xi^{-1} \hat{A} T_\xi, \quad \lambda_\eta = T_\eta^{-1} \hat{B} T_\eta, \quad \lambda_\zeta = T_\zeta^{-1} \hat{C} T_\zeta \tag{2.59}$$

Assuming that changes of the eigenvectors is negligible in space, the approximated left hand side in Eq 2.58 can be re-written with factoring out of the eigenvalues as:

$$T_\xi[I + \Delta t \partial_\xi \lambda_\xi]T_\xi^{-1} T_\eta[I + \Delta t \partial_\eta \lambda_\eta]T_\eta^{-1} T_\zeta[I + \Delta t \partial_\zeta \lambda_\zeta]T_\zeta^{-1} = \Delta t RHS^n \tag{2.60}$$

The DADI algorithm approximates the block tridiagonal inversion to scalar tridiagonal inversion that can be solved using the Thomas algorithm. The eigenvalues and eigenvectors described above are only for inviscid fluxes. The effect of viscous fluxes can be included with the following eigenvalues:

$$\begin{aligned}
\lambda_v(\xi) &= \overline{\nu J^{-1}(\xi_x^2 + \xi_y^2 + \xi_z^2)}J \\
\lambda_v(\eta) &= \overline{\nu J^{-1}(\eta_x^2 + \eta_y^2 + \eta_z^2)}J \\
\lambda_v(\zeta) &= \overline{\nu J^{-1}(\zeta_x^2 + \zeta_y^2 + \zeta_z^2)}J
\end{aligned} \tag{2.61}$$

The final formulation with the both inviscid and viscous parts are as below:

$$\begin{aligned}
T_\xi[I + \Delta t(\partial_\xi \Lambda_\xi - \partial_{\xi\xi}\lambda_v(\xi))]T_\xi^{-1} T_\eta[I + \Delta t(\partial_\eta \Lambda_\eta - \partial_{\eta\eta}\lambda_v(\eta))]T_\eta^{-1} \\
T_\zeta[I + \Delta t(\partial_\zeta \Lambda_\zeta - \partial_{\zeta\zeta}\lambda_v(\zeta))]T_\zeta^{-1}\Delta\hat{Q}^n = -\Delta t[RHS^n]
\end{aligned} \tag{2.62}$$

where the first derivatives represent discretizations using upwinding, and the second derivatives are discretizations with the second order central differecing.

2.2.7 Dual-time stepping

The approximation of the left hand side saves computational costs but it results in factorization errors. To reduce the factorization errors, dual time-stepping is employed with a fictitious pseudo-time. The governing equations with a pseudo-time step, τ, are given as

$$\frac{\partial \hat{Q}}{\partial \tau} + \frac{\partial \hat{Q}}{\partial t} + \frac{\partial \hat{F}}{\partial \xi} + \frac{\partial \hat{G}}{\partial \eta} + \frac{\partial \hat{H}}{\partial \zeta} = \hat{S} \tag{2.63}$$

The BDF1 is the most common way to discretize the pseudo-time as below

$$\frac{\hat{Q}^{p+1}-\hat{Q}^{p}}{\Delta\tau}+\frac{\partial\hat{Q}^{p+1}}{\partial t}+\frac{\partial\hat{F}^{p+1}}{\partial\xi}+\frac{\partial\hat{G}^{p+1}}{\partial\eta}+\frac{\partial\hat{H}^{p+1}}{\partial\zeta}=\hat{S}^{p+1} \tag{2.64}$$

where p represents the solution at the pth sub-iteration and $\Delta\tau$ is a pseudo-time step size. For BDF1, $\partial\hat{Q}^{p+1}/\partial t$ is discretized as

$$\frac{\partial\hat{Q}^{p+1}}{\partial t}=\frac{\hat{Q}^{p+1}-\hat{Q}^{n}}{\Delta t} \tag{2.65}$$

Similarly, for BDF2,

$$\frac{\partial\hat{Q}^{p+1}}{\partial t}=\frac{3\hat{Q}^{p+1}-4\hat{Q}^{n}+\hat{Q}^{n-1}}{2\Delta t} \tag{2.66}$$

where n means the solutions at the physical time step. The remaining spatial operators are discretized using the same way shown in Eq. 2.47.

2.2.7.1 Derivation of a blended BDF scheme for dual-time stepping

In the present work, a blended formulation of the BDF2 and BDF1 is derived to investigate the effect of temporal damping on the rotor wake breakdown. Then, the formulation is coupled to dual-time stepping for unsteady rotor simulations.

First, the BDF1 is given as:

$$\frac{du}{dt}=\frac{u^{n+1}-u^{n}}{\Delta t} \tag{2.67}$$

The BDF2 is

$$\frac{du}{dt} = \frac{3u^{n+1} - 4u^n + u^{n-1}}{2\Delta t} = \frac{u^{n+1} - u^n}{\Delta t} + \frac{u^{n+1} - 2u^n + u^{n-1}}{2\Delta t} \tag{2.68}$$

From these, the BDF1 and BDF2 can be written in a blended form with a factor, ϵ, as

$$\frac{u^{n+1} - u^n}{\Delta t} + \frac{1-\epsilon}{2}\frac{u^{n+1} - 2u^n + u^{n-1}}{\Delta t} \quad \text{if} \quad \begin{matrix} \epsilon{=}0\text{: BDF2} \\ \epsilon{=}1\text{: BDF1} \end{matrix} \tag{2.69}$$

The BDF2 has more dominant dispersion errors than the dissipation errors. A physical meaning of ϵ is adding the temporal damping to the BDF2 scheme. A range of ϵ is from 0 to 1.

The blended formulation is applied to dual-time stepping, and the governing equation becomes

$$\frac{\hat{Q}^{p+1} - \hat{Q}^p}{\Delta\tau} + \frac{\hat{Q}^{p+1} - \hat{Q}^n}{\Delta t} + \frac{1-\epsilon}{2}\frac{\hat{Q}^{p+1} - 2\hat{Q}^n + \hat{Q}^{n-1}}{\Delta t} + R^{p+1} = 0 \tag{2.70}$$

where R contains all spatial operators shown in Eq. 2.64. Putting the equation into the delta form and linearizing one can write:

$$\frac{\Delta\hat{Q}^p}{\Delta\tau} + \frac{\Delta\hat{Q}^p + \hat{Q}^p - \hat{Q}^n}{\Delta t} + \frac{1-\epsilon}{2}\frac{\Delta\hat{Q}^p + \hat{Q}^p - 2\hat{Q}^n + \hat{Q}^{n-1}}{\Delta t} + \frac{\partial R^p}{\partial\hat{Q}}\Delta\hat{Q}^p = -R^p \tag{2.71}$$

Multiply by Δt and group together the $\Delta\hat{Q}^p$ terms on the LHS:

$$\begin{gathered}\left(\frac{\Delta t}{\Delta\tau}+1+\frac{1-\epsilon}{2}\right)\Delta\hat{Q}^p+\Delta t\frac{\partial R^p}{\partial\hat{Q}}\Delta\hat{Q}^p= \\ -\Delta t\left[\frac{\hat{Q}^p-\hat{Q}^n}{\Delta t}+\frac{1-\epsilon}{2}\frac{\hat{Q}^p-2\hat{Q}^n+\hat{Q}^{n-1}}{\Delta t}+R^p\right]\end{gathered} \tag{2.72}$$

Defining $h=\frac{\Delta t}{\frac{3-\epsilon}{2}+\frac{\Delta t}{\Delta\tau}}$ and rearranging:

$$\left[I+h\frac{\partial R^p}{\partial\hat{Q}}\right]\Delta\hat{Q}^p=-h\left[\frac{\hat{Q}^p-\hat{Q}^n}{\Delta t}+\frac{1-\epsilon}{2}\frac{\hat{Q}^p-2\hat{Q}^n+\hat{Q}^{n-1}}{\Delta t}+R^p\right] \tag{2.73}$$

where $\frac{\partial R^p}{\partial\hat{Q}}=(\partial_\xi\hat{A}^n+\partial_\eta\hat{B}^n+\partial_\zeta\hat{C}^n)$ and $R^p=(\partial_\xi\hat{F}^n+\partial_\eta\hat{G}^n+\partial_\zeta\hat{H}^n-\hat{S}^n)$.

The temporal damping of the blended BDF scheme is controlled with ϵ. For $\epsilon=1$, Eq. 2.73 becomes

$$\left[I+h\frac{\partial R^p}{\partial\hat{Q}}\right]\Delta\hat{Q}^p=-h\left[\frac{\hat{Q}^p-\hat{Q}^n}{\Delta t}+R^p\right],\quad h=\frac{\Delta t}{1+\frac{\Delta t}{\Delta\tau}} \tag{2.74}$$

which is dual time-stepping with BDF1.

Similarly, for $\epsilon=0$,

$$\left[I+h\frac{\partial R^p}{\partial\hat{Q}}\right]\Delta\hat{Q}^p=-h\left[\frac{3\hat{Q}^p-4\hat{Q}^n-\hat{Q}^{n-1}}{2\Delta t}+R^p\right],\quad h=\frac{\Delta t}{\frac{3}{2}+\frac{\Delta t}{\Delta\tau}} \tag{2.75}$$

which is dual time-stepping with BDF2.

The above equations have similar form as Eq. 2.51 or Eq. 2.52, so, they can be solved using the same approximate factorization method, either LUSGS or DADI. The right hand side of the equation is the unsteady residual that measures the

convergence of unsteady simulations. During the sub-iterations, it should decrease as the solutions converge.

2.2.8 Boundary Condition

This section discusses boundary conditions employed in the present work. Several boundary conditions are implemented in OVERTURNS flow solver. Among them, the following boundary conditions are used: wall, wake-cut, far-field, symmetric, periodic, and parallel boundary conditions.

2.2.8.1 Wall boundary

At the wall, the viscous wall condition (the no slip condition) is applied. For a stationery wall, velocity components at the wall are zero. For a moving wall, velocity components are set to the grid velocity. The density is extrapolated from the interior domain, and the pressure is calculated from the normal momentum equation.

2.2.8.2 Wake-cut boundary

In a C-type or O-type structured mesh, there are grid layers collapsing to a single line (2-D) or a plane (3-D), which is called the wake-cut. Figure 2.4 shows the wake-cut boundary from the trailing edge of the airfoil. The wake-cut boundary is located at the trailing edge of an airfoil (2-D or 3-D) or on the root and tip of the blade (3-D). The solutions should be continuous across the boundary, and, for

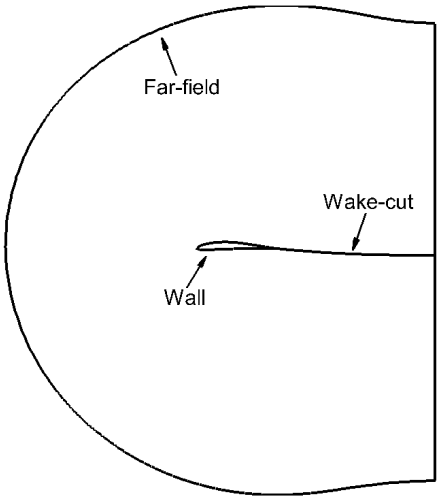

Figure 2.4: Boundary conditions of a C-type structured mesh.

this, the solutions from either side of the wake-cut are averaged at the wake-cut boundary.

2.2.8.3 Far-field boundary

In a simulation of external flow such as an airfoil, wing, or rotor blade, a computational mesh has a finite domain with artificial outer boundaries. The outer boundaries should not affect the solutions, and any characteristic waves should not reflect there. For this, the characteristic boundary conditions are applied at the far-field boundary. The boundary condition extrapolates flow variables using the Riemann invariants from the interior domain or the prescribed freestream values. In general, for 2-D airfoil cases, the outer boundaries located at 20∼30 chord lengths away from the wall are enough for the far-field boundary condition.

2.2.8.4 Symmetric boundary

For a symmetric domain to a plane, simulations can be performed only with a half domain using the symmetric boundary condition. In the symmetric boundary condition, the velocity normal to the plane and the fluxes across the boundary should be set to zero. In the present work, transition simulations of the 6:1 Prolate Spheroid are performed using the symmetric boundary condition with a computational mesh consisting of a half domain.

2.2.8.5 Periodic boundary

In a simulation of a hovering rotor, the flowfield can be assumed periodic in the azimuthal direction. For example, a four-bladed rotor has the periodicity of the flowfield every 90° in the azimuthal direction as shown in the Fig. 2.5. With this assumption, a hovering rotor simulation can be performed only with a quarter domain of the background and one blade instead of a full domain of the background and four blades. To employ the periodic boundary conditions, the background mesh should have additional "ghost layers" in the azimuthal direction for high-order reconstructions. In the "ghost layers", the solutions are extrapolated from the interior domain based on the periodicity of the flowfield.

2.2.8.6 Parallel boundary conditions

A 2-D airfoil simulation can be performed using a single CPU core, but 3-D wing or rotor simulations requires multiple CPU cores (approximately up to 1,000

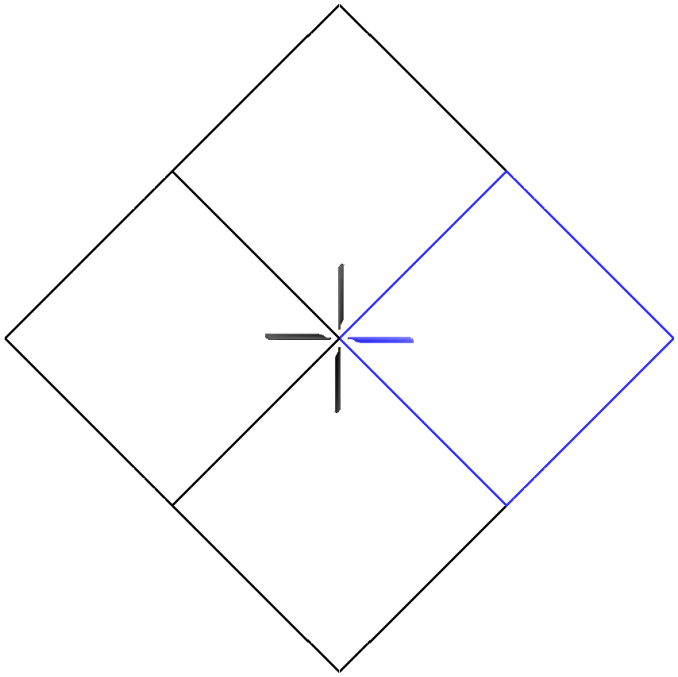

Figure 2.5: Periodicity in a hovering rotor simulation: four-bladed rotor

cores) with the parallelization. OVERTURNS flow solver is parallelized using the message passing interface (MPI) library. The computational domain is sub-divided in to multiple domains, and each domain communicates with adjacent domains through MPI library. In the parallel computation, OVERTURNS still maintains a high order of accuracy by employing the parallel boundaries that consisting of three "ghost layers". Figure 2.6 shows a schematic of the parallel boundaries. In the figure, black points represent the physical domains, and blue points show "ghost layers" for the parallel boundaries. The solutions at the parallel boundaries are transferred from the adjacent domains, and thus, simulations are performed without loss of order of accuracy in the sub-divided domains.

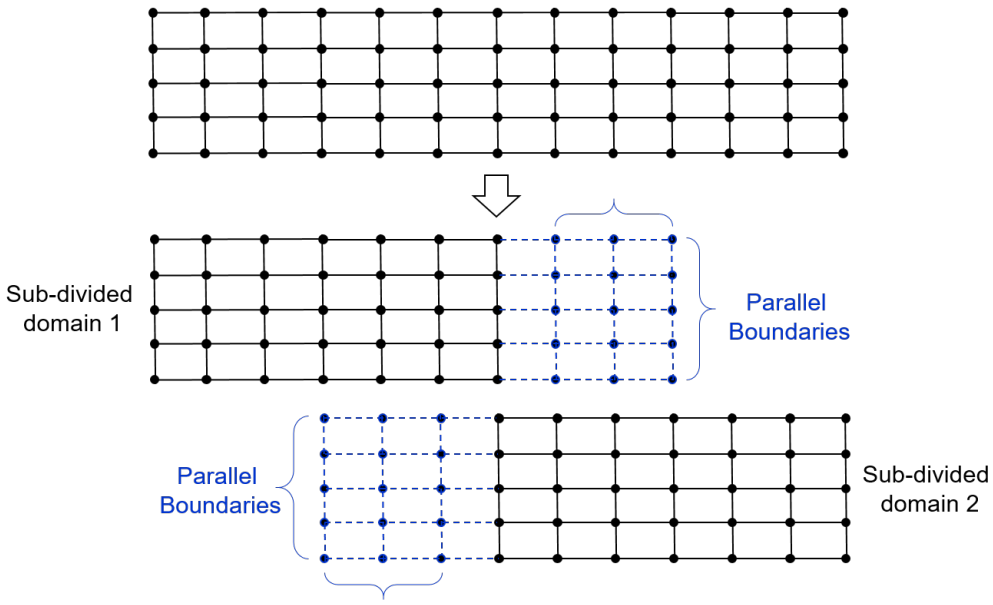

Figure 2.6: Schematic of the sub-division of the computational domain. Black: physical domain, Blue: parallel boundaries.

2.2.9 Overset Mesh Technique

Rotor simulations often require multiple meshes in the computational domain such as a blade mesh and background mesh or blade, fuselage, and background meshes. To transfer the solutions between the different meshes, OVERTURNS flow solver employs two overset mesh techniques: 1) an Implicit Hole Cutting (IHC) method developed by Lee [69] and further developed by Lakshminarayan [9] or 2) the open source Topology Independent Overset Grid Assembler (TIOGA) [70]. Each technique has different search algorithms, but they mainly consists of the following three steps: 1) identifying hole, fringe, and field points, 2) finding donor points and calculating interpolation weights, and 3) interpolating the data from the donor points to fringe points. Hole points represent points in one mesh that are within the solid wall of another mesh. In the hole points, the flow solutions are not calculated.

Fringe points are defined as points where the flow solutions are interpolated from the donor points of another mesh. Field points are regular points where the flow solutions are calculated. In general, fringe points are located at the outer boundaries of a mesh or in a region where another finer mesh is located. The information of the identified points are saved in an integer array called IBLANK with values of -1, 0, and 1 for hole, fringe, and field points, respectively. The IBLANK arrarys are coupled to the flow solver, and the flow solutions are updated only if IBLANK values are larger than zero.

For a general rotor simulation, the identification of the points should be done at every time step. However, in the present work, the identification is done only once at the beginning of the simulations because hovering rotor simulations are performed with the rotational source terms.

Chapter 3: Development of a Transition Model for the S–A Turbulence Model

This section discusses a Galilean invariant transition model for the S-A turbulence model. First of all, Menter's 1-eq γ transition model [47] is investigated as a baseline model, and modifications are made to integrate with the S–A turbulence model. Calibrations of the model constants are performed for more accurate predictions. Secondly, convergence of the transition model is improved with the application of the positivity of the implicit operator. Finally, the transition model is extended by coupling to two crossflow transition models.

3.1 Model Formulation

3.1.1 Transport equation for intermittency

Menter's 1-eq γ transition model solves a transport equation for intermittency (γ) . The transport equation for intermittency is defined as:

$$\frac{D(\rho\gamma)}{Dt} = P_\gamma - D_\gamma + \frac{\partial}{\partial x_j}\left[(\mu + \frac{\mu_t}{\sigma_\gamma})\frac{\partial\gamma}{\partial x_j}\right] \tag{3.1}$$

The production term, P_γ, is given as:

$$P_\gamma = F_{length}\rho S\gamma(1-\gamma)F_{onset} \tag{3.2}$$

where S is the strain rate magnitude. The destruction term, D_γ, is defined as:

$$D_\gamma = C_{a2}\rho\Omega\gamma F_{turb}(C_{e2}\gamma - 1) \tag{3.3}$$

where Ω is the vorticity magnitude. Transition onset criteria are defined as:

$$F_{onset1} = \frac{Re_v}{2.2Re_{\theta c}}, \quad F_{onset2} = (F_{onset1}, 2.0) \tag{3.4}$$

$$F_{onset3} = \max\left(1 - \left(\frac{R_T}{3.5}\right)^3, 0\right), \quad F_{onset} = \max(F_{onset2} - F_{onset3}, 0) \tag{3.5}$$

$$F_{turb} = e^{-\left(\frac{R_T}{2}\right)^4}, \quad R_T = \frac{\mu_t}{\mu}, \quad Re_v = \frac{\rho d_w^2 S}{\mu}, \quad Re_{\theta c} = f(Tu_L, \lambda_{\theta L}) \tag{3.6}$$

where d_w is the wall distance. R_T of the original model is calculated with k and ω from the SST turbulence model, but they are not available in the S–A turbulence model. So, in this study, they are replaced with a ratio of the turbulent eddy viscosity to laminar eddy viscosity.

The model constants are:

$$F_{length} = 100, \quad c_{e2} = 50, \quad c_{a2} = 0.06, \quad \sigma_\gamma = 1.0 \tag{3.7}$$

3.1.2 Local formulations for Tu, $\lambda_{\theta L}$, and $Re_{\theta c}$

The original transition model calculates the local turbulence intensity with k and ω as below:

$$Tu_L = \min\left(100\frac{\sqrt{2k/3}}{\omega d_w}, 100\right) \tag{3.8}$$

As mentioned earlier, k and ω are not available in the S–A turbulence model. To circumvent this issue, Nichols [42] replaced them with $\omega = S/0.3$ and $\mu_t = \rho k/\omega$. However, as Nichols states, with these modifications, there is no way to account for experimental freestream turbulence intensity in the transition model. Moreover, the initial condition of the S–A turbulence model ($\tilde{\nu}$) should be adjusted to match the experimental data. To overcome these limitations, the present work employs a constant turbulence intensity in the entire computational domain. An input turbulence intensity is a measured value from the experiment. The assumption of the constant turbulence intensity is valid for external aerodynamic flow [47] and has been already extensively validated in the work by Medida [32] and Jung and Baeder [71].

The pressure gradient variable of the model is given:

$$\begin{aligned} \lambda_{\theta L} &= -7.57 \times 10^3 \frac{dV}{dy}\frac{d_w^2}{\nu} + 0.0128 \\ \lambda_{\theta L} &= \min(\max(\lambda_{\theta L}, -1.0), 1.0) \end{aligned} \tag{3.9}$$

The critical Reynolds number is defined as:

$$Re_{\theta c} = C_{TU1} + C_{TU2} \exp[-C_{TU3} Tu_L F_{PG}(\lambda_{\theta L})] \tag{3.10}$$

The original coefficients are:

$$C_{TU1} = 100.0, \quad C_{TU2} = 1000.0, \quad C_{TU3} = 1.0 \tag{3.11}$$

Colonia et al. [72] suggested a new set of the constants based on 2-D airfoil simulations as:

$$C_{TU1} = 163.0, \quad C_{TU2} = 1002.25, \quad C_{TU3} = 1.0, \tag{3.12}$$

Because Colonia et al. performed calibrations of the model constants with 2-D airfoil cases at low turbulence intensity, however, the new set of the constants does not work well at high turbulence intensity. Therefore, the current work employs linear blending of the model constants based on simulation results of flow over the zero-pressure gradient flat plate. The constants by Colonia et al. [72] are applied for the turbulence intensity below Tu=0.51%, whereas the original model constants are used for the turbulence intensity above Tu=2.0%. Between the turbulence intensity

of 0.51% and 2.0%, two sets of model constants are linearly blended as below:

$$\begin{aligned} Tu &= \min(\max(Tu, 0.51), 2.0) \\ C_{TU1} &= (100.0 - 163.0)/(2.0 - 0.51) \times (Tu - 2.0) + 100.0 \\ C_{TU2} &= (1000.0 - 1002.25)/(2.0 - 0.51) \times (Tu - 2.0) + 1000.0 \\ C_{TU3} &= 1.0 \end{aligned} \tag{3.13}$$

F_{PG} function is given:

$$F_{PG}(\lambda_{\theta L}) = \begin{cases} \min(1 + C_{PG1}\lambda_{\theta L}, C_{PG1}^{lim})) \quad , \quad \lambda_{\theta L} \geq 0 \\ \min(1 + C_{PG2}\lambda_{\theta L} + C_{PG3}\min[\lambda_{\theta L} + 0.0681, 0], C_{PG2}^{lim}), \quad \lambda_{\theta L} < 0 \end{cases} \tag{3.14}$$

Constants of F_{PG} are as below:

$$C_{PG1} = 14.68, \quad C_{PG2} = -7.34, \quad C_{PG3} = 0.0, \quad C_{PG1}^{lim} = 1.5, \quad C_{PG2}^{lim} = 3.0 \tag{3.15}$$

Finally, a limit of F_{PG} is applied as to guarantee non-negative values:

$$F_{PG} = \max(F_{PG}, 0) \tag{3.16}$$

3.1.3 Coupling with S–A turbulence model

For the original transition model, the output intermittency is coupled to the transport equation for the k of the $k-\omega$ SST turbulence model. On the other hand, in the present work, the output intermittency is applied to the source terms of the

S–A turbulence model as Nichols did [42]:

$$\frac{D\tilde{\nu}}{Dt} = \gamma_s P_{\tilde{\nu}} - \max(\gamma_s, 0.1) D_{\tilde{\nu}} + \frac{1}{\sigma}\left[\nabla \cdot ((\nu + \tilde{\nu})\nabla\tilde{\nu}) + c_{b2}(\nabla\tilde{\nu})^2\right] \tag{3.17}$$

where $P_{\tilde{\nu}}$ and $D_{\tilde{\nu}}$ are the production and destruction terms of the S–A turbulence model, respectively. In the original transition model, the minimum value of intermittency at the wall in the laminar boundary layer is not zero but 0.02 ($=1/c_{e2}$). However, Nichols proposed the scaling of the intermittency so that it goes to zero in the laminar boundary layer. During the implementation, it was checked that scaling intermittency gives more accurate results for the S–A turbulence model. Therefore, the current work employs the scaling of intermittency as

$$\gamma_s = \frac{\min(\gamma, 1) - 1/c_{e2}}{1 - 1/c_{e2}}, \quad \gamma_s = \max(\min(\gamma_s, 1), 0) \tag{3.18}$$

The original transition model has an additional production term P_k^{lim} in the turbulent kinetic transport equation to make transition prediction more robust at arbitrary low turbulence intensities and/or in the separation bubbles.

$$P_k^{lim} = 5C_k max(\gamma - 0.2, 0)(1 - \gamma) F_{on}^{lim} max(3C_{sep}\mu - \mu_t, 0) S\Omega \tag{3.19}$$

Nichols applied this term with modifications for the production of the S–A turbulence model as

$$P_{\tilde{\nu}}^{lim} = 5C_k max(\gamma - 0.2, 0)(1 - \gamma) F_{on}^{lim} max(3C_{sep}\mu - \mu_t, 0)\sqrt{S\Omega} \tag{3.20}$$

However, the additional production term is not employed in the current work, since significant effects of the term were not found in simulations with the S–A turbulence model.

3.2 Application of the positivity in the implicit operator for implicit methods

During tests of the transition model, it was found that the transition model shows convergence issues in some cases due to non-physical negative intermittency values. The negative intermittency values are corrected to zero by Eq. 3.18 but caused convergence stall as shown in Fig. 3.1(a). To improve the convergence, the positivity of the implicit operator is enforced using a similar way proposed by Spalart and Allmaras [29]. The positivity is applied to the source, diffusion, and convection terms of the transition model. Because the positivity for the diffusion and convection terms are very similar to those of the S–A turbulence model, however, the positivity for the source terms are only shown here. The original production and destruction of the transition model are

$$P_\gamma = F_{length}\rho S\gamma(1-\gamma)F_{onset}, \quad D_\gamma = C_{a2}\rho\Omega\gamma F_{turb}(C_{e2}\gamma - 1) \tag{3.21}$$

This can be written in the form given by Spalart and Allmaras [29] as

$$P = F_{length}\rho S(1-\gamma)F_{onset}, \quad P' = -F_{length}\rho S F_{onset} \tag{3.22}$$

$$D = C_{a2}\rho\Omega F_{turb}(C_{e2}\gamma - 1)D, \quad D' = C_{a2}\rho\Omega F_{turb}C_{e2} \tag{3.23}$$

They are combined together for Jacobians

$$\overline{D} - \overline{P} = \text{pos}[D - P] + \text{pos}[D' - P']\gamma \quad \text{where} \quad \text{pos}(x) = \begin{cases} x & \text{if} \quad x \geq 0 \\ 0 & \text{if} \quad x < 0 \end{cases} \tag{3.24}$$

Figure 3.1 compares convergences of intermittency for NLF(1)-0416 airfoil at $\alpha = 12°$. The residual without the positivity shows convergence stalls, whereas the residual with the positivity of the implicit operator shows significantly improved convergences.

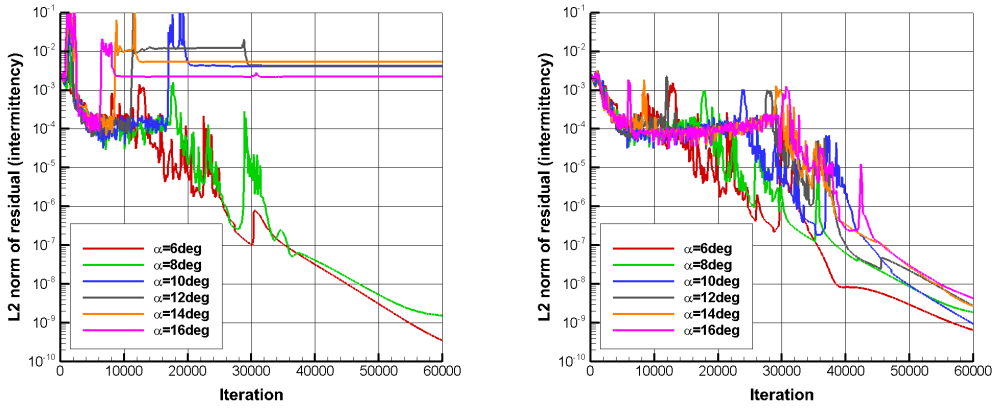

(a) Without the positivity (b) With the positivity

Figure 3.1: Convergence of intermittency without and with the positivity of the implicit operator.

3.3 Extension of the model for prediction of crossflow transition

The original transition model is only available for streamwise transition such as natural transition, bypass transition, and separation induced transition. To include

the effect of 3-D crossflow transition, the transition model is coupled to two crossflow transition models proposed by Menter and Smirnov [33] and Langtry et al. [37]. Menter and Smirnov's model uses the wall normal change of the normalized vorticity vector to measure the local crossflow strength, and thus, the model is Galilean invariant. On the other hand, Langtry et al.'s model employs the helicity as an indicator of the crossflow strength, so it is not Galilean invariant. However, Langtry et al.'s model accounts for the effects of surface roughness on the crossflow transition, whereas Menter and Smirnov's model does not. Because Galilean invariance is not an issue for a stationary object, Langtry et al.'s model is still useful for stationary objects such as a fuselage.

Menter and Smirnov's model is derived from the Arnals C1 correlation. The crossflow transition onest criterion is given

$$T_{C1local} = \frac{C_{RSF}}{150}(G\Psi Re_v) > 1 \tag{3.25}$$

where the G accounts for the pressure gradient (shape factor), Ψ indicates the strength of crossflow, and Re_v includes the effects of Reynolds number. The correlation constant C_{RSF} is given as 1.0, but it is set to 1.35 with the S–A turbulence model based on calibration results. The function G is calculated as:

$$g(\lambda_{\theta L,CF}) = 27864.0\lambda^3_{\theta L,CF} - 1962.0\lambda^2_{\theta L,CF} + 54.3\lambda_{\theta L,CF} + 1.0 \tag{3.26}$$

$$g(\lambda_{\theta L,CF}) = min\left[max\left(g(\lambda_{\theta L,CF}), 1.0\right), 2.3\right] \tag{3.27}$$

$$G(\lambda_{\theta L,CF}) = 0.684/g(\lambda_{\theta L,CF}) \tag{3.28}$$

where the $\lambda_{\theta L,CF}$ is a variable for the local pressure gradient and calculated as

$$\lambda_{\theta L,CF} = -7.57 \times 10^{-3} \frac{dV}{dy} \frac{d_w^2}{\nu} + 0.0174 \tag{3.29}$$

$$\lambda_{\theta L,CF} = min[max(\lambda_{\theta L,CF}, 0), 0.0477] \tag{3.30}$$

The indicator of crossflow strength, Ψ, is calculated based on the wall normal change of the normalized vorticity as follow

$$\Psi = \left|\vec{\phi}\right| d_w, \qquad \vec{\phi} = \vec{n} \cdot \bigtriangledown \vec{e}_\omega, \qquad \vec{e}_\omega = \frac{\vec{\omega}}{|\vec{\omega}|} \tag{3.31}$$

where $\vec{e}_\omega$ is the vorticity vector and $\vec{n}$ is the wall normal vector. Re_v is from the baseline transition model. Finally, the crossflow transition onset criterion is integrated with the baseline transition model as:

$$F_{onset,CF} = min(max(100(T_{C1local} - 1), 0), 1) \tag{3.32}$$

$$F_{onset} = max(F_{onset}, F_{onset,CF}) \tag{3.33}$$

Langtry et al.'s crossflow transition model is given

$$Re_{scf} = \frac{\rho \left(\frac{U}{0.82}\right) \theta_t}{\mu} = -35.088ln\left(\frac{h}{\theta_t}\right) + 319.51 + f(+\Delta H_{crossflow}) - f(-\Delta H_{crossflow}) \tag{3.34}$$

where h is a root mean square (RMS) value of surface roughness height. Because the momentum thickness, θ_t is on both left and right hand sides of the equation, it should be solved using an iterative method such as the shooting method or Newton method. The crossflow strength is calculated using the non-dimensionalized crossflow strength $H_{crossflow}$ with the streamwise vorticity $\Omega_{streamwise}$ (helicity) as

$$H_{crossflow} = \frac{y\Omega_{streamwise}}{U}, \quad \Omega_{streamwise} = \left|\vec{U} \cdot \vec{\Omega}\right| \tag{3.35}$$

$$\vec{U} = \left(\frac{u}{\sqrt{u^2+v^2+w^2}}, \frac{v}{\sqrt{u^2+v^2+w^2}}, \frac{w}{\sqrt{u^2+v^2+w^2}}\right) \tag{3.36}$$

where y is the wall normal distance and $\vec{\Omega}$ is the vorticity vector. Remaining parts of the right hand side of the Eq. 3.34 are calculated as

$$\Delta H_{crossflow} = H_{crossflow}\left(1.0 + min\left[R_T, 0.4\right]\right) \tag{3.37}$$

$$+\Delta H_{crossflow} = max(0.1066 - \Delta H_{crossflow}, 0.0) \tag{3.38}$$

$$f(+\Delta H_{crossflow}) = 6200(+\Delta H_{crossflow}) + 50000(+\Delta H_{crossflow})^2 \tag{3.39}$$

$$-\Delta H_{crossflow} = max(-(0.1066 - \Delta H_{crossflow}), 0.0) \tag{3.40}$$

$$f(-\Delta H_{crossflow}) = 75tanh\left(\frac{-\Delta H_{crossflow}}{0.0125}\right) \tag{3.41}$$

In the original model, the output Re_{scf} is applied to the transport equation for $\tilde{Re}_{\theta t}$. However, in the 1-eq γ transition model, the transport equation is not available. To integrate Langtry et al.'s model with the current transition model, a new transition

onset criterion is added in the baseline transition model as

$$F_{onset1} = max\left[\frac{Re_v}{2.2Re_{\theta c}}, \frac{cRe_v}{2.2Re_{scf}}\right] \tag{3.42}$$

where c is a calibration constant and set to 0.98 in the present work. A similar approach was applied in Carnes and Coder [35] to couple the Langtry et al.'s model with the AFT2019b transition model.

Chapter 4: Validation of the SA-γ transition model

SA-γ transition model is validated against various 2 dimensional and 3 dimensional cases such as flow over zero pressure gradient flat plate, airfoils, prolate spheroid, and a hovering rotor. All transition simulations use $\tilde{\nu}/\nu = 0.1$ as an initial conditions of the S–A turbulence model based on the recommendation by Spalart and Allmaras [29]. Comparisons are made with available experimental data and fully turbulent simulation results.

4.1 2-D zero-pressure gradient flat plate

SA-γ transition model is tested for flow over the zero-pressure gradient flat plate. Simulations are performed for the Schubauer-Klebanoff (S-K) case [73] and T3 cases [74]. Table 4.1 shows freestream turbulence intensity of the each case. A computational mesh is from NASA Turbulence Modeling Resource (TMR) website [75], and the grid consists of 273 and 193 points in the streamwise and the wall normal directions. The same boundary conditions and inflow conditions (M=0.2, Re_L=5M) are applied as the conditions given for the fully turbulent simulation.

Figure 4.1 compares skin friction on the flat plate between the current predictions and the experimental data. For the S-K case that has the lowest freestream

turbulence intensity, the SA-γ model predicts slightly delayed transition than the experiment. For the T3 cases, predicted transition locations are in good correlations with the experimental data. For the T3B case, the current result shows slightly lower skin friction than the experiment after the transition onset. However, this is also observed in other transition simulations using the S-A turbulence model.

S-K [73]	T3A- [74]	T3A [74]	T3B [74]
0.03%	0.51%	2.0%	5.25%

Table 4.1: Turbulence intensity of zero pressure gradient flat plate cases

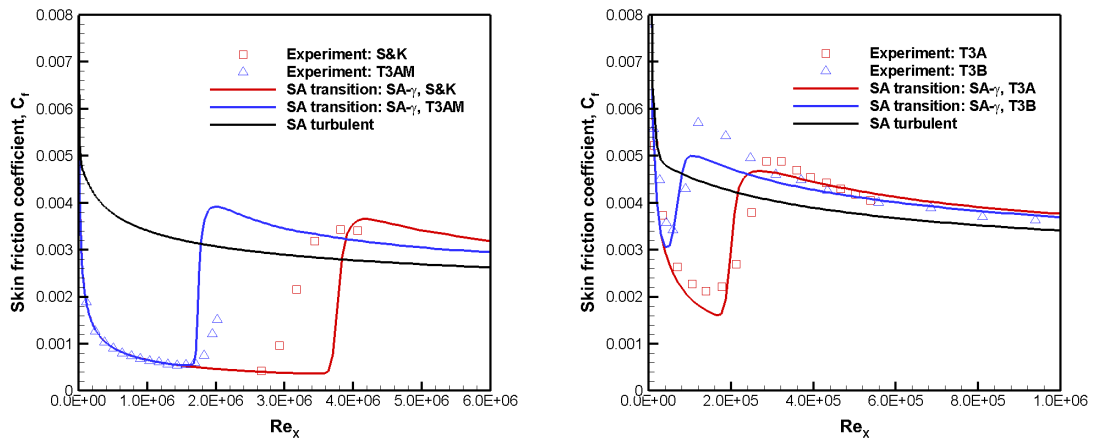

(a) S-K, T3A-

(b) T3A, T3B

Figure 4.1: Comparison of skin frictions on the zero-pressure gradient flat plate.

4.2 2-D airfoil cases

SA-γ transition model is validated against four 2-D airfoil cases. Table 4.2 summarizes flow conditions of the cases. All cases are subsonic, and Reynolds number ranges from 2×10^5 to 4×10^6. Comparisons are made with fully turbulent simulation results and available experimental data, such as skin friction, surface pressure,

lift, drag, and transition locations.

Figure 4.2 shows computational grids of the cases, C-type structured grids. The grids of the Aerospatiale-A and Eppler 387 airfoils are generated using an in-house C-type structured mesh generator, whereas S809 and NLF(1)-0416 airfoil grids are the "Medium" grids provided by 2018 AIAA CFD Transition Modeling Discussion Group [76]. A number of grid points in the wrap around and wall normal direction is 705 and 97, respectively, and 513 points are located on the airfoil surface. The wall normal spacing (y^+) of the grids is less than 1. The far-field boundaries of the Aerospatiale-A and E387 grids are located at 40 chord lengths away from the surface, whereas the S809 and NLF(1)-0416 grids have the far-field boundaries at 1000 chord lengths away from the surface. The meshes generated by the in-house grid generator has a smaller outer-boundaries, but it is still enough for the far-field boundary conditions to avoid unphysical reflections of the waves.

Airfoil	Mach	Re [$\times 10^6$]	Tu [%]	AoA [°]
Aerospatiale-A [77]	0.15	2.1	0.1	13.3
S809 [78]	0.1	2.0	0.05	multiple
NLF(1)-0416 [79]	0.1	4.0	0.15	multiple
E387 [80]	0.1	0.2	0.1	multiple

Table 4.2: Flow conditions of 2-D airfoil cases.

4.2.1 Aerospatiale-A Airfoil

The Aerospatial-A airfoil was tested in ONERA F-1 wind tunnel in 1997 [77]. The experimental results at the angle of attack of 13.3° have been widely used as a validation case for transition simulations [15, 32, 71]. Figure 4.3 shows comparisons of skin friction and pressure coefficients on the airfoil surface. In the experiment,

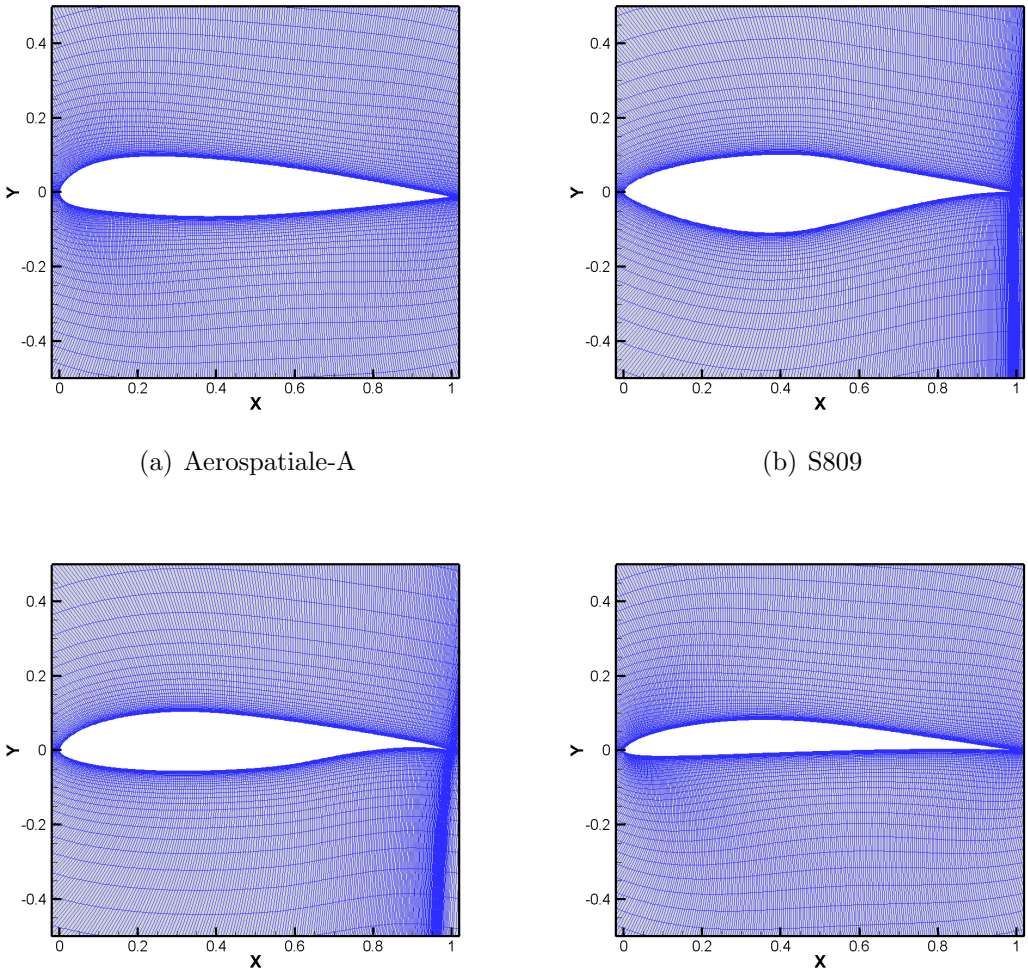

(a) Aerospatiale-A

(b) S809

(c) NLF(1)-0416

(d) Eppler 387

Figure 4.2: 2-D airfoil grids (C-type structured mesh).

a laminar separation bubble exists on the suction side (upper surface) of the airfoil around 12% of the chord, and separation-induced transition results in a development of the turbulent boundary layer downstream. In Fig. 4.3(a), SA-γ model captures a decrease of skin friction due to the laminar-separation bubble and a rapid increase after the separation-induced transition. On the other hand, baseline SA turbulence model doesn't predict this trend at all. In Fig. 4.3(b), comparisons of surface pressure distribution are shown. SA-γ result shows a slightly higher suction peak than

the experiment and the fully turbulent simulation result, but overall agreement with the experiment is very good on both suction and pressure sides. Drag coefficients from the experiment, SA-γ model, and baseline SA turbulence model, are 0.0208, 0.0182, and 0.0273, respectively. The transition model under-predicts the drag coefficient by 12.5%, but it gives a better agreement with the experiment than the fully turbulent simulation result that over-predicts the drag coefficient by 31.25%.

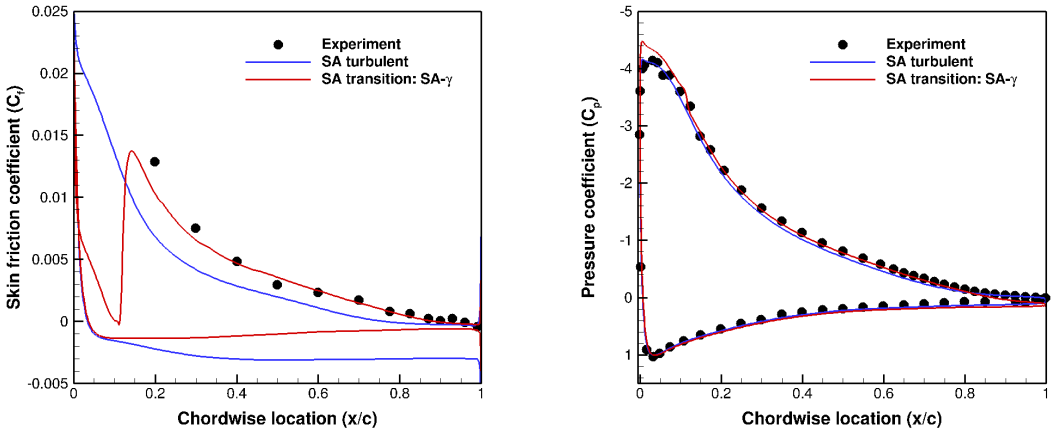

(a) Skin friction coefficient

(b) Pressure coefficient

Figure 4.3: Comparison of skin friction and pressure distributions.

4.2.2 S809, Wind-Turbine Airfoil

The S809 is a laminar-flow airfoil designed for wind turbine applications. The airfoil was tested in the low-turbulence wind tunnel of the Delft University of Technology, Netherlands in 1986 [78]. Predicted lift and drag polar are plotted in Fig. 4.4 against the experimental data. For the lift coefficient in Fig. 4.4(a), SA-γ model slightly over-predicts the lift coefficient at low angles of attack, whereas the baseline SA turbulence model under-predicts the lift coefficient. However, overall agreement

in the linear range of the lift curve is reasonable. On the other hand, at angles of attack higher than 10°, both fully turbulent and transition simulations over-predict lift coefficients due to a known limitation of the SA turbulence model under the adverse pressure gradient. For the drag polar in Fig. 4.4(b), SA-γ model significantly improves the prediction of the drag bucket at low angles of attack by including the effects of laminar flow over airfoil surfaces. Figure 4.5 shows comparisons of surface

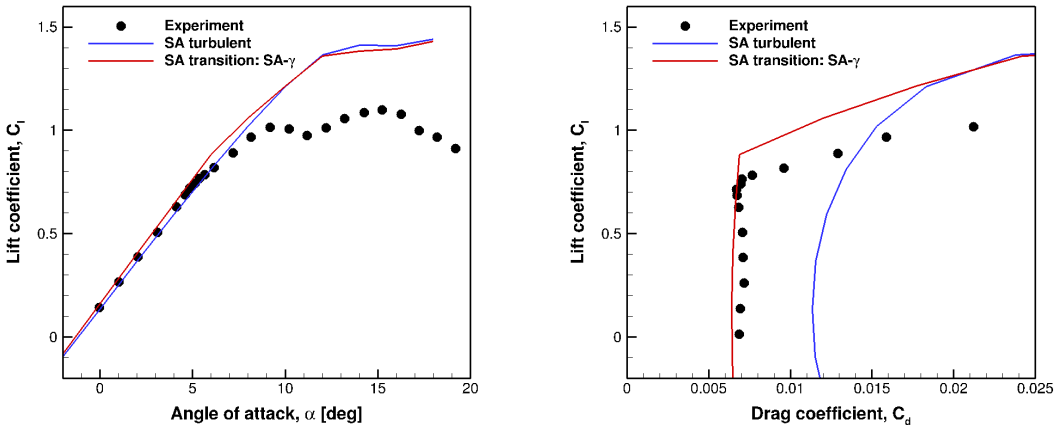

(a) AoA Vs. Lift coefficient (b) Drag Polar

Figure 4.4: Comparison of lift and drag polar between CFD and the experiment for S809 airfoil.

pressure coefficients between CFD predictions and the experiment at four angles of attack. At angles of attack 1° and 5°, SA-γ results are in better correlations with the experiment than the fully-turbulent results and successfully captures laminar-separation bubbles on the airfoil. At angles of attack 9° and 14°, there are no important differences between SA-γ and fully-turbulent results. At angle of attack 9°, both results show a good comparison with the experiment, but at angle of attack 14°, both SA-γ and fully turbulent simulations over-predict pressure distributions

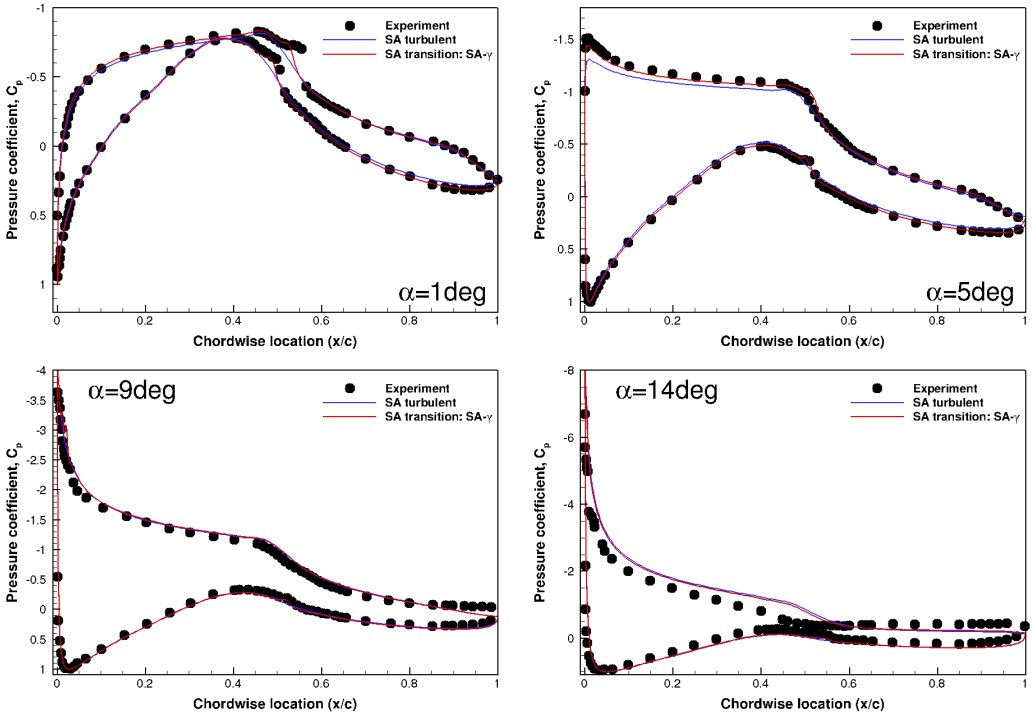

Figure 4.5: Comparison of surface pressure coefficients between CFD and the experiment for S809 airfoil.

on the upper surface.

Finally, a grid study is performed with the meshes "Tiny" to "Ultra", provided by 2018 AIAA CFD Transition Modeling Discussion Group [76]. Table 4.3 shows the number of grid points from the Tiny to Ultra mesh. The grid study is particularly important because some CFD results such as OVERFLOW with Langtry–Menter's transition model [81] show spurious oscillations on the surface pressure distributions with a very fine mesh ("Ultra mesh"). Figure 4.6 shows results of the grid study for the pressure, skin friction, and lift and drag coefficients at two angles of attack, $\alpha = 1^\circ$ and $\alpha = 6^\circ$. For the pressure coefficient (Fig. 4.6(a) and 4.6(b)), the Tiny mesh (coarsest mesh) gives oscillations near the separation bubble on the upper surface, but it disappears as the mesh becomes finer. Figures 4.6(c) and 4.6(d)

shows the skin friction coefficient for the different meshes. As it was observed in the pressure coefficient, the tiny mesh results are slightly off from the other results, but all meshes give relatively similar trends. As the mesh becomes finer, the peaks in the skin friction coefficient due to the separation bubble become more sharp on the both upper and lower surfaces. Finally, Figs 4.6(e) and 4.6(f) show convergences of the lift and drag coefficients with respect to a number of grid points on the airfoil surface. At $\alpha = 1°$, the lift coefficient shows a converged trend from the medium mesh. On the other hand, for the drag coefficient, a slope of change decreases as the mesh becomes finer, but it is still converging with the finest mesh. At $\alpha = 6°$, the lift and drag coefficients change significantly between the Tiny to the Coarse mesh, and then they converge very rapidly. Overall, SA-γ model gives robust results for all meshes and show good comparisons with the experimental data. Suspicious oscillations shown in OVERFLOW results [81] for S809 airfoil with the "Ultra" mesh are not observed in the current results.

Mesh	JMAX	KMAX	Points on the wall
Tiny	353	49	257
Coarse	529	73	385
Medum	705	97	513
Fine	1057	145	769
Extra	1409	193	1025
Ultra	2113	289	1537

Table 4.3: Number of grid points for grid study.

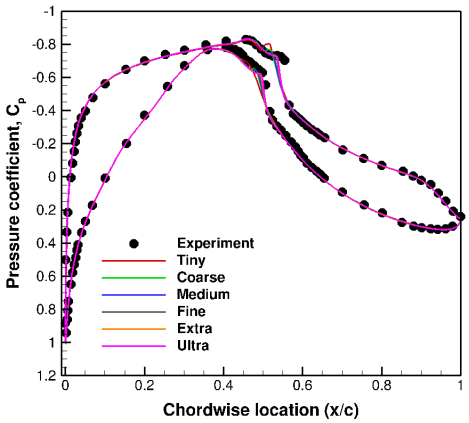

(a) Pressure coefficient at $\alpha = 1°$

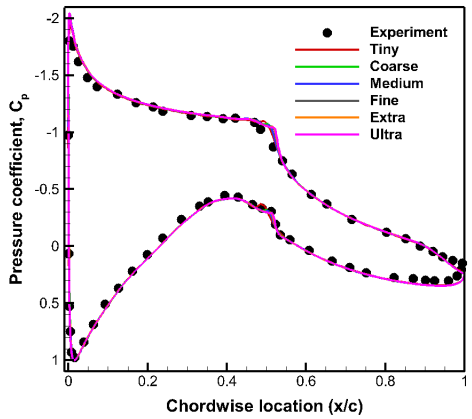

(b) Pressure coefficient at $\alpha = 6°$

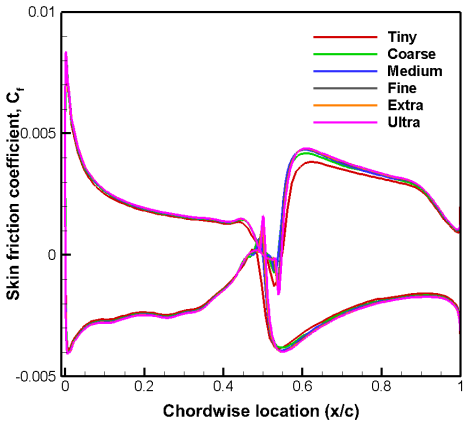

(c) Skin friction coefficient at $\alpha = 1°$

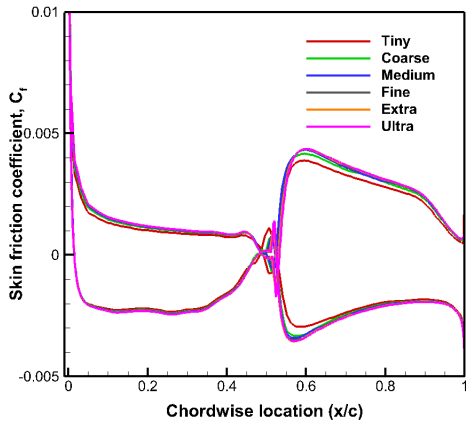

(d) Skin friction coefficient at $\alpha = 6°$

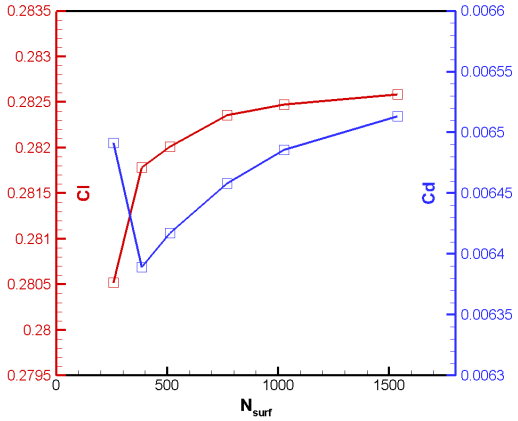

(e) Convergence of Cl and Cd at $\alpha = 1°$

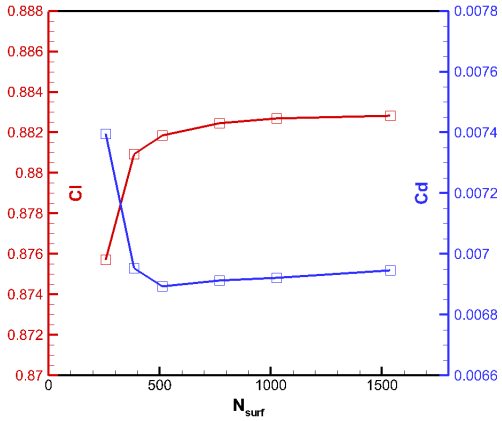

(f) Convergence of Cl and Cd at $\alpha = 6°$

Figure 4.6: Grid study results for the S809 airfoil.

4.2.3 NLF(1)-0416, General-Aviation Airfoil

NLF(1)-0416 is a "Natural-Laminar-Flow" airfoil for general aviation applications. The airfoil was designed to obtain high maximum lift with the low-drag characteristics. The experiment was performed in the Low-Turbulence Pressure Tunnel (LTPT) at the NASA Langley Research center [79].

Figure 4.7 shows comparisons of lift coefficient and drag polar. In the lift coefficient in Fig. 4.7(a), SA-γ and fully turbulent simulations show very similar results. They compare well with the experiment in the linear range of the lift curve but over-predict the lift coefficients after the stall angle of attack. For drag polar in Fig. 4.7(b), SA-γ results shows much better comparison with the experiment than the fully turbulent simulation results.

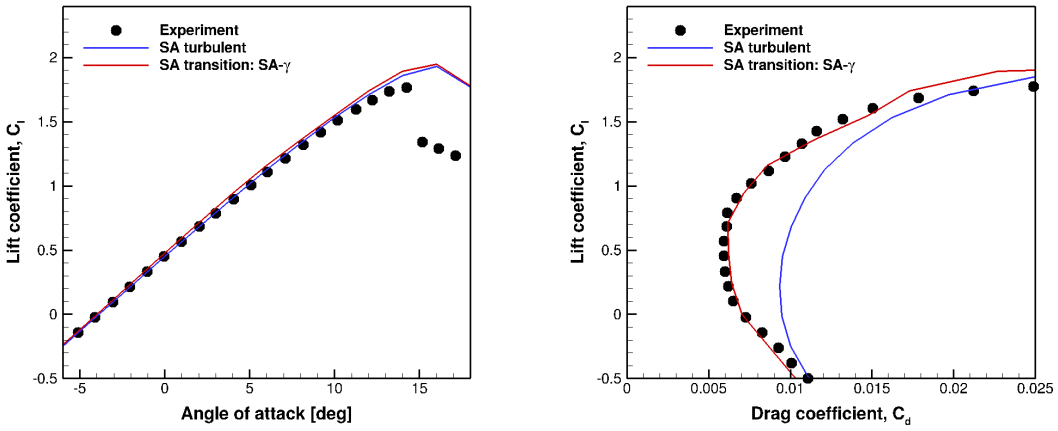

(a) AoA Vs. Lift coefficient (b) Drag Polar

Figure 4.7: Comparison of lift and drag polar between CFD and the experiment for NLF(1)-0416 airfoil.

Predicted surface pressure distributions are compared against the experiment in Fig. 4.8. At α=0°, SA-γ result shows a better comparison on the upper surface

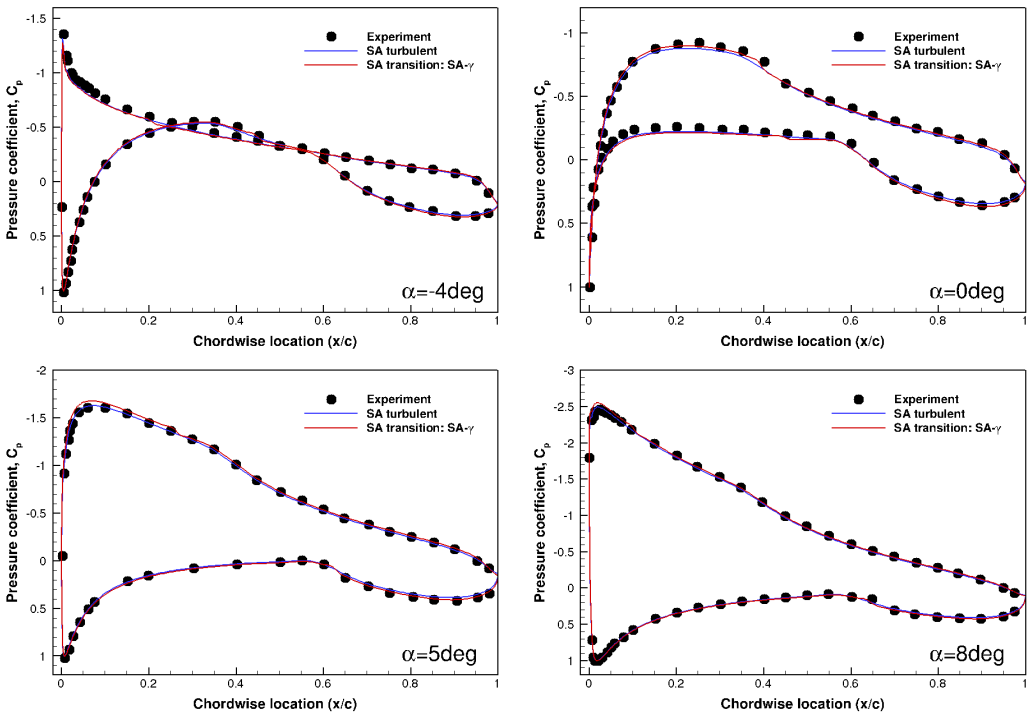

Figure 4.8: Comparison of surface pressure coefficients between CFD and the experiment for NLF(1)-0416 airfoil.

at $x < 0.4c$, but overall results from SA-γ and fully-turbulent simulations are very similar at all angles of attack.

As it was performed for the S809 airfoil, a similar grid study is performed for the NLF(1)-416 airfoil using the six different meshes from "Tiny" to "Ultra" mesh, provided by 2018 AIAA CFD Transition Modeling Discussion Group. A number of grid points for the each grid is given in Table 4.3. Figure 4.9 shows results of the grid study for the pressure, skin friction, and lift and drag coefficients at $\alpha = 0°$ and $\alpha = 5°$. In OVERFLOW results using Langtry–Menter's transition model [81], unphysical oscillations of the pressure distributions were observed with the Ultra mesh for NLF(1)-0416 airfoil too, but the current SA-γ model gives reliable results from the Tine to Ultra meshes with good comparisons with the experimental data in

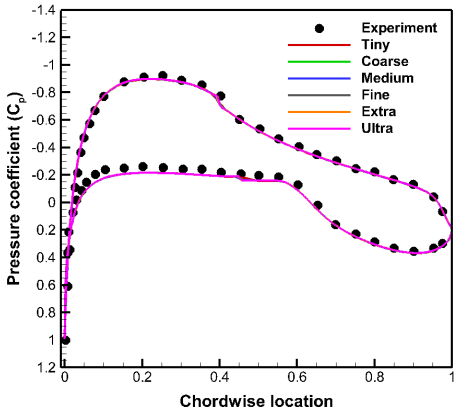

(a) Pressure coefficient at $\alpha = 0°$

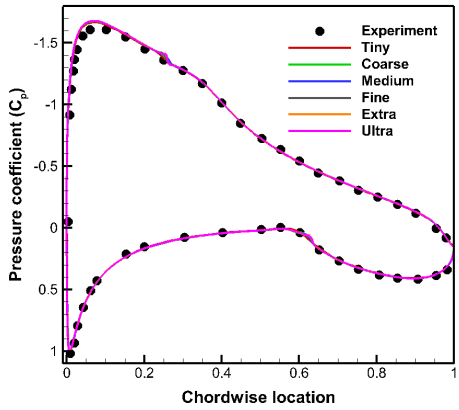

(b) Pressure coefficient at $\alpha = 5°$

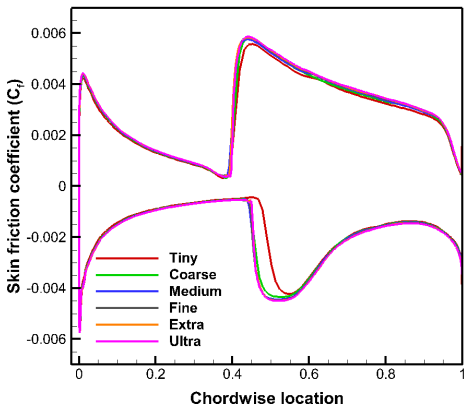

(c) Skin friction coefficient at $\alpha = 0°$

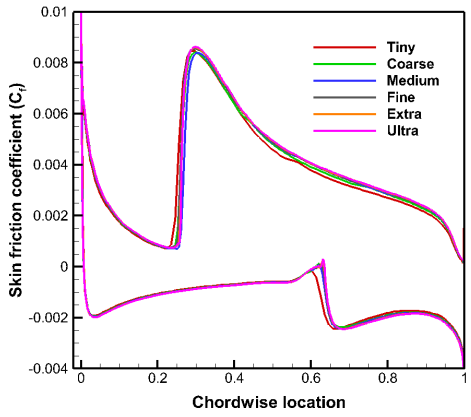

(d) Skin friction coefficient at $\alpha = 5°$

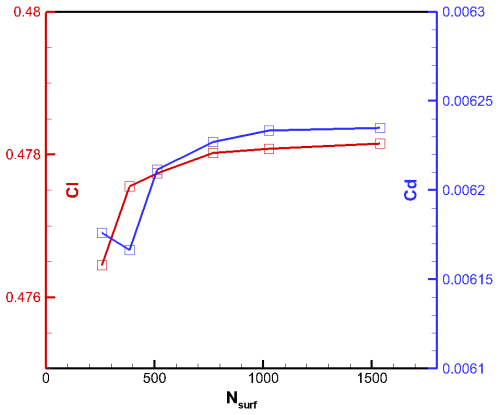

(e) Convergence of Cl and Cd at $\alpha = 0°$

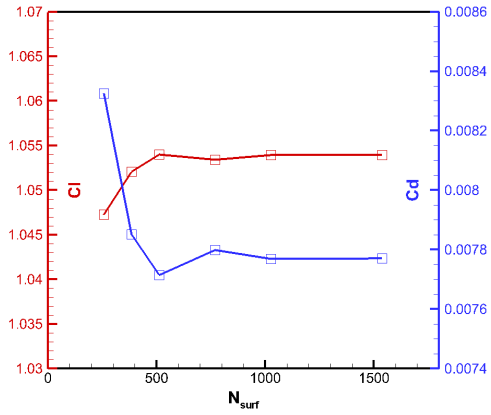

(f) Convergence of Cl and Cd at $\alpha = 5°$

Figure 4.9: Grid study results for the NLF(1)-0416 airfoil.

Figs. 4.9(a) and 4.9(b). For the skin friction coefficient, all mesh shows similar trends of the skin friction distribution except the tiny mesh that shows delayed transition at $\alpha = 0°$ and earlier transition at $\alpha = 5°$. For the lift and drag coefficients in Figs. 4.9(e) and 4.9(f), they both converge well as a number of grid points on the airfoil surface increases.

4.2.4 E387, Low Reynolds Number Airfoil

Eppler E387 airfoil is a low Reynolds number airfoil designed for model sailplanes. The airfoil has been widely tested at various low Renolds number wind tunnels, and the experimental data in this work are obtained from UIUC low-speed subsonic wind tunnel in 2002 [80].

Predicted lift and drag polar are plotted against the experimental data in Fig. 4.10. For the lift coefficient in Fig. 4.10(a), the SA-γ and the baseline turbulence model give very similar results at the linear range of the lift curve. However, after the stall angle of attack, the baseline SA turbulence model over-predicts the lift coefficient, whereas the transition model captures decrease of the lift coefficient well. For the drag polar in Fig. 4.10(b), the turbulence simulation inaccurately predicts the drag through the entire range. In contrast, SA-γ model results compare very well with the experiment. Figure 4.11 shows a comparison of the drag breakdown between the fully turbulent and transition simulations. In the fully turbulent results, the viscous drag is larger than the pressure drag at low angles of attack and it mainly accounts for the total drag at angles of attack lower than 7°. On the other hand,

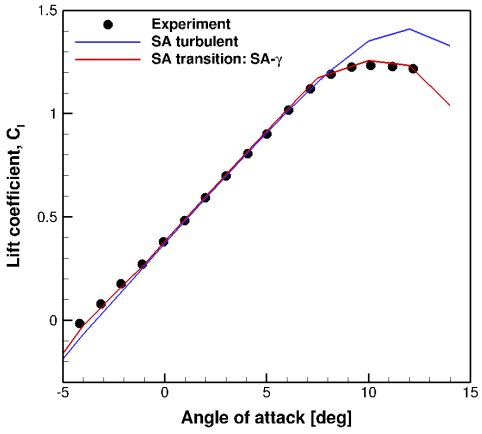

(a) AoA Vs. Lift coefficient

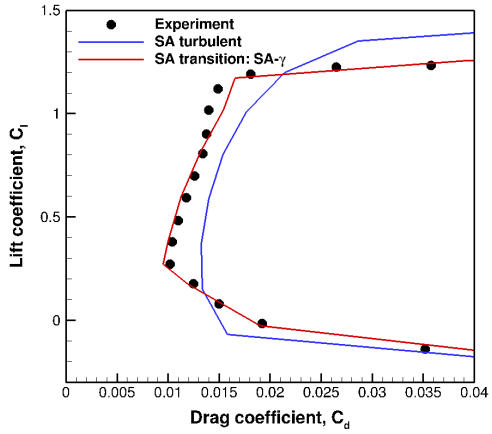

(b) Drag Polar

Figure 4.10: Comparison of lift and drag polar between CFD and the experiment for E387 airfoil.

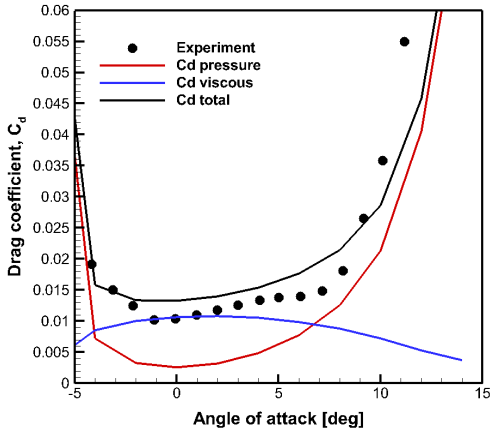

(a) SA turbulent

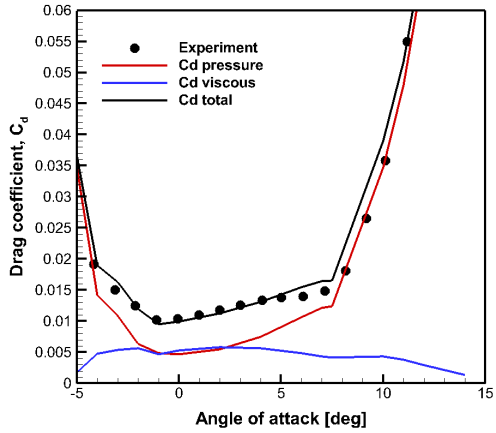

(b) SA transition: SA-γ

Figure 4.11: Comparison of drag component breakdown between the SA and SA-γ results.

in the transition simulation results, the pressure drag is a major source of the total drag, and it is larger than the pressure drag through the entire range of the angles of attack.

Figure 4.12 compares predicted surface pressure distributions against the experimental data at four angles of attack. In all results, SA-γ model captures the

effect of the laminar-separation bubble on the upper surface of the airfoil well, whereas the turbulent simulations do not at all. The higher pressure drag predicted from the transition simulations shown in Fig. 4.11(b) is due to the separation bubble on the upper surface of the airfoil.

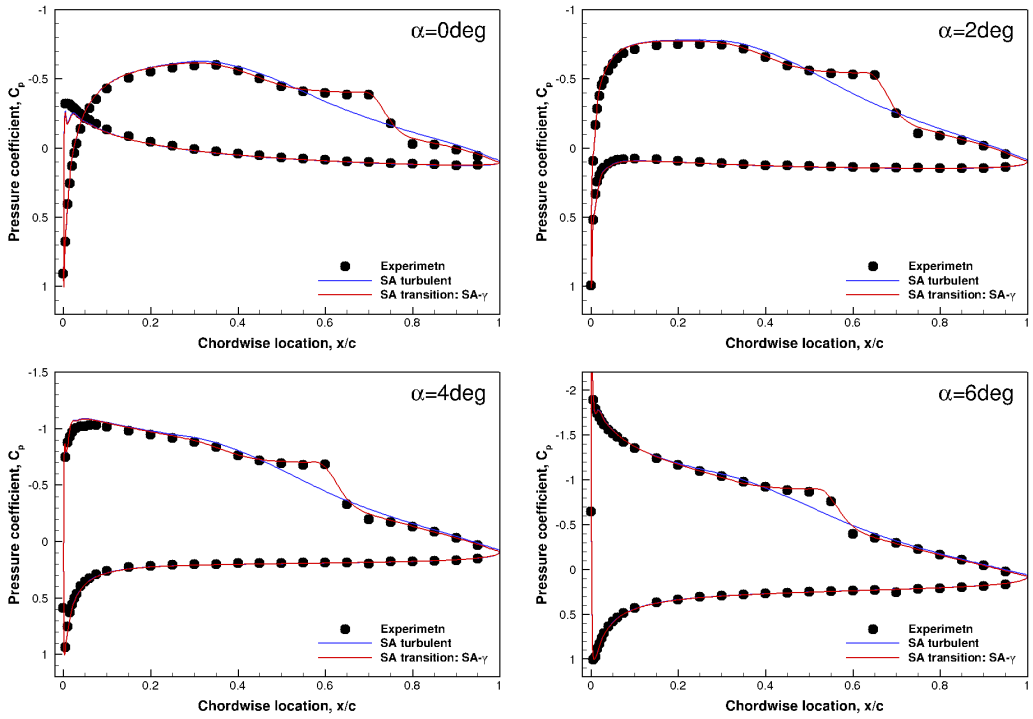

Figure 4.12: Comparison of surface pressure coefficients between CFD and the experiment for E387 airfoil.

Figure 4.13 shows predicted skin friction distributions on the upper surface of the airfoil and locations of the laminar separation and turbulent reattachment. In Fig. 4.13(a), locations of the laminar separation are points where the skin friction becomes negative, and locations of the turbulent reattachment are points where the skin friction becomes positive again. In Fig. 4.13(b), predicted locations of the laminar separation and turbulent reattachment are compared against the measured locations in the experiment. In the experiment, the laminar separation bubble

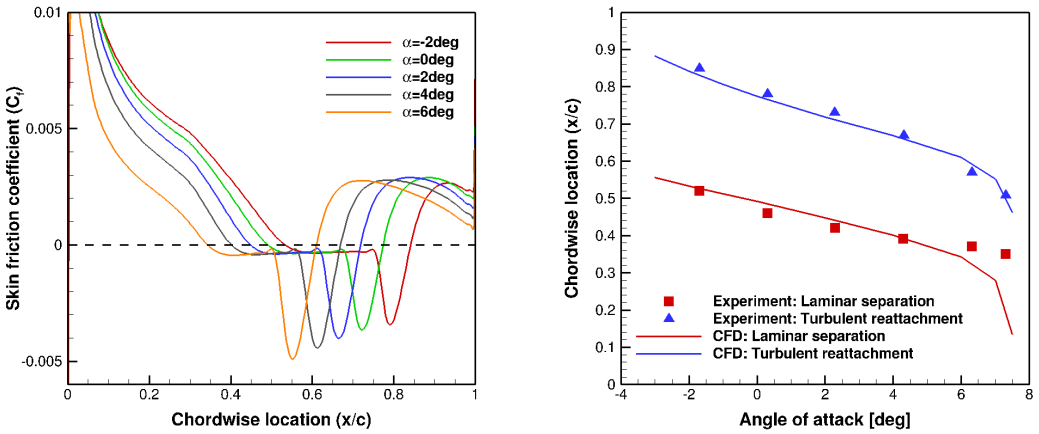

(a) Predicted skin friction on the upper surface (b) Locations of laminar separation and turbulent reattachment

Figure 4.13: Comparison of transition locations on the upper surface of E387 airfoil.

extends to more than 30% of the chord at low angles of attack, and it becomes smaller and moves forward as the angle of attack increases. In the figure, it is seen that the SA-γ model captures locations of the laminar separation and turbulent reattachment very well except at the high angles of attack where the laminar separation bubble becomes smaller and the type of transition changes from the separation-induced transition to the natural transition. Overall, SA-γ model gives reliable predictions at the low Reynolds number as well.

4.3 3-D cases

SA-γ model is applied to 3-D cases such as an infinite swept wing, prolate spheroid, and a hovering rotor. The effect of crossflow transition is investigated using two different crossflow transition models by Langtry et al. and Menter and Smirnov. All simulations use $\tilde{\nu}/\nu = 0.1$ as the initial conditions of the S–A turbulence model like the previous 2-D cases. For a hovering rotor, simulations are performed in the time-accurate manner. Detailed flow conditions of the cases are given in each section.

4.3.1 NLF(2)-0415 swept wing

The NLF(2)-0415 swept wing was tested in the Arizona State University Unsteady Wind Tunnel by Dagenhart et al. [2] and Radeztsky et al. [82]. A Reynolds number sweep was performed at a constant angle of attack of -4° with a swept angle of 45° to investigate crossflow instability on a swept wing. Before a comparison is made between CFD predictions and the experiment, the experimental data should be mentioned. Figure 4.14 shows the experimental data by Dagenhart et al. [2] and Radeztsky et al. [82]. Radeztsky et al.'s data accounts for the effect of surface roughness on the transition locations, and Langtry et al.'s crossflow transition model was calibrated using them. On the other hand, Dagenhart et al.'s data do not include the effect of the surface roughness but flow conditions of the experiments are clearly clarified. Many crossflow transition models are developed using Dagenhart et al.'s data. An issue is that there are some consistent shift of Reynolds number

between Dagenhart et al.'s data and Radeztsky et al.'s data for $h = 3.3\mu m$. It's not clear which data are correct, but Venkatachari et al. [83] assumes Dagenhart et al.'s data are correct for $h = 3.3\mu m$ because Dagenhart et al.'s paper [2] includes more clear information about flow conditions. For this reason, Venkatachari et al. used Dagenhart et al's data for $h = 3.3\mu m$ and Radeztsky et al.'s data for $h = 0.5\mu m$ and $h = 0.25\mu m$ to validate their OVERFLOW simulations. The current work also follows this assumption for calibrations of the model and comparisons with the experiment.

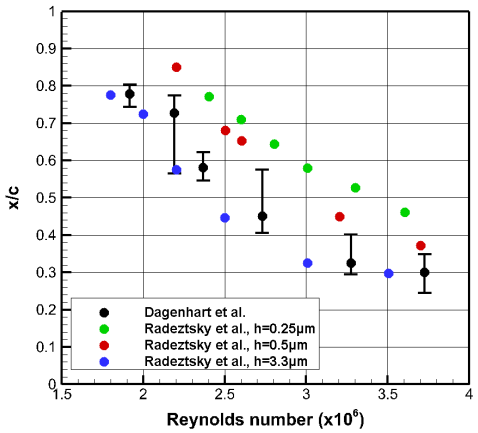

Figure 4.14: Comparison of experimental data of NLF2-0415.

Simulations are performed for the experimental conditions of $Re = 1.92\times10^6 \sim 3.73\times10^6$, Tu=0.09%, $\alpha = -4°$, and $\beta = 45°$. A C-type structured grid is generated using an in-house mesh generator, and the grid consists of 705 points in the wrap around direction (513 points on the surface), 97 points in the wall normal direction, and 7 points in the spanwise direction. Initial wall normal spacing of the grid is 3.5e-6 chords, and the far-field boundaries are located at 20 chords from the surface. Figure 4.15(a) shows predicted transition locations with and without crossflow tran-

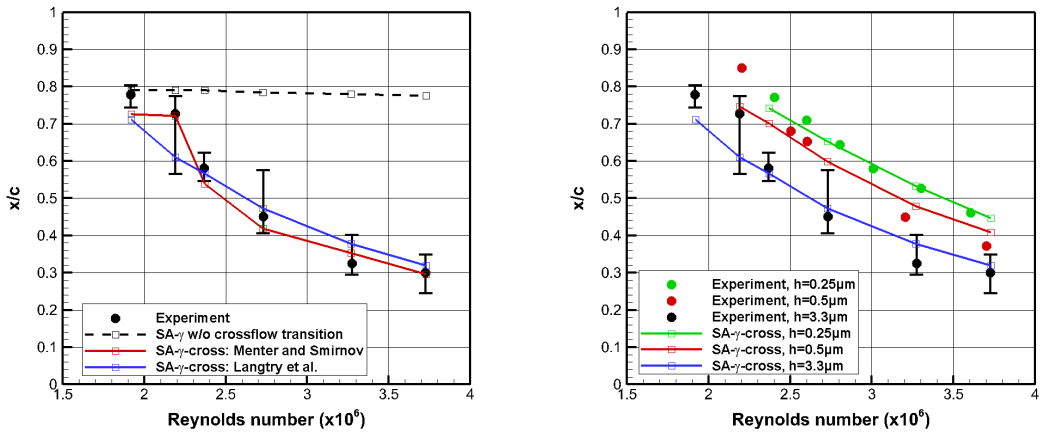

(a) Comparison of transition location with crossflow transition models.

(b) Effect of surface roughness with Langtry et al. model.

Figure 4.15: Prediction of transition locations with crossflow transition models.

sition models against the Dagenhart et al.'s data [2]. For Langtry et al.'s model, $3.3\mu m$ is used for the surface roughness height. In the figure, the baseline transition model is unable to predict locations of crossflow transition correctly. On the contrary, the two crossflow transition models improve the prediction of transition locations significantly. Both transition models show earlier transition at Re=1.92×10^6 but the agreement becomes better as the Reynolds number increases.

The crossflow transition model by Langtry et al. accounts for surface roughness. In Fig. 4.15(b), the predicted transition locations for different surface roughness heights are compared against the experimental data. In the results, the effect of surface roughness on crossflow transition are well captured with Langtry et al.'s crossflow transition model.

4.3.2 Inclined 6:1 Prolate Spheroid

SA-γ model is applied to the inclined 6:1 Prolate Spheroid [84]. The Prolate Spheroid was tested in DFVLR low speed wind tunnel at Gottingen, Germany, and dominating transition modes, Tollmien–Schlichting and/or crossflow, are investigated as functions of Reynolds numbers and angles of attack [84]. Figure 4.16 shows a computational mesh near the spheroid surface. The grid is "Medium grid" provided by the AIAA CFD Transition Modeling Discussion group and consists of 193 points in the streamwise direction, 97 points in the spanwise direction, and 97 points in the wall normal direction. The grid only includes a half domain, and thus, it requires the symmetric boundary condition at the xz plane. Table 4.4 shows flow conditions of simulations. Computations are performed at three angles of attack, and results are compared against the measured transition locations on the spheroid surface.

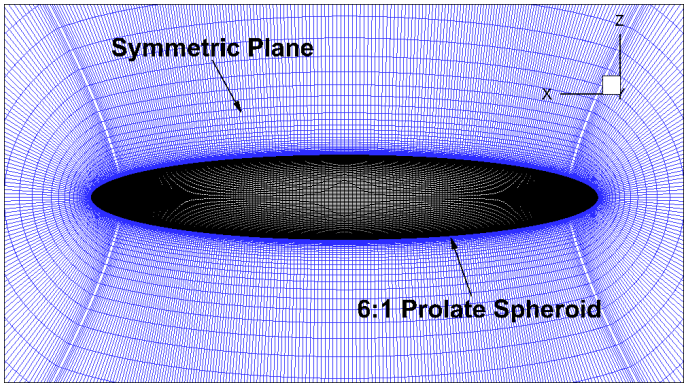

Figure 4.16: Surface and volume grid of the 6:1 Prolate Spheroid.

Mach	Re [$\times 10^6$]	Tu [%]	AoA[°]
0.13	6.5	0.15	5, 10, 15

Table 4.4: Flow conditions of the inclined 6:1 prolate spheroid.

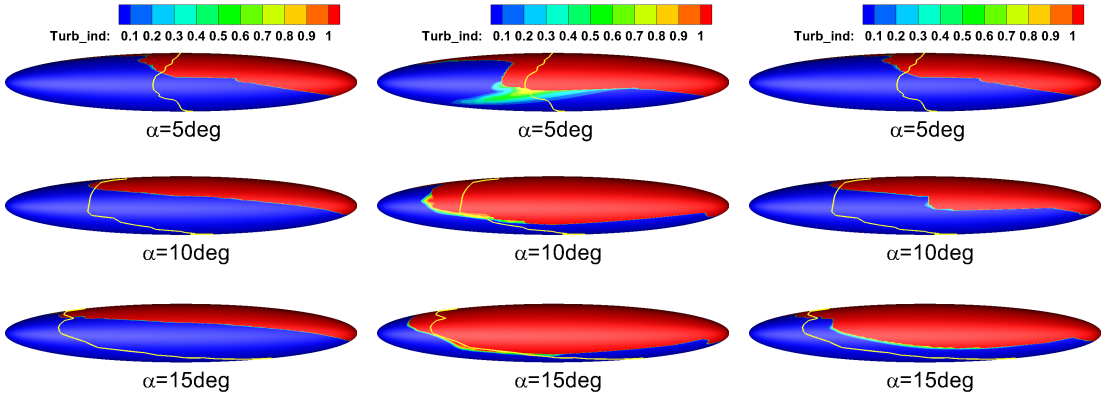

(a) Baseline $SA-\gamma$ (b) $SA-\gamma$-cross: Menter and Smirnov. (c) $SA-\gamma$-cross: Langtry et al..

Figure 4.17: Predicted turbulence index against the measured transition locations of the 6:1 Prolate Spheroid.

Figure 4.17 shows contours of predicted turbulence index [29] on the spheroid surface. In the figure, red area represents turbulent flow, whereas blue area means laminar flow. For a comparison with the experiment, measured transition locations are also plotted in the figure as yellow lines. At $\alpha = 5°$, both Tollmien-Schlichting and crossflow instabilities are dominant in the experiment. However, in CFD results, the $SA-\gamma$ model and crossflow transition model by Langtry et al. only predict Tollmien–Schlichting instability. Menter and Smirnov's model gives larger turbulent area than the two results, but it still captures less effects of the crossflow transition. As the angle of attack increases, the results from crossflow transition models show better agreement with the experiment than those from the baseline transition model. At $\alpha = 10°$, Menter and Smirnov's model gives the best agreement with the experiment, but Langtry et al.'s model also predicts larger turbulent area than the baseline transition model. At $\alpha = 15°$, both crossflow transition models show reasonable agreements with the experiment. The two crossflow transition models show

different trends with respect to the angle of attack, but, in general, they improve comparisons with the experiment as the angle of attack increases.

4.3.3 NASA Langley's PSP hovering rotor

Finally, the transition model is applied to NASA Langleys PSP hovering rotor [10]. The rotor was tested at NASA Langley Research Centers Rotor Test Cell (RTC) in 2016. In the experiment, the hover performance of the installed rotor was investigated with a ROBIN Mod-7 fuselage underneath for various transition conditions, and boundary layer transition locations on the blade surfaces were measured using the infrared thermography technique.

4.3.3.1 Computational mesh system

Figure 4.18 shows a computational mesh system consisting of a single O-O type blade mesh and 1/4 domain Cartesian background mesh with periodic boundary conditions. The blade mesh has 291 x 204 x 78 points in the wrap around, spanwise, and normal directions, respectively with the wall normal spacing (y+) of 0.4. The background mesh is a quarter domain Cartesian background mesh and contains 174 x 174 x 164 points in radial and vertical directions. A mesh adaptation is performed on the background mesh based on the tip vortex trajectory. A minimum cell size of the original background mesh is 0.12C, whereas a size of the adapted mesh is 0.06C in the refined region. Top, bottom, and radial boundaries are located at 4.2R, 8.1R, and 6.0R respectively. The original experiment includes the ROBIN Mod-7 fuselage

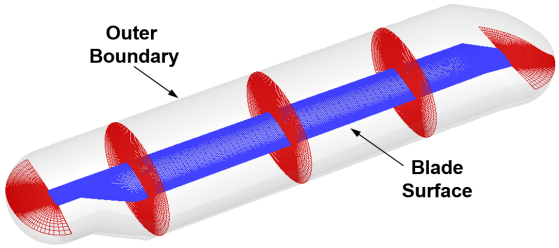

(a) Single O-O type blade mesh.

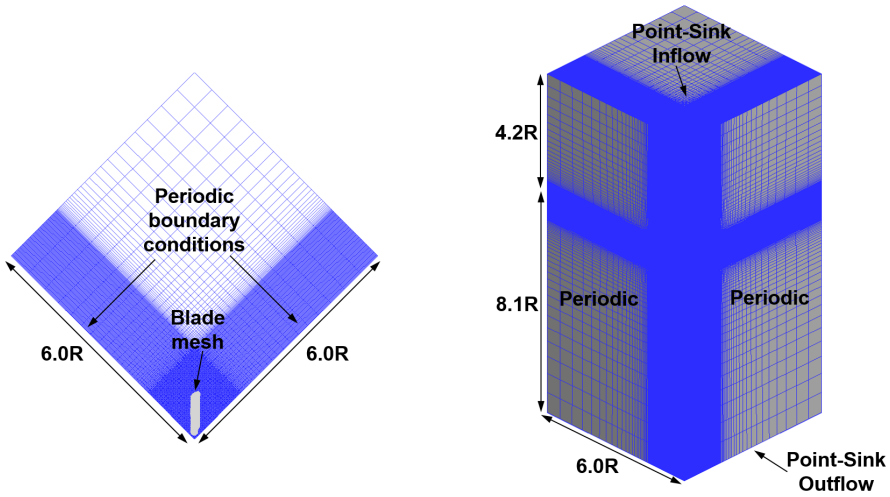

(b) Upper and side view of the background mesh.

Figure 4.18: Total mesh system: O-O type blade mesh and 1/4 Cartesian background mesh.

beneath the rotor, but it's not included in the current simulations.

4.3.3.2 Simulation setup

Simulations are performed from low to high thrust levels for six collective pitch angles from 6° to 11°. In order to remove artifact effects of CFD simulations such as starting vortices, calculations were performed in two phases. The first 12 rotor revolutions were computed with the third-order MUSCL scheme, BDF1, and only 2 sub-iterations in fully-turbulent simulations. In the second phase, the solution was

restarted and run for 10 more revolutions with the fifth-order WENO scheme, the blended BDF ($\epsilon = 0.1$), and 10 sub-iterations in SA-γ transition simulations. In both phases, a time step size of 0.25° was maintained with a constant CFL number of 10 for a pseudo-time step during the sub-iterations.

For transition simulations, the freestream turbulence intensity is a key parameter of transition simulations. However, the experimental value is not available because it was not measured. In the current work, a constant freestream turbulence intensity of 0.075% ($\approx N_{crit} = 9$) is applied in the computational domain. Then, other values are tested at low and high thrust levels based on the simulations results. For the simulations using Langtry et al.'s crossflow transition model, a RMS roughness height of $0.5\mu m$ was applied, which is equivalent to a RMS roughness height of a polished surface. However, the experimental measurement of the RMS roughness height is not available.

4.3.3.3 Result: fully-turbulent simulations

To validate the baseline computational setup, fully turbulent simulations are performed first. Figure 4.19 shows predicted Figure of Merit plotted against the experimental data and other CFD results using the SST turbulence model by Jain [5]. As mentioned earlier, the current work doesn't include the fuselage. The data from Jain's work [5] are also for the "isolated rotor" without the fuselage. In the fully turbulent simulations, the current predictions compare well with the experimental data with the fixed upper surface at the low and medium collective pitch angles. On

the other hand, at the high collective pitch angles, a better comparison is observed with the experimental data where the both surfaces are fixed. Compared to the other CFD results by Jain [5], the trends of the predicted Figure of Merit are very similar although the present study and Jain's work [5] use different computational setups in terms of flow solvers, computational meshes, and turbulence models.

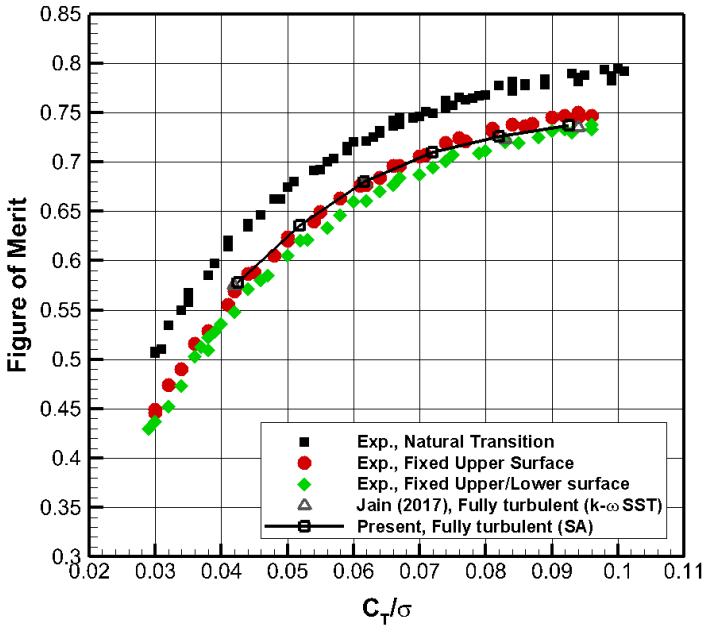

Figure 4.19: Comparison of Figure of Merit against the experiment: fully-turbulent simulations.

4.3.3.4 Result: transition simulations

Figure 4.20 shows predicted Figure of Merit against the experimental data and other available CFD results from transition simulations. For the other CFD results, Jain used the SST-γ-$Re_{\theta t}$ model (non-Galilean invariant) [5], whereas Fitzgibbon et al. used the SST-γ model (Galilean invariant) [53]. In the figure, transition simula-

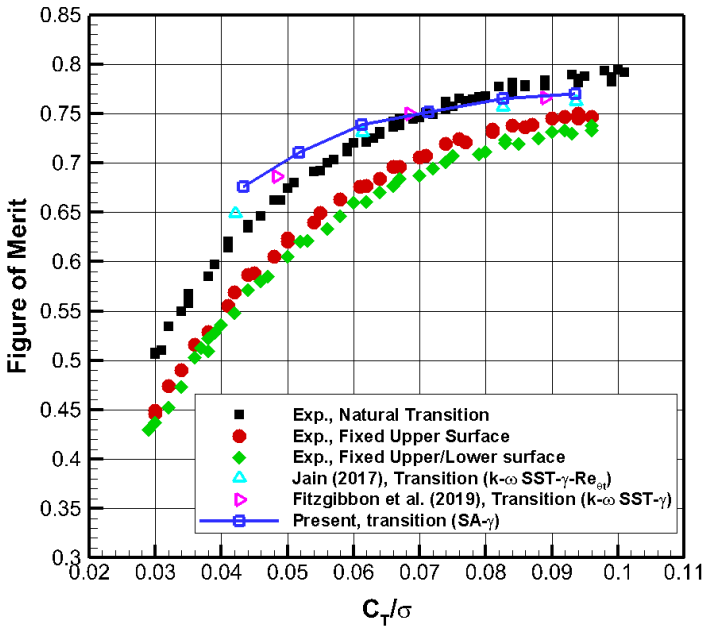

Figure 4.20: Comparison of Figure of Merit against the experiment: transition simulations.

tion results show better comparisons with the natural transition data (black square symbol) than the fixed-surface data (red or green symbols). Overall trends are in reasonable agreement with the experiment, but the slope of the predicted Figure of Merit is slightly different from the experimental measurements; over-prediction of Figure of Merit at low thrust levels and under-prediction at high thrust levels. At the low thrust levels, the SA$-\gamma$ model shows slightly more over-prediction than the other CFD results. There can be some possibilities for this. In the SST-γ-$Re_{\theta t}$ or SST-γ transition model, the local turbulence intensity is calculated with the k and ω from the SST turbulence model. However, in the current $SA-\gamma$ model, the constant turbulence intensity is applied in the computational domain because k and ω are not available. The assumption of the constant turbulence intensity may not be accurate at the low thrust levels where the rotor wake remains near the rotor

disk plane and is possibly re-ingested into the rotor disk plane, which can result in higher turbulence intensity than that at high thrust levels. To investigate the effect of turbulence intensity, other values of turbulence intensity are tested in the later section of the current chapter.

4.3.3.5 Result: effects of crossflow transition

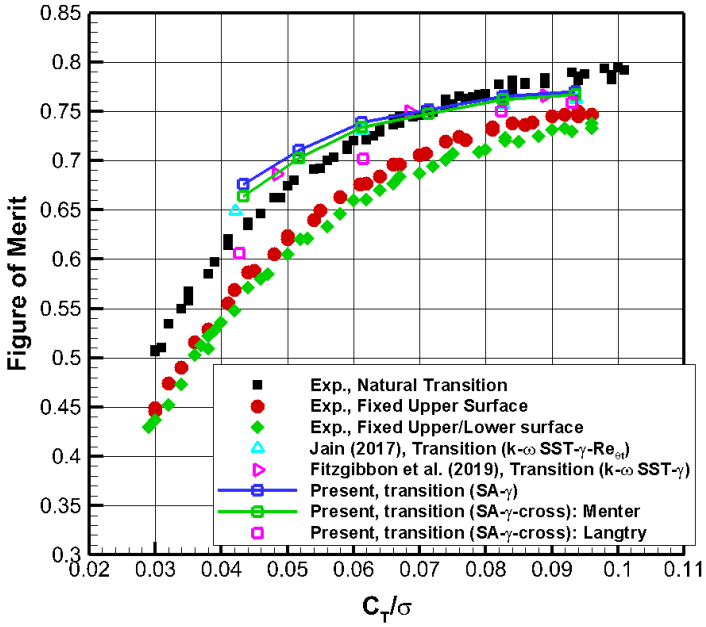

Figure 4.21: Comparison of Figure of Merit against the experiment: the effect of crossflow transition.

The effects of the crossflow transition are investigated with the two crossflow transition models by 1) Menter and Smirnov and 2) Lantry et al.. Figure 4.21 compares the predicted Figure of Merit with and without the crossflow transition models. As it was mentioned earlier, a RMS value $0.5\mu m$ is applied for the Langtry et al.'s crossflow transition model, which is equivalent to a RMS roughness height

of the "polished surface".

In the Figure, Menter and Smirnov's model (green line) predicts slightly lower Figure of Merit at low thrust levels than the baseline transition model but it does not show noticeable effects on the rotor performance. On the other hand, Langtry et al.'s crossflow transition model gives under-prediction of Figure of Merit through the entire thrust levels. Because the calibrations of the two crossflow transition models were performed for h=3.3μm, Langtry's model with the RMS height of 0.5μm should give higher Figure of Merit than the Menter and Smirnov's model. It is considered that the non-Galilean invariance in the Langtry et al.'s model results in the inaccurate predictions for the rotor simulations. It should be mentioned that Langtry's crossflow transition model was also tested for the same rotor in the work by Carnes and Coder [35], and there was no significant effects of the model in the work. However, the work didn't clarify the RMS roughness height of the simulations. In addition, it is not clear whether the non-Galilean invariant variables are corrected or not in the work. Therefore, it is difficult to directly compare the current results with Carnes and Coder's work [35].

4.3.3.6 Result: comparisons of transition locations

Figures 4.22 and 4.23 show contours of predicted turbulence index on the blade surfaces at the low and high collective pitch angles. Measured transition locations in the experiment are added as square symbols in the figure. At the low collective pitch angle ($\theta = 6°$), the SA-γ model shows better agreement with the experimental

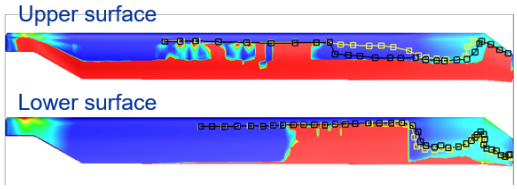

(a) SA-γ.

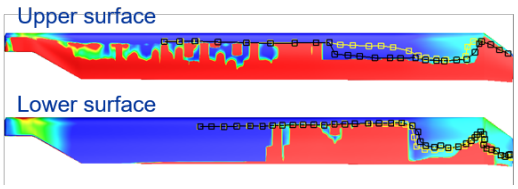

(b) SA-γ-crossflow (Menter and Smirnov).

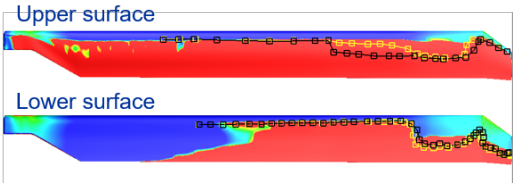

(c) SA-γ-crossflow (Langtry et al.).

Figure 4.22: Comparison of turbulence index contours against the experiment at $\theta = 6°$. CFD: C_t/σ=0.043. Exp: C_t/σ=0.040 (Black). Exp: C_t/σ=0.045 (Yellow)

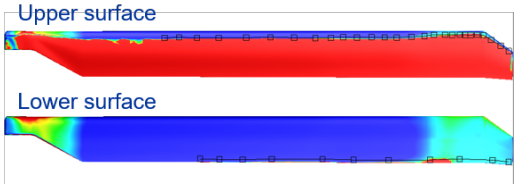

(a) SA-γ.

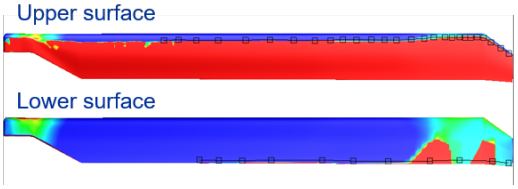

(b) SA-γ-crossflow (Menter and Smirnov).

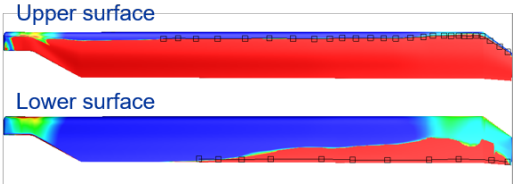

(c) SA-γ-crossflow (Langtry et al.).

Figure 4.23: Comparison of turbulence index contours against the experiment at $\theta = 11°$. CFD: C_t/σ=0.093. Exp: C_t/σ=0.090 (Black).

transition locations at C_t/σ=0.040 (black symbols). Overall, the current results show lagged turbulent areas on the both upper and lower surfaces especially at the inboard and middle sections. Menter and Smirnov's crossflow transition model gives slightly larger turbulent areas than the baseline transition model, but their trends are very similar. On the other hand, in the result from Langtry et al.'s model,

larger turbulent areas are observed on the both upper and lower surfaces than the experiment or Menter's model results. This may be due to the lack of Galilean invariance as it was mentioned in the previous section. At the high collective pitch angle ($\theta = 11°$), all results show very good comparisons with the experiment on the upper surface. On the other hand, on the lower surface, the baseline transition model gives the best comparison. The crossflow transition models captures larger turbulent areas than the experiment near the tip and the trailing edge, but overall agreement looks still reasonable. In the current results, unphysical transition trends observed in Jain's work [5] using non-Galilean invariant model are not found.

4.3.3.7 Result: effect of turbulence intensity

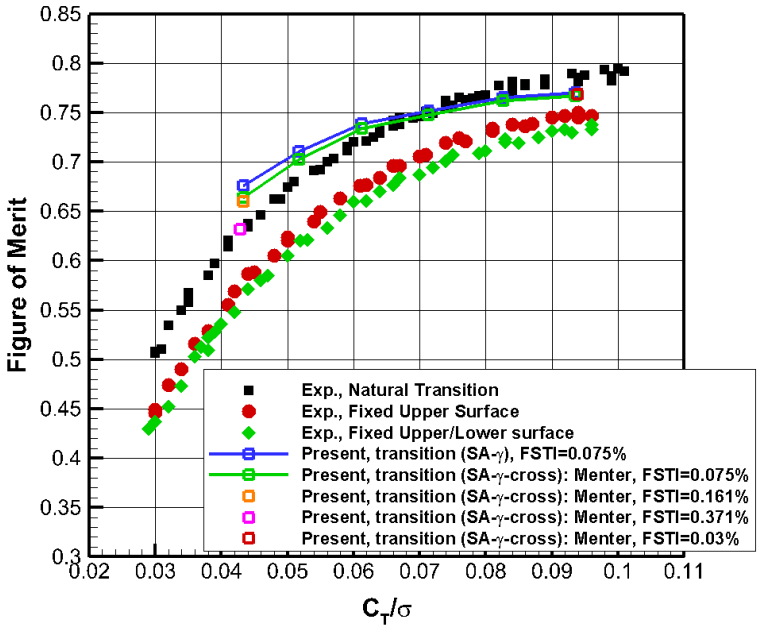

Figure 4.24: Effect of freestream turbulence intensity on Figure of Merit.

To investigate the gap between the predicted Figure of Merit and the exper-

imental data, the effect of freestream turbulence intensity is tested at the low and high collective pitch angles. Figure 4.24 shows results with different freestream turbulence intensity values at the collective pitches of 6° and 11°. At the low collective pitch angle, two higher freestream turbulence intensity values, 0.161% ($N_{crit} = 7$) and 0.371%($N_{crit} = 5$), are tested, whereas at the high collective pitch, a lower freestream turbulence intensity value, 0.03% ($N_{crit} = 11$), is tested. At the low collective pitch angle, Figure of Merit is still over-predicted with the freestream turbulence intensity of 0.161%, but it is well matched to the experiment with 0.371%. Figure 4.25 compares turbulence index on the blade surfaces from the simulations at the low collective pitch. It is seen that the turbulence intensity of 0.371% gives better comparisons with the experimental data at C_t/σ=0.045 than other results. Figure 4.26 shows spanwise distributions of the thrust and power coefficients on the blade for the three freestream turbulence intensity values. For the sectional thrust, the effect of turbulence intensity is minor, whereas there are some differences in the torque distribution at $r/R = 0.55 \sim 0.95$. It is considered that the low thrust level has higher turbulence intensity than the higher thrust levels due to the remaining rotor wake near the rotor disk plane. For this reason, the higher turbulence intensity gives better comparisons with the experimental data at the low thrust level. On the other hand, at the collective pitch of 11°, the low turbulence intensity (0.03%) gives almost the same Figure of Merit, still with under-prediction. Because 0.03% is already very low, it is expected that a even lower value like 0.01% may give the same result. Since the lower turbulence intensity does not improve the prediction, one of other possibilities for the under-prediction, the effect of blade aeroelasticity,

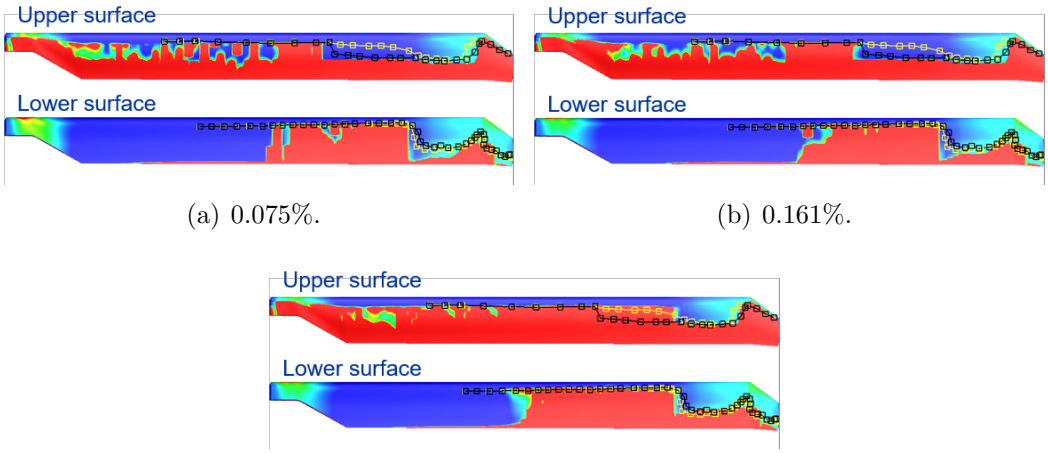

(a) 0.075%. (b) 0.161%.

(c) 0.371%.

Figure 4.25: Effect of the freestream turbulence intensity on turbulence index contours at $\theta = 6°$. CFD: C_t/σ=0.043. Exp: C_t/σ=0.040 (Black). Exp: C_t/σ=0.045 (Yellow).

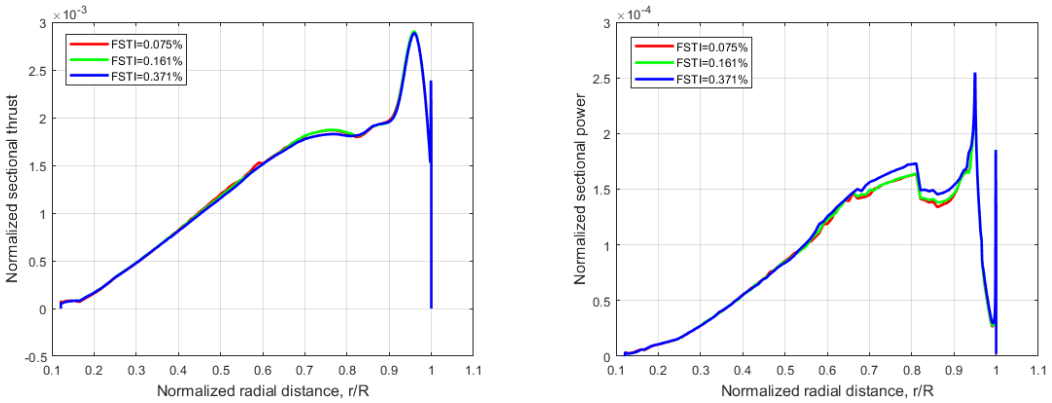

(a) Sectional thrust. (b) Sectional power.

Figure 4.26: Comparison of the sectional thrust and power distributions at $\theta = 6°$.

is investigated in the next section.

4.3.3.8 Result: effect of aeroelasticity at the high thrust condition

The effect of blade aeroelasticity on the rotor performance is examined at the high thrust level ($\theta = 11°$) with a tip twist. The tip twist angle, 2°, is estimated based on Jain's work [85] in which the effect of aeroelasticity is studied with

CFD/CSD simulations for the PSP rotor. Figure 4.27 compares twist distributions of the original blade and the blade with the tip twist angle 2°. Figure 4.28 shows

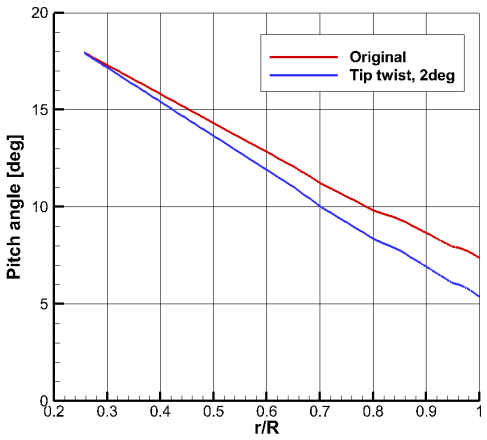

Figure 4.27: Comparison of blade pitch distributions with and without the tip twist.

the predicted Figure of Merit with the tip twist (red diamond) and the original predictions. In the figure, the additional tip twist actually gives reduced thrust and Figure of Merit, and thus the predicted value is less than that at the collective pitch of $\theta = 10°$ although the predicted value is still on the curve of Figure of Merit. The work by Jain [85] also shows very similar trends to the current study. Therefore, the effect of blade aeroelasticity is not a source of the under-prediction of Figure of Merit at the high thrust level. To identify a correct reason for that, further studies are required in the future work.

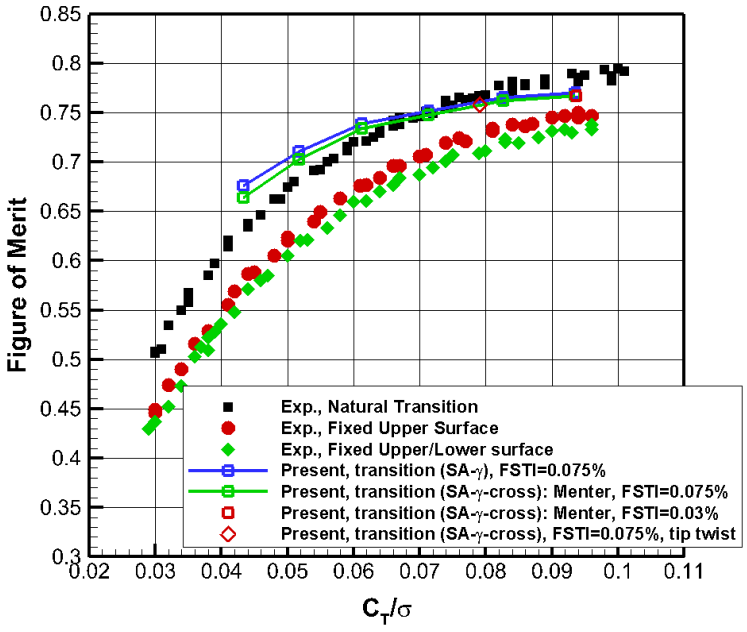

Figure 4.28: Effect of blade aeroelasticity on the rotor performance at $\theta = 11°$.

Chapter 5: Effect of time-marching on the wake structure breakdown in a hovering rotor simulation

This section discuss the second part of the current dissertation, the wake breakdown of a hovering rotor. The section investigates the effect of time-marching with 1) time step sizes, 2) the BDF1 and BDF2 schemes, and 3) a temporal damping of the BDF scheme. The effect of grid size of the background mesh is also studied, since it affects the effective CFL numbers. Simulations are performed at a collective pitch of 11° for the NASA Langley's PSP hovering rotor, and the computational setup presented in Chapter 4.3.3 was used. To investigate the effect of temporal damping of the BDF scheme, the blended BDF formulation derived in Chapter 2.2.7.1 was applied in simulations.

5.1 Effect of the time step size

The effect of the time step size on wake breakdown is investigated for four different time step sizes, 0.0625°, 0.125°, 0.25° (baseline) and 0.5°. To save computational costs, simulations were restarted at the solutions of revolution 20 with time step size 0.25° and run for 2 additional revolutions with the different time step sizes. Figure 5.1 compares wake structures (Q-criterion) at revolution 22. All

results show wake breakdown with the secondary vortex braid instabilities, but the largest time step size, 0.5°, gives the most severe wake breakdown. As the time step size decreases, there are less secondary vortex braids in the solutions, and the wake structures from the time step sizes 0.0625° and 0.125° are relatively similar. Considering the relation between the CFL number and the time step size, a smaller CFL number gives less secondary vortex braids.

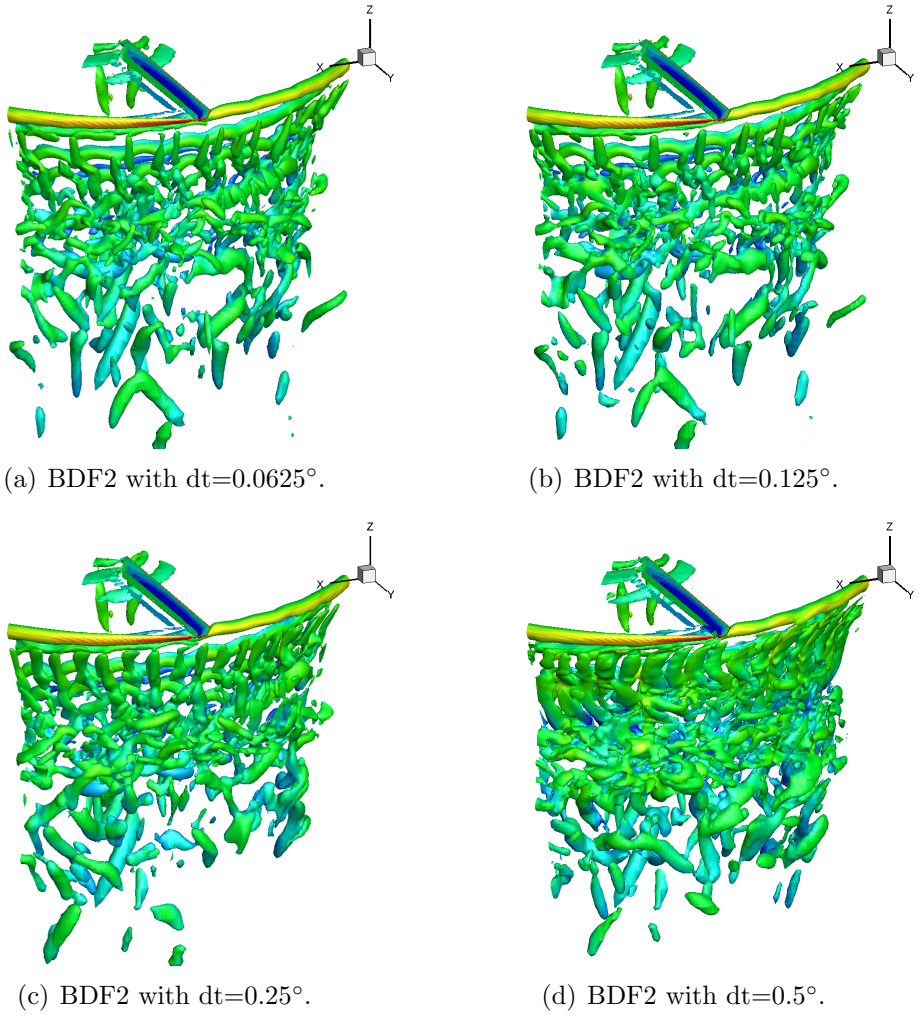

(a) BDF2 with dt=0.0625°.

(b) BDF2 with dt=0.125°.

(c) BDF2 with dt=0.25°.

(d) BDF2 with dt=0.5°.

Figure 5.1: Effect of the time step size on wake structures (Q-criterion=0.001) at revolution 22.

Figure 5.2 compares the thrust and torque coefficients from the simulations

during the last 1 revolution. A range of the Y-axis is adjusted to see differences between the results more clearly. In the figures, the larger time step size gives more high frequency oscillations in the thrust and torque although their time-averaged values are similar. Considering the wake structures shown in Fig. 5.1, it is considered that wake breakdown with the secondary vortex braids affect the upstream rotor wake and thus make the rotor performance more oscillatory.

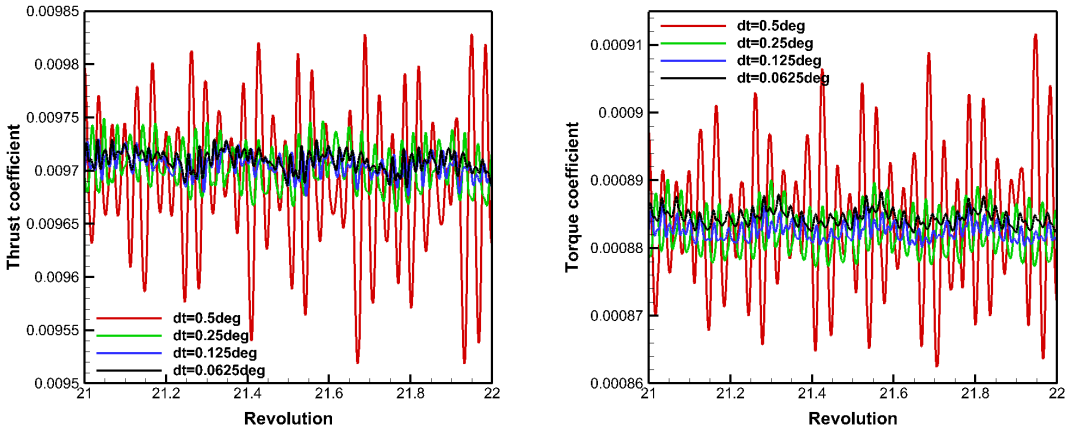

(a) Thrust coefficient.

(b) Torque coefficient.

Figure 5.2: Effect of the time step size on the thrust and torque coefficients.

Figure 5.3 shows FFT results of the thrust coefficients up to 80/revs for the different time step sizes. In the figure, the larger time step size gives more high frequency components in the thrust coefficient. In the results from the time step size 0.5°, two most dominant frequencies are 32/rev and 24/rev. However, in the results from the time step size of 0.25°, 32/rev and 31/rev are most dominant. In the result from the time step sizes 0.125° and 0.0625°, 4/rev is the most dominant frequency, and the higher frequency components observed in the previous results are almost gone. It is seen that the wake breakdown significantly increases high

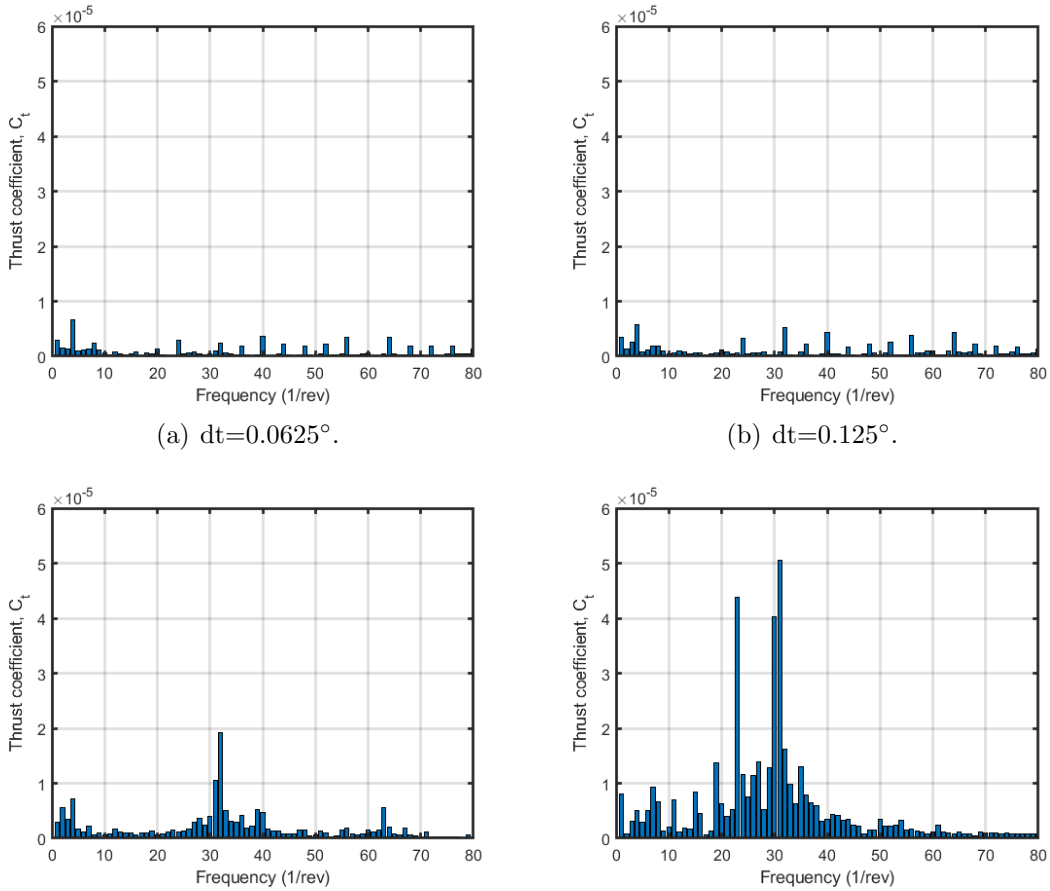

(a) dt=0.0625°. (b) dt=0.125°.

(c) dt=0.25°. (d) dt=0.5°.

Figure 5.3: Comparison of frequency components in the thrust coefficient for different time step sizes.

frequency components in the predicted rotor performance.

Figure 5.4 compares sub-iteration convergences of the background mesh. The convergences from the time step sizes 0.0625° to 0.25° are very similar although there some differences in the wake structures. For the time step size 0.5°, it shows the residual drop more than one order but has the least convergence.

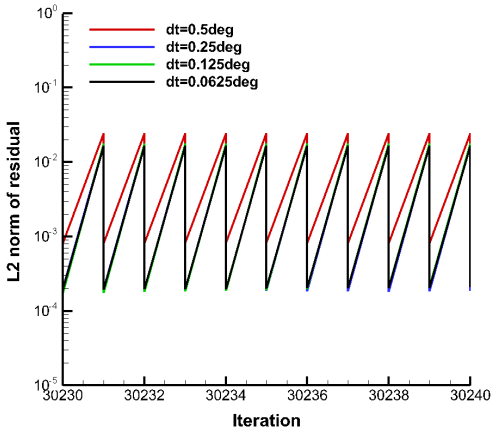

Figure 5.4: Comparison of sub-iteration convergence of the background mesh.

5.2 Effect of the background mesh

The effect of the background mesh is investigated with a finer background mesh. The cell size is not directly related to the time-marching, but it still affects the CFL number. In the original mesh, a smallest cell size in the clustering region is 6% of the chord length, whereas, in the finer mesh, the minimum cell size is 4% of the chord length. Figure 5.5 compares wake structures from two cases at revolution 22. In the results, the finer background mesh gives more secondary vortex braids in the near and far wakes than the original background mesh.

Figure 5.6 compares predicted thrust and torque coefficients from the two cases. In both the thrust and torque coefficients, the finer background mesh gives larger magnitudes of oscillations. For the torque coefficient, the finer mesh gives a reduced time-averaged value by 1.13%, but for the thrust coefficient, the difference between the time-averaged values is less than 0.2%.

In Figure 5.7, FFT results of the thrust coefficient are shown. In the results,

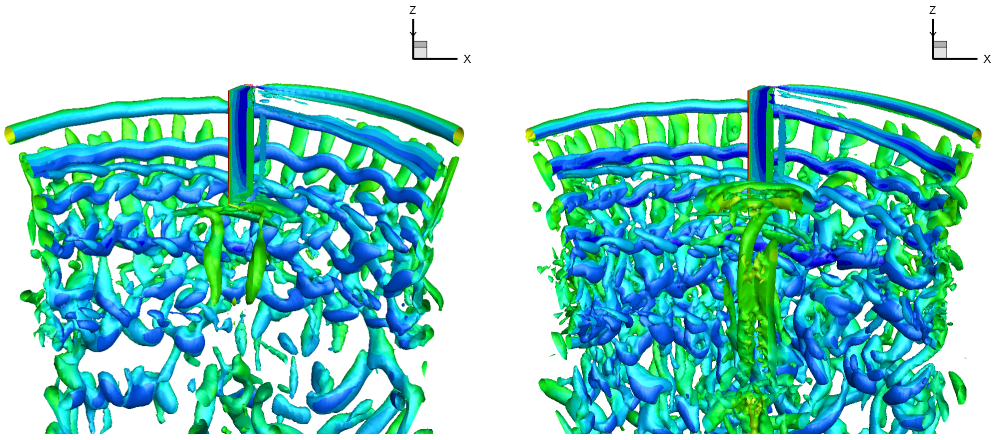

(a) Original background mesh. (b) Finer background mesh.

Figure 5.5: Effect of a grid size on wake structures (Q-criterion=0.001) at revolution 22.

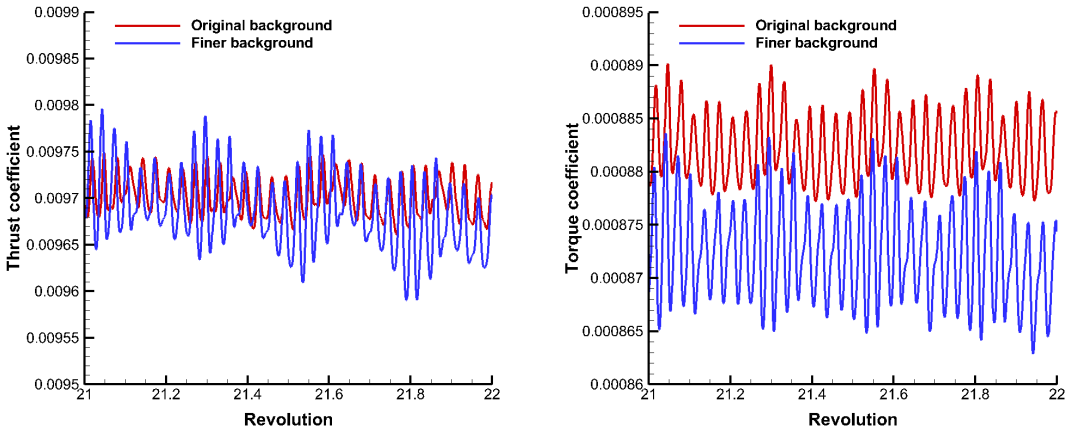

(a) Thrust coefficient. (b) Torque coefficient.

Figure 5.6: Effect of a grid size on the thrust and torque coefficients.

32/rev is the most dominant component, but the finer background mesh gives more higher frequency components in the thrust coefficient.

Figure 5.8 compares sub-iteration convergences of the background mesh. The finer mesh has slightly higher magnitudes of the residual than the original mesh, but the orders of the residual drop of the two cases are very similar.

From the point of view of the CFL number, a smaller mesh size means a larger

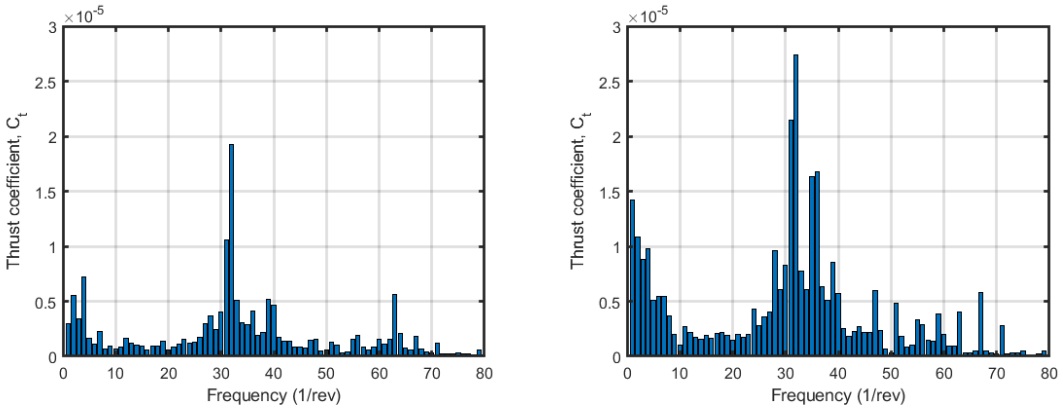

(a) Original background mesh. (b) Finer background mesh.

Figure 5.7: Effect of a grid size on the thrust and torque coefficients.

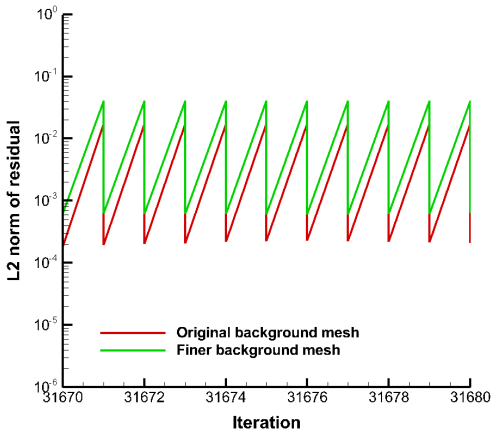

Figure 5.8: Comparison of sub-iteration convergence of the background mesh.

CFD number. As it was observed in the results from the different time step sizes, a larger CFD number gives more wake breakdown with secondary vortex braids.

5.3 Comparison between the BDF2 and BDF1 schemes

The effect of time marching schemes is investigated between the BDF2 and BDF1 schemes. In Figure 5.9, wake structures are compared between the BDF2 and BDF1 results at revolution 22. Computations are performed using the BDF2

scheme up to revolution 20. Then, solutions are restarted with the BDF2 or BDF1 and run for additional two revolutions. In the BDF2 result, the tip vortex becomes

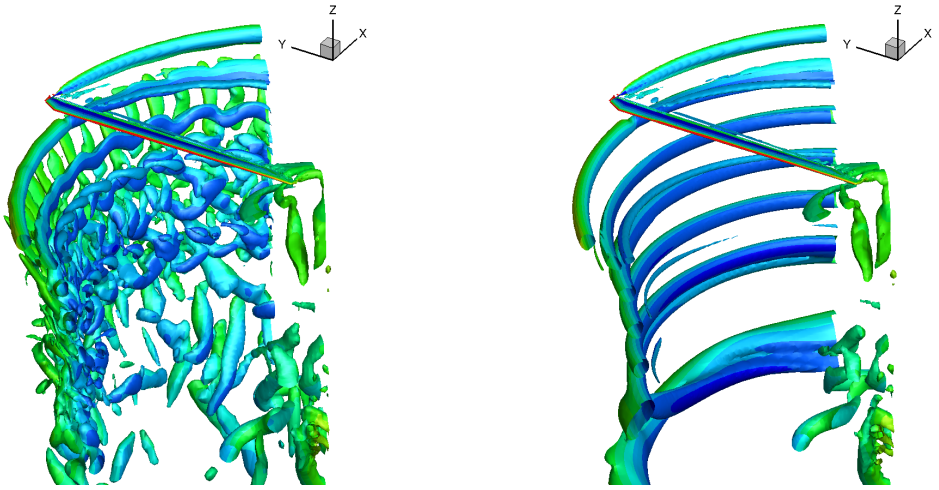

(a) BDF2. (b) BDF1.

Figure 5.9: Comparison of wake structures (Q-criterion=0.001) at revolution 22: BDF1 Vs. BDF2.

unstable in the near wake due to the secondary vortex braid instabilities, and wake structure breakdown occurs from the third blade passage. As a result, it is difficult to observe coherent vortical structures in the middle and far wake regions. On the other hand, in the BDF1 result, the secondary vortex instability is gone, and wake structures become very stable with the tip vortices preserved up to the fifth blade passages. The reduced temporal accuracy gives the more stable and diffused wake structures.

Figure 5.10 compares predicted thrust coefficient and Figure of Merit using the BDF2 and BDF1 schemes. In the figure, BDF2 shows high frequency oscillations in the thrust coefficient and Figure of Merit, whereas BDF1 gives settled down results with less oscillations. For the Figure of Merit, the result from the BDF2 slightly

changes even after revolution 20, but the BDF1 result is relatively flat.

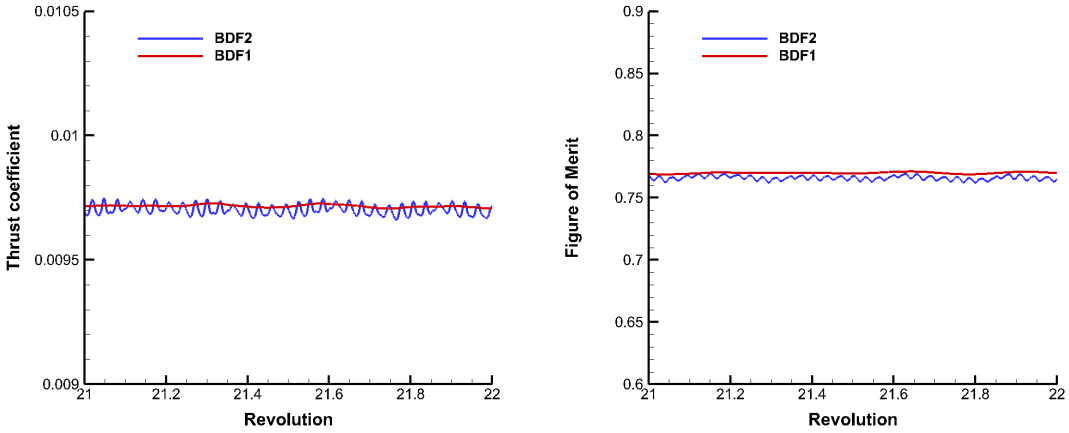

(a) Thrust coefficient.

(b) Figure of Merit.

Figure 5.10: Comparison of integrated rotor performance: BDF2 Vs. BDF1.

Figure 5.11 shows spanwise distributions of thrust and torque loadings from the BDF2 and BDF1 schemes. Overall trends are very similar, but there is a gap in the torque loading at r/R =0.95 caused by differences in the returning vortex and the wake structures. In the BDF2 result, the returning vortex is destabilized by the secondary vortex braids, but it is not the case in the BDF1 result. The more stable wake structures in the BDF1 results in a larger drop in the section torque distribution around 95% of the spanwise section.

5.4 Effect of temporal damping: Blended BDF scheme

Finally, the effect of temporal damping of the time-marching scheme is investigated using the blended BDF scheme. Figure 5.12 shows wake structures (Q-criterion) for different temporal damping values from zero to one. In the figure, the BDF2 ($\epsilon = 0.0$) and the blended BDF with $\epsilon = 0.02$ give unstable wake structures

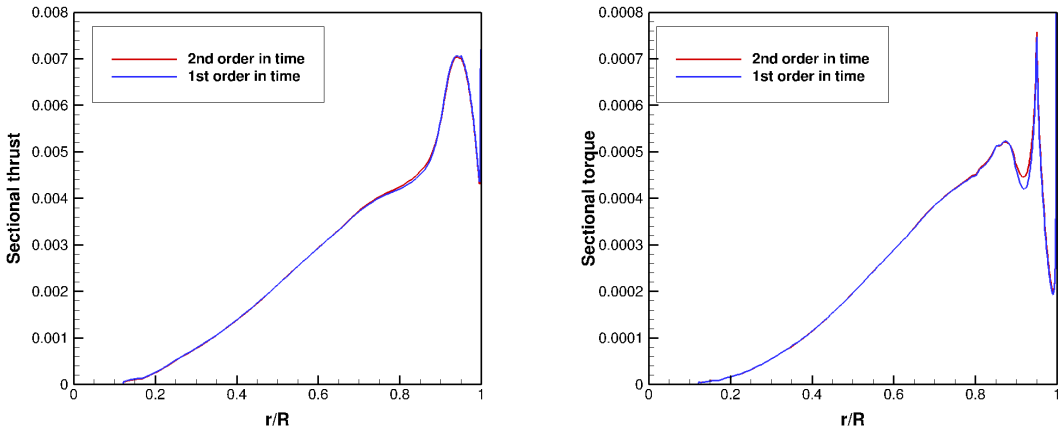

(a) Sectional thrust.

(b) Sectional torque.

Figure 5.11: Comparison of blade loadings: BDF2 Vs. BDF1.

with lots of secondary vortex braids. The blended BDF with $\epsilon = 0.02$ give slightly less secondary vortex braids in the near wake, but overall trends are very similar to the BDF2 result. It is seen that the returning vortex from the previous blade also becomes unstable by the instabilities in the both results. In the previous section, it was shown that the unstable returning vortex caused the lower distribution of the torque at $r/R = 0.95$ of the blade spanwise section. For the blended BDF with $\epsilon = 0.1$, the wake structures becomes more stable in the near wake region up to the third blade passages, and wake breakdown occurs in the middle and far wake regions, which is more physical than the previous two results. Also, it shows significantly less the secondary vortex braid instabilities in the flow field. Finally, for the BDF1 ($\epsilon = 1.0$) result, tip vortices are very well preserved for 4-5 blade passages, but perhaps, it is too stable.

Figure 5.13 compares thrust and torque coefficients for the BDF2 ($\epsilon = 0.0$), BDF1 ($\epsilon = 1.0$), and the blended BDF with ϵ=0.02 and 0.1. Range of Y-axis is

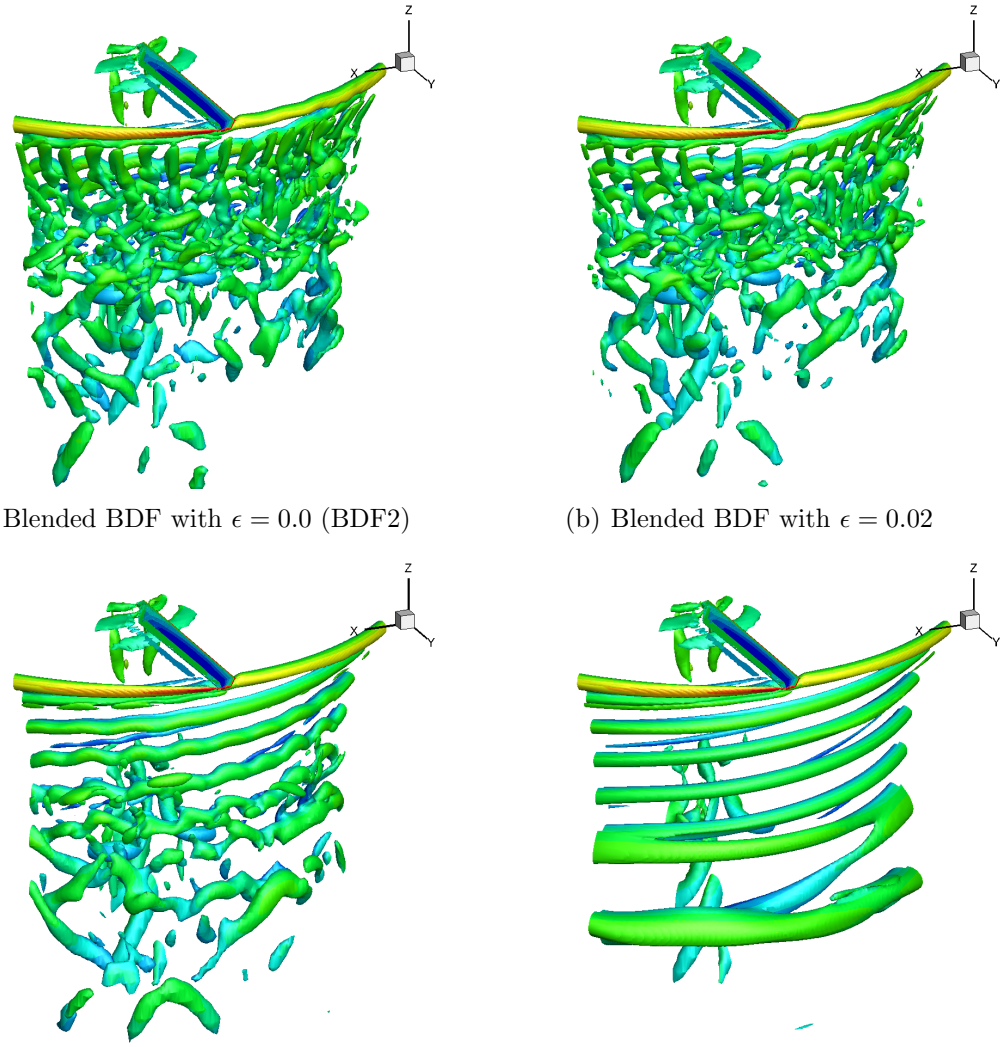

(a) Blended BDF with $\epsilon = 0.0$ (BDF2)

(b) Blended BDF with $\epsilon = 0.02$

(c) Blended BDF with $\epsilon = 0.1$

(d) Blended BDF with $\epsilon = 1.0$ (BDF1)

Figure 5.12: Comparison of wake structures (Q-criterion=0.001) for different temporal damping.

adjusted from Fig. 5.10 to see differences between each other more clearly. As shown in the previous section, the BDF2 gives lots of high frequency oscillations by the secondary vortex instability, whereas BDF1 doesn't show the oscillations. For the blended BDF with ϵ=0.02, although magnitudes of oscillations in the thrust and torque coefficients decrease slightly from the BDF2 results, overall trends are very similar to the BDF2 results. For the blended BDF with ϵ=0.1, it shows less high

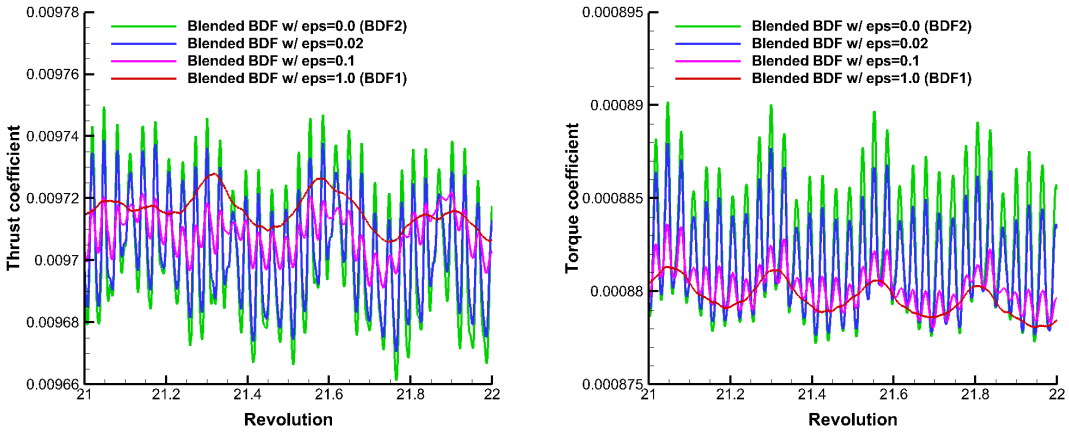

(a) Thrust coefficient. (b) Torque coefficient.

Figure 5.13: Comparison of integrated rotor performance.

frequency oscillations in the thrust and torque coefficients than the results from the BDF2 or the blended BDF with ϵ=0.02. As it was discussed earlier, it is considered that the high frequency components in thrust and torque coefficients are caused by the secondary vortex braid instabilities in the wake.

Figure 5.14 shows FFT result of the thrust coefficients. In the figure, a larger damping value gives less high frequency components in the thrust coefficient. The BDF2 or the blended BDF with ϵ=0.02 has 32/rev as the most dominant component. On the other hand, in the results with blended BDF with $\epsilon = 0.1$, the magnitude of 32/rev is less than that of 4/rev, and in the BDF1 result ($\epsilon = 1.0$), 4/rev is the most dominant and higher frequency components are not observed well.

Figure 5.15 shows sub-iteration convergences of the background mesh for the different temporal damping values. All cases show very similar trends of the residual drop except the blended BDF with $\epsilon = 1.0$ (BDF1) despite significant differences in the wake structures and the predicted rotor performance. It is considered that

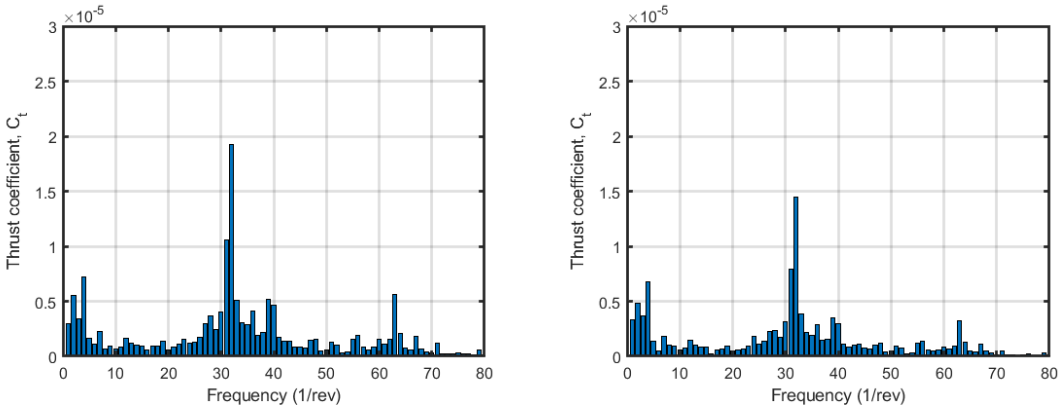

(a) Blended BDF with $\epsilon = 0.0$ (BDF2)

(b) Blended BDF with $\epsilon = 0.02$

(c) Blended BDF with $\epsilon = 0.1$

(d) Blended BDF with $\epsilon = 1.0$ (BDF1)

Figure 5.14: Comparison of frequency contents in the thrust coefficients.

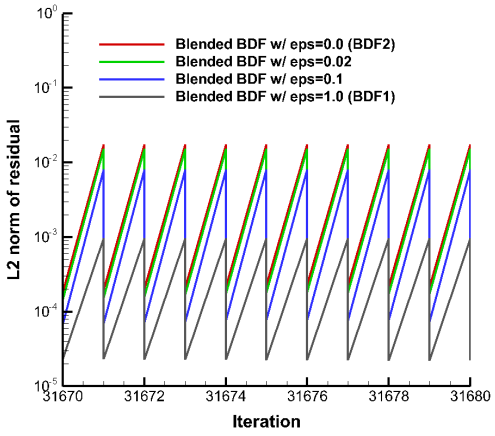

Figure 5.15: Comparison of sub-iteration convergence of the background mesh.

the global convergence of the background may not be directly related to the wake breakdown.

In summary, the current study shows that the time-marching is one of factors affecting the numerical prediction of wake breakdown of a hovering rotor. It was shown that reducing the CFL number with a smaller time step size and/or a larger cell size makes wake structures more stable with less secondary vortex braids. In addition, adding a small amount of temporal damping helps relieve the problem. However, reducing the CFL number may result in an increase of computational times due to a smaller time step size or the dissipation of wake structures due to larger cell sizes. On the other hand, adding a small amount of temporal damping using the blended BDF scheme does not lose temporal accuracy significantly while it reduces unphyscial early wake breakdown. Therefore, it can be used as an engineering solution of the problem.

Chapter 6: Conclusion and Summary

6.1 Galilean invariant transition model for the S–A turbulence model

Prediction of laminar-turbulent transition is still one of the key challenges in general purpose CFD simulations. Although Langtry-Menter's $\gamma - Re_{\theta t}$ model has become one of the most successful models in industrial CFD applications since its release, it has several limitations such as 1) lack of Galilean invariance, 2) complexity in local correlations (the critical momentum thickness Reynolds number transport equation), and 3) dependence on the variations in the SST turbulence model. These limitations motivates the first goal of the current study, the development of a Galilean invariant transition model for the SA turbulence model.

In the present work, Menters one-equation γ transition model is coupled to the SpalartAllmaras turbulence model. Calibrations of the transition model are performed on flat plate cases to ensure accurate predictions, and a new set of correlation constants are proposed. Convergence of the transition model is improved for implicit time marching methods by applying the positivity of implicit operators. A constant freestream turbulence intensity from the experiment is employed to account for experimental flow conditions. The transition model is extended with crossflow transition models. The model is validated against various 2-D and 3-D

transition cases and shows good comparisons with experimental data.

6.1.1 Key observation

Transition simulations with a constant turbulent intensity from experiments give very good comparisons with the experiment. The initial condition of the SA turbulent model does not need to be adjusted, unlike Nichols's work [42].

Application of the positive principle in the implicit operators significantly improves convergence of the model for both 2-D and 3-D cases and does not give non-physical negative intermittency values.

Validations of the SA-γ model is performed for four 2-D subsonic airfoil cases. Reynolds number ranges from 0.2×10^6 to 4×10^6 and freestream turbulence intensity is from 0.05% to 0.15%. In the results, SA-γ simulations significantly improved drag prediction from the fully turbulent simulations for all four cases. The model captures the effect of laminar-turbulent transition on the skin friction, pressure coefficient, and drag coefficient very well. The grid study results show that the SA-γ model gives robust prediction for different meshes. The model shows converging trend of lift and drag coefficient as the mesh becomes finer, and the SA-γ model does not show nonphysical oscillations in the results with the finest mesh. At the low Reynolds number (Re=0.2×10^6), the transition model predicts the separation-induced transition very well with accurate locations of the laminar separation and turbulent reattachment.

The SA-γ transition model is applied to three-dimensional cases with two

crossflow transition models. Simulations are performed for the following three cases: 1) NLF(2)-0415 swept wing, 2) Inclined 6:1 Prolate Spheroid, and 3) NASA Langley's PSP hovering rotor.

For the NLF(2)-0415 swept wing, both crossflow transition models give better comparisons of transition locations with the experiment than the baseline transition model. For Langtry et al.'s model, it accounts for the surface roughness and reasonably captures the effect of surface roughness on crossflow transition.

For the inclined 6:1 Prolate Spheroid, the baseline transition model does not capture the trends of the experiment through the entire range of angles of attack. On the other hand, both crossflow transition models give reasonable agreement with the experiment at the medium and high angles of attack ($\alpha = 10^\circ$ and 15°). Overall, the crossflow transition model by Menter and Smirnov shows earlier transition onset than the model proposed by Langtry.

Finally, the SA-γ transition model is applied to the NASA Langley's PSP rotor simulations. The experimental freestream turbulence intensity is unknown, and a range of the freestream turbulence intensity in other CFD simulations is very wide: from 0.07% to 1.0%. In the current work, a freestream turbulence intensity of 0.075% is applied for simulations, and other values are tested at low and high thrust levels based on the results. Overall, the current prediction shows reasonable agreements with the experiment and similar trends with other CFD results; over-prediction of Figure of Merit at low thrust levels and under-prediction at high thrust levels. The effect of crossflow transition model is investigated using the two crossflow transition models. From the result, the crossflow transition model by Menter and Smirnov

shows minor effects, whereas the model by Langtry et al. shows significant under-prediction of the Figure of Merit than the baseline results. Langtry et al.'s model may give different results due to the lack of Galilean invariance and/or inaccurate surface roughness heights. To figure out the correct reasons, further investigations are required with additional rotor test data.

At the low and high thrust levels, the effect of freestream turbulence intensity is investigated. At collective pitch of 6°, a higher turbulence intensity value, 0.371% gives better comparison with the experiment than the original value, 0.075%. It is considered that at low thrust levels the rotor wake remains near the rotor and turbulence may be re-ingested into the rotor disk plane, which results in an increase of turbulence intensity of the inflow. On the other hand, at a high thrust level (collective pitch of 11°), a lower turbulence intensity, 0.03%, does not improve correlations with the experiment. The effect of aeroelasticity is investigated with the tip twist, but it does not give a solution for the under-prediction either. Further investigations are required to figure out the under-prediction at the high thrust level.

The predicted transition locations on the blade surfaces are compared with the experiment. The new baseline transition model with the crossflow transition model by Menter and Smirnov gives reasonable comparisons with the experiments without unphysical transition behaviors near the swept tip of the blade where the blade-vortex interaction occurs. On the other hand, the crossflow transition model by Langtry et al. (non-Galilean invariant) gives excessive turbulent areas on the blade surfaces.

6.1.2 Contributions of Thesis

Key Contributions of this thesis are as follows:

1. Coupled Menter's 1-eq γ transition model to the S-A turbulence model and accounted for experimental conditions by employing a constant turbulence intensity

2. Improved convergence of the transition model with application of the positivity in the implicit operator

3. Extended the transition model by coupling two crossflow transition models and re-calibrated the model constants

4. Preformed hovering rotor simulations with the transition model and show that the Galilean invariant model doesnt show unphysical transition behaviors on the blade surfaces

6.1.3 Recommendations for Future Work

1. For the PSP hovering rotor, the SA-γ transition model slightly over-predicts Figure of Merit at the low thrust levels than the experiment and other CFD results. It is considered that this is due to higher turbulence intensity in the experiment caused by turbulent inflow near the rotor disk plane. Further studies are required to investigate correlations between turbulence intensity and thrust levels with additional experimental data.

2. Results from using the crossflow transition model by Langtry et al. show good comparisons with the experimental data for NLF(2)-0415 wing or Prolate Spheroid. However, it captures excessive effects of crossflow transition for the NASA Langley's PSP hovering rotor. It is considered that this may be due to lack of Galilean invariance of the model, and the effect of non-Galilean invariance in the crossflow transition model needs to be further investigated.

3. Surface roughness is one factor that affects laminar-turbulent transition. Although Langtry et al.'s crossflow transition model accounts for roughness height as a model input, the baseline turbulence and transition models are only for a smooth surface. For more physical simulations of wing, fuselage, or rotor blade, the effect of surface roughness on the transition needs to be considered. Dassler [40] and Langel [41] proposed the roughness-induced transition models that employs an additional transport equation for the roughness amplification factor. A similar approach can be tried for the current SA-γ transition model.

4. In a recent study by Jung et al. [86], it was found that the SA-γ model becomes inaccurate at high Reynolds number flow ($Re \geq 9 \times 10^6$) and gives earlier transition than it should be. The capability of the SA-γ transition model for high Reynolds number flow should be improved with further calibrations of the model constants and/or a machine-learning approach.

6.2 Wake breakdown of a hovering rotor

Wake breakdown of a rotor has been observed in CFD simulations with applications of high-order numerical schemes and/or the adaptive mesh refinement. Wake breakdown begins with the secondary vortex braid instability, and it destroys the vortical structures except the very near wake structures. Although, a recent experimental study confirms the existence of the secondary vortex braids, the extent of the instability in CFD simulations is considered physically incorrect.

The second objective of the present study is to investigate the effects of time-marching on the wake breakdown of a hovering rotor. Several factors are tested such as 1) time step sizes, 2) temporal accuracy (BDF2 and BDF 1 schemes), and 3) adding a temporal damping to the BDF2 scheme. For this purpose, a blended formulation of the BDF1 and BDF2 scheme is derived with a temporal damping variable and coupled to dual-time stepping. Simulations are performed for NASA Langleys PSP hovering rotor, and wake structures (iso surface of Q-criterion), integrated rotor performance, and FFT analysis of the thrust coefficient are examined.

6.2.1 Key observation

6.2.1.1 Effect of the time step size

The effect of the time step size on the wake breakdown is analyzed for four different time step sizes, 0.0625°, 0.125°, 0.25°, and 0.5°. The larger time step size gives more secondary vortex braids with higher frequency oscillations in the thrust

and torque coefficients although their converged time-averaged values are not significantly different. The secondary vortex braid instability affects the tip vortical structures, resulting in high frequency oscillations in the predicted rotor performance. The larger time step size shows higher magnitudes of frequency contents of the thrust coefficient in the FFT analysis.

6.2.1.2 Effect of background mesh

The effect of grid size of the background mesh is checked for two different background mesh. Although it is not a time-marching factor, it does modify the effective CFL numbers. The smallest cell size of the original mesh is 6% of the chord length, whereas, the finer mesh has 4% of the chord length in the refined region. Regarding wake structures, the finer background mesh gives more secondary vortex braids in the near and far wake regions than the original background mesh. However, because both meshes show severe wake breakdown, it is difficult to identify the tip vortex after only 2 or 3 blade passages. In the FFT analysis of the thrust coefficient, 32/rev is the most dominant component for both meshes, but the finer background mesh gives more high frequency components.

6.2.1.3 Effect of temporal accuracy

Effect of temporal accuracy on the wake breakdown is studied with the BDF2 and BDF1 scheme. The BDF2 scheme gives lots of secondary vortex braids in the wake structures, whereas BDF1 shows very stable vortical structures without any

secondary vortex braids. However, BDF1 result may be too stable considering the experimental work by Wolf [7]. In the thrust and torque coefficients, the BDF2 gives high frequency oscillations, whereas the BDF1 shows very flat trends. For the spanwise distributions of thrust and torque coefficients, the BDF1 gives more drop of torque coefficient at r/R=0.95 where the returning vortex interacts with the blade because the wake structure (tip vortex) from the BDF1 is more stable and diffused than that from the BDF2 result.

6.2.1.4 Effect of temporal damping

The BDF2 scheme has dominant dispersion errors, whereas the BDF1 scheme has more dissipation errors. The effect of temporal damping is checked with the blended BDF scheme. In the results, a small amount of the temporal damping (10% of the BDF1 scheme) reduces the secondary vortex braids and delays wake structure breakdown, which results in more physical wake structures. High frequency oscillations in the predicted rotor performance also decrease with the temporal damping. The blended BDF scheme with a temporal damping can be used as an engineering solution of the wake breakdown for more physical wake structures in a rotor simulation without significant loss of temporal accuracy.

6.2.2 Contributions of Thesis

Key Contributions of this thesis are as follows:

1. Showed that the time-marching is a factor affecting the wake breakdown in a

hovering rotor simulation

2. Derived a blended formulation of the BDF schemes with a temporal damping variable

3. Demonstrated adding a small amount of temporal damping to the BDF scheme gives more physical wake structures with less secondary vortex braid instability

4. Proposed an engineering solution of the wake breakdown for more physical wake structures

6.2.3 Recommendations for Future Work

1. Duraisamy [87] proposed a time-limited implicit scheme. A key idea behind the scheme is to reduce the temporal accuracy of the scheme locally where the time integration is not smooth so that the scheme is non-oscillatory in time. The scheme can be compared with the blended BDF scheme.

2. Abras et al. [24–26] shows a rotating torus mesh with a blade reduces wake breakdown. The blended BDF scheme with a rotating torus mesh needs to be tested to check if the combination reduces non-physical wake breakdown further.

3. The blended BDF scheme is implemented in flow solvers at the University of Maryland. It would be useful if the scheme is implemented in DoD flow solvers such as NASA's OVERFLOW or SAMCART of CREATE-AV Helios.

Appendix A: Transition Prediction

A.1 e^n method based on linear stability theory

e^n method [88–90] is based on linear stability theory. Linear stability theory is based on solutions of the the Orr-Sommerfeld equation [91, 92]. The equations are derived from the Navier–Stoke equations with assumptions that flow is locally parallel and flow components consist of mean and small perturbations. The velocity perturbations are given as a perturbation stream function as

$$\Psi = \phi(y) A_0 e^{[i(\alpha x - \omega t)]} \tag{A.1}$$

where ϕ is an amplitude function, y is the wall normal coordinate, A_0 is an undetermined coefficient, and x is a streamwise coordinate. If the perturbation amplitude grows, then the boundary layer becomes unstable and transition begins, whereas the boundary layer becomes stable if the perturbation amplitude decays. The Orr-Sommerfeld equation can be extended to include the effects of non-parallel flow by using the Parabolized Stability Equations (PSE) [93].

In e^n method [88–90], transition is triggered once the perturbation amplitude ratio (e^n) is approximately equal to the critical amplification ratio. The exponent

of the critical amplification ratio is called the critical N factor, and a typical range of that is from 7 to 9 for aerodynamic flows. e^n methods have been widely used in many design and analysis codes such as XFOIL [43], LILO [94], and LASTRAC [95] and have given very good comparisons with experimental data.

However, there are some difficulties to apply e^n method in 3-D CFD simulations. First of all, the stability theory requires non-local operations such as the integration along the boundary layer or tracking perturbations along the streamlines. Not only are they not available or desirable in modern CFD methodology, but also they cause many issues for complicated 3-D geometries. Secondly, full application of e^n method requires to track all possible frequencies that can reach the critical amplification factor. Although this can be simplified with the database look up, it is still computationally expensive. To apply the e_n method in general problems, further simplifications may need to be applied such as approximations by Drela and Giles [43]. Finally, to use the e^n method, additional boundary layer codes are required. Because CFD simulations do not provide sufficient solutions for the e^n method, CFD flow solvers are coupled to the e^n method and boundary layer prediction codes in most work [96–98].

A.2 Local correlation methods

Local correlation methods are based on empirical relations between the transition onset and the transition momentum thickness Reynolds number or the vorticity Reynolds number calculated from the freestream turbulent intensity and pressure

gradient parameter. If a local value exceeds the critical value, transition process begins. Many PDE-based methods are also based on local correlations methods, but in this section, only non PDE-based methods are presented.

A.2.1 Mayle's Correlation

Mayle's correlation [28] for transition momentum thickness Reynolds number is given as a function of the freestream turbulence intensity as

$$Re_{\theta t} = 400Tu^{-5/8} \tag{A.2}$$

The correlation is for flow over zero-pressure gradient flat plate only.

A.2.2 Abu-Ghannam and Shaw Correlation

The Abu-Ghannam and Shaw correlation [99] accounts for not only the effect of the freestream turbulence intensity but also the pressure gradient parameter on the transition onset as

$$Re_{\theta t} = 163.0 + \left\{ F(\lambda_\theta) - \frac{F(\lambda_\theta)}{6.91} Tu \right\} \tag{A.3}$$

$$F(\lambda_{\theta L}) = \begin{cases} 6.91 + 12.75\lambda_\theta + 63.64(\lambda_\theta)^2 & \text{for} \quad \lambda_\theta \leq 0 \\ 6.91 + 2.48\lambda_\theta - 12.27(\lambda_\theta)^2 & \text{for} \quad \lambda_\theta < 0 \end{cases} \quad \text{and} \quad \lambda_\theta = \frac{\theta^2}{\nu}\frac{dU_\infty}{dx} \tag{A.4}$$

A.2.3 Van Driest and Blumer Correlation

Van Driest and Blumer Correlation [36] proposed using the vorticity Reynolds number for transition onset criteria, which is defined as

$$Re_v = \frac{(du/dy)y^2}{\nu} \tag{A.5}$$

The onset criteria includes the effect of the freestream turbulence and the pressure gradient parameter using the Pohlhausen fourth-degree velocity profile as

$$9860/Re_\delta = 1 - 0.0485\Lambda + 3.36Re_\delta(u'/U_e)^2 \tag{A.6}$$

where Λ is the Pohlhausen parameter defined as $\Lambda = -(\delta^2/\mu U_e)(dp/dx)$ and δ is the boundary layer thickness.

Bibliography

[1] White, F. *Viscous Fluid Flow*. McGraw-Hill, New York, NY, 2006.

[2] Dagenhart, J. and Saric, W. Crossflow Stability and Transition Experiments in Swept-Wing Flow. Technical Report 1999-209344, NASA, 1999.

[3] Russell, J. Length and Bursting of Separation Bubbles: A Physical Interpretation. Technical Report Conference Publication 2085, Part 1, NASA Langley Research Center, January 1979.

[4] Jain. N., Lee, B., and Baeder, J. D. Assessment of shielding parameters in conventional DDES method under the presence of alternative turbulence length scales. In *23rd AIAA Computational Fluid Dynamics Conference, AIAA AVIATION Forum*, 2017.

[5] Jain, R. CFD Performance and Turbulence Transition Predictions on an Installed Model-scale Rotor in Hover. In *55th AIAA Aerospace Sciences Meeting*, January, 2017.

[6] Hariharan, N., Potsdam, M., and Wissink, A. Helicopter Rotor Aerodynamic Modeling in Hover Based on First-Principles: State-ofthe- Art and Remaining Challenges. In *50th AIAA Aerospace Sciences Meeting*, January, 2012.

[7] Wolf, C., Schwarz, C., Kaufmann, K., Gardner, A., Michaelis, D., Bosbacj, J., Schanz, D., and Schrder, A. Experimental Study of Secondary Vortex Structures in a Rotor Wake. In *45th European Rotorcraft Forum*, September 2019.

[8] Lomax, H., Pullilam, T. H., and Zingg, D. W. *Fundamentals of Computational Fluid Dynamics*. Springers, 2001.

[9] V. Lakshminarayan. *Computational Investigation of Micro-Scale Coaxial Rotor Aerodynamics in Hover*. PhD thesis, University of Maryland, 2009.

[10] Overmeyer, A. D. and Martin, P. B. Measured Boundary Layer Transition and Rotor Hover Performance at Model Scale. In *55th AIAA Aerospace Sciences Meeting*, January, 2017.

[11] Hariharan, N., Egolf, A., Narducci, R., and Sankar. L. Helicopter Rotor Aerodynamic Modeling in Hover: AIAA Standardized Hover Evaluations. In *53rd AIAA Aerospace Sciences Meeting*, January, 2015.

[12] Slotnick, J., Khodadoust, A., Alonso, J., Darmofal, D., Gropp, W., Lurie, E., Mavriplis, D. CFD Vision 2030 Study: A Path to Revolutionary Computational Aerosciences. Technical Report CR-2014-218178, NASA, March 2014.

[13] Spalart, P. R., and Allmaras, S. R. A One-Equation Turbulence Model for Aerodyanmics Flow. *La Recherche Aerospatiale 1*, 1(3):5–21, 1994.

[14] F. R. Menter. Two-equation eddy-viscosity turbulence models for engineering applications. *AIAA Journal*, 12(8):15981605, 1994.

[15] R. B. Langtry and F. R. Menter. Correlation-based transition modeling for unstructured parallelized computational fluid dynamics codes. *AIAA Journal*, 47(12):2894–2906, 2009.

[16] Pope, S. B. *Turbulent Flows*. Cambridge University Press, New York, NY, 2000.

[17] Lee, B., Govindarajan, B., and Baeder, J. Methods for Efficient Resolution of Vortical Structures of an S-76 Rotor in Hover. In *55th AIAA Aerospace Sciences Meeting*, Jan. 2017.

[18] Lee, B., Jung, Y. S., Jude, D. and Baeder, J. Turbulent Transition Prediction of PSP Hovering Rotor using $\gamma - \overline{Re_{\theta t}}$-SA with Crossflow Transition Model. In *AIAA Scitech 2019 Forum*, January, 2019.

[19] Hwang, J. Y., and Kwon, O. J. Numerical Study of PSP Rotor Blades using a $\gamma - Re_{\theta t} - CF^{+}$ Turbulent Transition Model. In *AIAA Scitech 2019 Forum*, January, 2019.

[20] Park, S., Kwon, O. J. Numerical Study of Isolated and Full Configuration PSP Rotor Using a Mixed Mesh Flow Solver. In *AIAA Scitech 2020 Forum*, January, 2020.

[21] Chaderjian, N., and Buning, P. High Resolution Navier-Stokes Simulation of Rotor Wakes. In *AHS 67th Annual Forum*, May 3-5, 2011.

[22] Hariharan, N., Wissink, A., Steffen, M., and Potsdam, M. Tip Vortex Field Resolution Using a Adaptive Dual-Mesh Computational Paradigm. In *49th Aerospace Sciences Meeting*, January 4–7, 2011.

[23] Jain, R. A Comparison of CFD Hover Predictions for the Sikorsky S-76 Rotor. In *54th AIAA Aerospace Sciences Meeting*, January 4–8, 2017.

[24] Abras J., Narducci R., and Hariharan N. Wake Breakdown of High-fidelity Simulations of a Rotor in Hover. In *AIAA Scitech 2019 Forum*, January 7–11, 2019.

[25] Abras J., Narducci R., and Hariharan N. Impact of High-fidelity Simulation Variations on Wake Breakdown of a Rotor in Hover. In *AIAA Scitech 2020 Forum*, January 6–10, 2020.

[26] Hariharan N., Abras J., and Narducci R. An Overview of Wake Breakdown in High-Fidelity Simulations of Rotor-in-Hover. In *AIAA Scitech 2020 Forum*, January 6–10, 2020.

[27] Reynolds, O. An experimental investigation of the circumstances which determine whether the motion of water shall direct or sinous, and of the law of resistance in parallel channels. *Philosophical Transaction of the Royal Society*, 174:935–982, 1883.

[28] Mayle, R.E. The Role of Laminar-Turbulent Transition in Gas Turbine Engines. *Journal of Turbomachinery*, 113:509537, 1991.

[29] Spalart, P. R., and Allmaras, S. R. A One-Equation Turbulence Model for Aerodyanmics Flows. In *AIAA-Paper-1992-0439, 30th AIAA Sciences Meeting and Exhibit*, January 6–9, 1992.

[30] Menter, F. R. Improved Two-Equation k-omega Turbulence Models for Aerodynamic Flows. Technical Report 103975, NASA, 1992.

[31] Kaufmann, K., Stroer, P., Richez, F., Lienard, C., Gardarein, P., Krimmelbein, N., Gardner, A. D. Validation of boundary-layer-transition computations for a rotor with axial inflow. In *Vertical Flight Society 75th Annual Forum*, May 2019.

[32] S. Medida. *Correlation-based Transition Modeling for External Aerodynamic Flows*. PhD thesis, University of Maryland, 2014.

[33] Menter, F. R., and Smirnov, P. E. Development of a RANS-based Model for Predicting Crossflow Transition. In *Presented at the 2014 STAB Symposium, Munich 2014*, 2014.

[34] J. G. Coder and M. D. Maughmer. Computational fluid dynamics compatible transition modeling using an amplification factor transport equation. *AIAA Journal*, 52(11):2506–2512, 2014.

[35] Carnes, J. and Coder, J. Effect of Crossflow on the S-76 and PSP Rotors in Hover. In *AIAA Scitech 2020 Forum*, January, 2020.

[36] Van Driest, E. R. and Blumer, C. B. Boundary Layer Transition: Freestream Turbulence and Pressure Gradient Effects. *AIAA Journal*, 1:1303–1306, 1963.

[37] Langtry, R. B., Sengupt, K., Yeh, D. T., and Dorga, D. J. Extending the $\gamma - Re_{\theta t}$ Local Correlation based Transition Model for Crossflow Effects. In *AIAA AVIATION Forum*, June 22–26, 2015.

[38] Muller, C. and Herbst, F. Modelling of Crossflow-induced Transition based on Local Variables. In *6th European Conference on Computational Fluid Dynamics (ECFD)*, 2014.

[39] Grabe, C., Nie, S. and Krumbein, A. Transport Modeling for the Prediction of Crossflow Transition. *AIAA Journal*, 56:3167–3178, 2018.

[40] Dassler P., Kozulovic D., and Fiala A. . Modeling of Roughness-Induced Transition Using Local Variables", in European. In *Congress on Computational Methods in Applied Sciences and Engineering (ECCOMAS 2012)*, September 10–14, 2012.

[41] Langel, C., Chow, R., Dam, C. P., and Maniaci, D. C. A Transport Equation Approach to Modeling the Influence of Surface Roughness on Boundary Layer Transition. Technical Report SAND2017-10670, SANDIA, October, 2017.

[42] Nichols, R. Addition of a Local Correlation-Based Boundary Layer Transition model to the CREATETM-AV Kestrel Unstructured Flow Solver. In *AIAA Scitech 2019 Forum*, January 7–11, 2019.

[43] Drela, M. and Giles, M. B. Viscous-Inviscid Analysis of Transonic and Low-Reynolds Number Airfoils. *AIAA Journal*, 25:1347–1355, 1987.

[44] Mack, L. M. Transition and Laminar Instability. Technical Report CR-153203, NASA, May 1977.

[45] Sankaran, V., Sitaraman, J., Wissink, A., Datta, A., Jayaraman, B., Potsdam, M., Mavriplis, D., Yang, Z., O'Brien, D., Saberi, H., Cheng, R., Hariharan, N., and Strawn, R. Application of the Helios Computational Platform to Rotorcraft Flowfields. In *AIAA-Paper-2010-1230, 48th AIAA Aerospace Sciences Meeting*, January, 2010.

[46] Garcia, A. J., Colonia, S., and Barakos, G. N. Accurate Predictions of Hovering Rotor Flows Using CFD. In *55th AIAA Aerospace Sciences Meeting*, January, 2017.

[47] Menter, F. R., Smirnov, P. E., Liu, T., and Avancha, R. A one-equation local correlation-based transition model. *Flow Turbulence and Combustion*, 95(4):583619, 2015.

[48] Sheng, C. Role of Transition Modeling in Rotor Hover Predictions. *Journal of Aircraft*, 55(1):23–37, 2018.

[49] Vieira, B. A., Kinzel, M. P., and Maughmer, M. D. CFD Hover Predictions Including Boundary-Layer Transition. In *55th AIAA Aerospace Sciences Meeting*, January, 2017.

[50] Parwani, A., and Coder, J. G. CFD Predictions of Rotor-Fuselage Interactions Using Laminar-Turbulent Transition Modeling. In *AHS 74th Annual Forum*, May, 2018.

[51] Zhao, Q, Wang, J, and Sheng, C. Numerical Simulations and Comparisons of PSP and S-76 Rotors in Hover. In *56th AIAA Aerospace Sciences Meeting*, January, 2018.

[52] Zhao, Q., Baugher, S., and Sheng, C. Numerical Simulations of an Isolated PSP Rotor and Full Configuration in Hover. In *AIAA Scitech 2019 Forum*, January, 2019.

[53] Fitzgibbon, T. A., Barakos, G. N., Woodgate, M. A., and Garcia, A. J.,. Numerical Simulations of Various Rotor Designs in Hover and Forward Flight. In *AIAA Scitech 2019 Forum*, January, 2019.

[54] Spalart, P. R. and Rumsey, C. L. Effective Inflow Conditions for Turbulence Models in Aerodynamic Calculations. *AIAA Journal*, 45(10):2544–2553, 2007.

[55] Kato, M. and Launder, B. E. The Modelling of Turbulent Flow Around Stationary and Vibrating Square Cylinders. In *9th Symposium on Turbulent Shear Flows*, August 1993.

[56] Jain, R. Sensitivity study of high-fidelity hover predictions on the Sikorsky S-76 rotor. *Journal of Aircraft*, 55(1):78–88, 2018.

[57] Abras J., Hariharan N. Performance Impact of Tip Shape Variations on the S-76 Rotor Using kCFD. In *54th AIAA Aerospace Sciences Meeting*, January 4–8, 2016.

[58] Srinivasan, G. R., and Baeder, J. D. TURNS: A Free-Wake Euler/Navier–Stokes Numerical Method for Helicopter Rotors. *AIAA Journal*, 31(5):959–962, 1933.

[59] J. Dacles-Mariani, D. Kwak, and G. Zilliac. On numerical errors and turbulence modeling in tip vortex flow prediction. *International Journal for Numerical Methods in Fluids*, 30(1):65–82, 1999.

[60] Van Leer. Towards the ultimate conservative difference scheme v. a second-order sequel to godunovs method. *Journal of Computational Physics*, 32(1):101–136, 1979.

[61] Jiang, G. S., and Shu, C. W. Efficient Implementation of Weighted ENO Schemes. *Journal of Computational Physics*, 126(1):202–228, June 1996.

[62] P. Roe. Approximate riemann solvers, parameter vectors and difference schemes. *Journal of Computational Physics*, 43(2):357–372, 1981.

[63] A. Harten and J. M. Hyman. Self adjusting grid methods for one-dimensional hyperbolic conservation laws. *Journal of Computational Physics*, 50(2):235–269, 1983.

[64] B. Koren. Multigrid and defect correction for the steady navier-stokes equations. *Journal of Computational Physics*, 87(1):25–46, 1990.

[65] Aslam T. D. Henrick, A. K. and J. M. Powers. Mapped weighted essentially non-oscillatory schemes: Achieving optimal order near critical points. *Journal of Computational Physics*, 207(2):542–567, 2005.

[66] R. Borges, M. Carmona, B. Costa, and D. Don. An improved weighted essentially non-oscillatory scheme for hyperbolic conservation laws. *Journal of Computational Physics*, 227(6):3191–3211, 2008.

[67] Yoon, S., and Jameson, A. Lower-Upper Symmetric-Gauss-Seidel Method for the Euler and Navier–Stokes Equations. *AIAA Journal*, 26(9):1,025–1,026, 1988.

[68] Pulliam, T. H. and Chaussee, D. A diagonal form of an implicit approximate factorization algorithm. *Journal of Computational Physics*, 39(2):347–363, 1981.

[69] Y. Lee. *On Overset Grids Connectivity and Vortex Tracking in Rotorcraft CFD*. PhD thesis, University of Maryland, 2008.

[70] Brazell, M., Sitaraman, J. and Mavriplis, D. An overset mesh approach for 3d mixed element high-order discretizations. *Journal of Computational Physics*, 322(1), 2016.

[71] Jung, Y. S. and Baeder, J. $\gamma - \overline{Re_{\theta t}}$-SA with Crossflow Transition Model using Hamiltonian-Strand Approach. *Journal of Aircraft*, 2019.

[72] Colonia, S., Leble, V., Steijl, R., and Barakos, G. Assessment and calibration of the γ-Equation Transition Model at Low Mach. *Journal of Aircraft*, 55(4):1126–1139, 2017.

[73] Schubauer, G.B., Klebanoff, P.S. Contribution on the Mechanics of Boundary Layer Transition. Technical Report TN 3489, NACA, 1955.

[74] Coupland, J. Special interest group on laminar-to-turbulent transition and retransition: T3a and t3b test cases. Technical Report A309514, ERFCOFTAC, 1990.

[75] Rumsey, C. L., Smith, B. R., and Huang, G. P. Description of a Website Resource for Turbulence Modeling Verification and Validation. In *40th AIAA Fluid Dynamics Conference*, June-July 2010.

[76] Coder, J. Standard Test Cases for Transition Model Verification and Validation in Computational Fluid Dynamics. In *56th AIAA Aerospace Sciences Meeting*, January, 2018.

[77] Chaput, E. Chapter iii: Application-oriented synthesis of work presented in chapter ii, notes on numerical uid mechanic. Technical Report 58, ERFCOFTAC, Vieweg Braunschweig, Wiesbaden, 1997.

[78] Somers, D. M. Design and Experimental Results for the S809 Airfoil. Technical Report 440-6918, NREL/SR, 1997.

[79] Somers, D. M. Design and Experimental Results for a Natural-Laminar-Flow Airfoil for General Aviation Applications. Technical Report 1861, NASA, 1981.

[80] Selig, M. S., and McGranahan, B. D. Wind tunnel aerodynamic tests of six airfoils for use on small wind turbines. Technical Report SR-500-34515, NREL, 2004.

[81] Hall, Z. M. Assessment of Transition Modeling Capabilities in NASAs OVERFLOW CFD Code version 2.2m. In *56th AIAA Aerospace Sciences Meeting*, January, 2018.

[82] Radeztsky, R. H., Reibert, M. S., Saric, W. S., and Takagi, S. Effect of Micron-Sized Roughness on Transition in Swept-Wing Flows. In *AIAA Paper 93-0076*, Jan. 1993.

[83] Venkatachari, B. S., Paredes, P., Derlaga, J. M., Buning, P., Choudhari, M., Li, F., and Chang, C. Assessment of Transition Modeling Capability in OVERFLOW with Emphasis on Swept-Wing Configurations. In *AIAA Scitech 2020 Forum*, January 2020.

[84] Kreplin, H-P., Vollmers, H., and Meier, H. U. Wall shear stress measurements on an inclined prolate spheroid in the DFVLR 3 m x 3 m low speed wind tunnel. Technical Report IB 22-84 A 33, DFVLR-AVA, 1985.

[85] Jain, R. Effect of Facility Walls and Blade Aeroelasticity on PSP Rotor Hover Performance Predictions. In *56th AIAA Aerospace Sciences Meeting*, January, 2018.

[86] Jung, Y. S., Vijayakumar, G., Ananthan, S., Baeder, J. Correlation-based Transition Models for High-Reynolds-Number Wind Turbine Airfoils. *Wind Energ. Sci. Discuss. [preprint]*, 2021.

[87] Duraisamy, K. Development of a New Class of High order Implicit Non-Oscillatory Schemes for Conservation Laws. Master thesis, Department of Applied Mathematics, University of Maryland, College Park, MD, 2004.

[88] Smith, A. M. O. and Gamberoni, N. Transition, Pressure Gradient, and Stability Theory. Technical Report ES-26388, Douglas Aircraft, 1956.

[89] Van Ingen, J. L. Suggested Semi-Empirical Method for the Calculation of the Boundary Layer Transition Region. Technical Report VTH-74, Dept. of Aerospace Engineering, Delft Univ. of Technology, 1956.

[90] Van Ingen J. L. The e^n method for transition prediction. Historical review of work at tu delft. In *38th AIAA Fluid Dynamics Conference and Exhibit*, January, 2008.

[91] Orr, W. M. The Stability or Instability of the Steady Motions of a Perfect Liquid and of a Viscous Liquid, Part I: A Perfect Liquid. *Proceedings of the Royal Irish Academy, Section A: Mathematical and Physical Sciences*, 27:9–68, 1907.

[92] Sommerfeld, A. Ein Beitrag zur hydrodynamische Erklarung der turbulenten Flussigkeitsbewegungen. *Proceedings of the 4th International Congress of Mathematicians*, 3:116124, 1908.

[93] Herbert, Th. And Bertolotti, F. B. Stability analysis of nonparallel boundary layers. *Bulletin of the American Physical Society*, 32:20792806, 1983.

[94] Schrauf, G. LILO 2.1 - Users Guide and Tutorial, Tech. Rep. 6, GSSC. Technical Report 6, GSSC, 2006.

[95] Chang, C-L. The Langley Stability and Transition Analysis Code (LASTRAC): LST, Linear and Nonlinear PSE for 2-D, Axisymmetric, and Infinite Swept Wing Boundary Layers. In *41st AIAA Aerospace Sciences Meeting and Exhibit*, January , 2003.

[96] Krimmelbein, N., and Krumbein, A. Automatic Transition Prediction for Three-Dimensional Configurations with Focus on Industrial Application. *Journal of Aircraft*, 48(6):18781887, 2011.

[97] Lynde, M. N. and Campbell, R. L. Computational Design and Analysis of a Transonic Natural Laminar Flow Wing for a Wind Tunnel Model. In *35th AIAA Applied Aerodynamics Conference*, January, 2017.

[98] Weiss, A., Gardnery, A., Schwermerz, T., Klein, C. On the Effect of Rotational Forces on Rotor Blade Boundary-Layer Transition. In *2018 AIAA Aerospace Sciences Meeting*, January, 2018.

[99] Abu-Ghannam, B. J. and Shaw, R. Natural Transition of Boundary Layers: The Effects of Turbulence, Pressure Gradient, and Flow History. *Journal of Mechanical Engineering Science*, 22:213–228, 1980.